MECHANICAL FATIGUE CHARACTERIZATION OF NITIHF SMA'S FOR A UNIFIED DESCRIPTOR TO ACTUATION FATIGUE

A Thesis

by

HRISHIKESH PADALIA

Submitted to the Graduate and Professional School of
Texas A&M University
in partial fulfillment of the requirements for the degree of

MASTER OF SCIENCE

Chair of Committee,	Dimitris C. Lagoudas
Committee Members,	Jean-Briac le Graverend
	Richard Malak
Head of Department,	Ivett A. Leyva

August 2023

Major Subject: Aerospace Engineering

ABSTRACT

Due to its potential candidacy for use as solid-state actuators, experimental studies to characterize, model, and predict the actuation or thermomechanical fatigue response of NiTiHf high temperature SMA's (HTSMA) have been carried out to assess their functional performance and longevity for optimal actuator design. A drawback of actuation fatigue testing is the high cost and time span the tests require because of slow heating and cooling rates. This is especially applicable to high cycle actuation fatigue, which can take on the order of days to weeks to complete. On the other hand, mechanical or pseudoelastic fatigue is much quicker to carry out due to faster loading rates, with high cycle fatigue tests taking just hours. This work aims to experimentally characterize the mechanical fatigue lifetime and functional response of three Ni-rich NiTiHf HTSMA's ($Ni_{50.3}Ti_{29.7}Hf_{20}$, $Ni_{50.5}Ti_{33.5}Hf_{16}$, and $Ni_{50.6}Ti_{30.4}Hf_{19}$) under uniform testing parameters, and further develop an empirical model to fit established actuation lifetime and work-output data with mechanical fatigue lifetime data. Using this approach, similarity between the two fatigues types along different thermomechanical paths and loading rates, providing a unifying descriptor for tensile thermomechanical fatigue can be demonstrated. This approach showed that a similarity in the slopes of the two fatigue lifetime trends is observed across all the materials tested when using a mechanical work equivalent similar to the actuation work output model based on the Smith-Watson-Topper (SWT) parameter, with actuation data having a consistently higher work output, leading to an offset between both fatigue curves. Additionally, intrinsic properties of the materials such as ductility, is characterized by looking into the mechanical functional trends such as plastic strain accumulation, providing for preliminary material screening methods before extensive actuation fatigue analyses.

ACKNOWLEDGMENTS

I would like to thank my committee chair, Dr. Dimitris Lagoudas for providing the opportunity to work with an amazing group of researchers and for an exciting project. Additionally, I would like to thank my committee members for their guidance throughout my graduate course of study here at Texas A&M University.

I would like to extend my gratitude to Mr. Jim Mabe, Dr. Behrouz Haghgouyan, Dr. Anargyros Karakalas, Dr. Alexander Demblon, Sherilyn Fields, members and affiliates of the Dr. Lagoudas research group (SMARTANS), and members of the NASA ULI materials team along with members of the overall NASA ULI team for their support, technical expertise and mentorship initially and throughout my two plus years as a graduate student.

CONTRIBUTORS AND FUNDING SOURCES

Contributors

This work was supervised by a thesis committee consisting of Professor Dimitris Lagoudas and Jean-Briac le Graverend of the Department of Aerospace Engineering and Professor Richard Malak of the Department of Mechanical Engineering.

Actuation/thermomechanical fatigue lifetime and work output data in chapter 2 (section 2.3.4), and $Ni_{50.3}Ti_{29.7}Hf_{20}$ thermal cycling characterization test data (section 2.2.2) were provided by Dr. Alexander Demblon, a colleague and member of the NASA ULI project here at Texas A&M University. Stress-strain graphs relating to frequency effects on SMA mechanical response in chapter 2 (section 2.3.2 and 2.3.4) was conducted by Dr. Behrouz Haghgouyan, former colleague and member of the project and post-doctoral researcher with the Department of Aerospace Engineering. All other work conducted for the thesis was completed by the student independently.

Funding Sources

Graduate study was supported by an assistantship from the Texas A&M University Department of Aerospace Engineering and Texas A&M Experiment Station (TEES) and research funding from the NASA's University Leadership Initiative (ULI) project.

TABLE OF CONTENTS

LIST OF FIGURES

FIGURE Page

LIST OF TABLES

1. INTRODUCTION

1.1 Introduction to Shape Memory Alloys

Shape Memory Alloys are a class of multifunctional alloy materials that exhibit extraordinary abilities to recover from large deformations under applied thermomechanical loading. This property of large deformations and recovery are characterized by a change in solid-to-solid phases within the material, namely Austenite and Martensite (also known as high-temperature and low-temperature phase respectively). The transformation from one phase to another is a diffusionless process and is characterized by shear lattice distortion, whereby a change in microstructure takes place. A typical phase diagram of an SMA is shown in Figure 1.1.

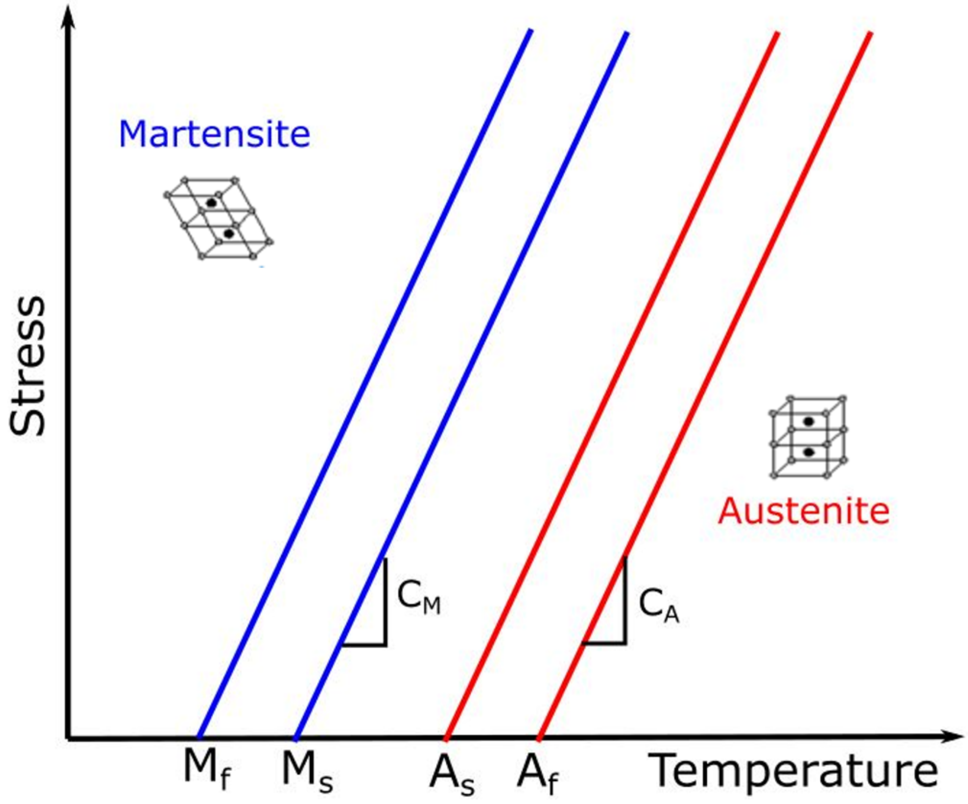

Figure 1.1: General SMA Phase Diagram Schematic

The Martensite and Austenite phases take the left and right side of the diagram, respectively. The four parallel lines showcase temperature thresholds that dictate when the material undergoes transformation from one phase to another. These four lines correspond to the M_f^σ, M_s^σ, A_s^σ, A_f^σ which are the Martensite finish, Martensite Start, Austenite Start and Austenite Finish temperatures which are a function of applied load or stress. The descriptor 'finish' tells us when the transformation is complete to the corresponding phase, and 'start' tells us when the transformation is beginning to the corresponding phase. The changes in phase can be bought about by a change in temperature or load which gives the material its two distinct effects that govern its multifunctionality namely the shape memory effect (SME) and the pseudoelasticity or the superelasticity effect (PE).

- **Shape Memory Effect** - Figure 1.2a shows the thermomechanical path on the phase diagram with the associated changes in microstructure as it relates to the SME (see Figure 1.2c). Also shown is a typical stress-temperature-strain response for the shape memory effect (see Figure 1.2b). This is when a specimen is mechanically loaded in its twinned martensitic phase that induces transformation, and with it, inelastic strain through the detwinning process of Martensite (path 1). Upon unloading, the elastic strains are recovered, but the inelastic strains remain (path 2). Upon an increase in temperature to above A_f, the inelastic strain is recovered when the material transforms to its Austenite phase (path 3). Additionally, upon cooling down to below M_f, the material experiences negligible macroscopic changes when it transforms back to twinned Martensite.

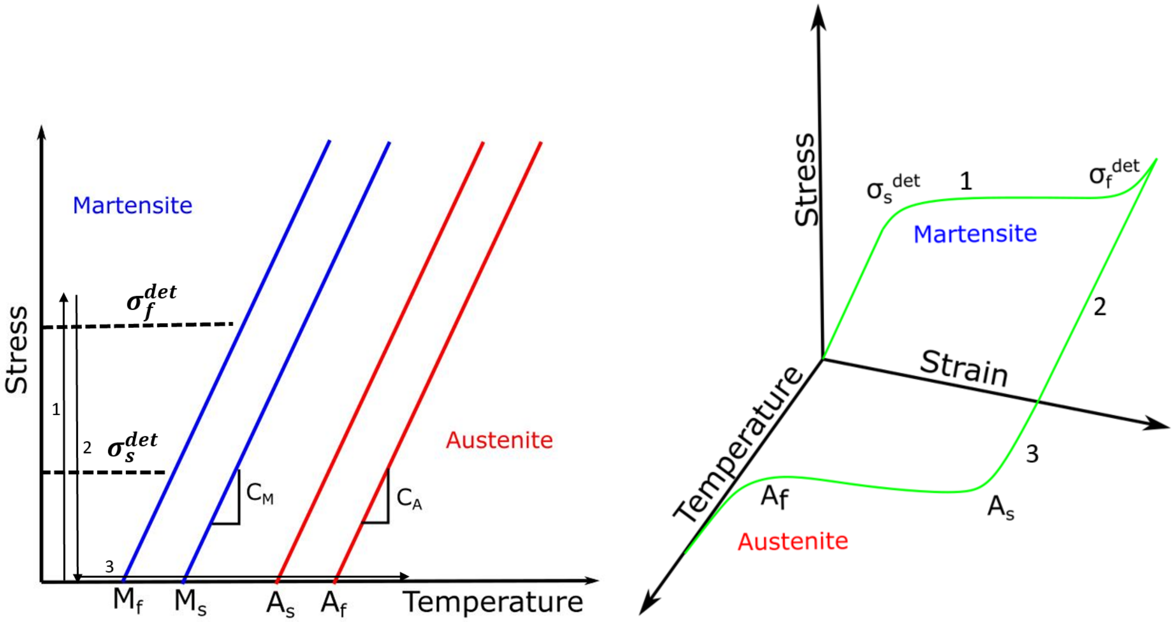

(a) Shape Memory Effect Path

(b) Shape Memory Effect Curve

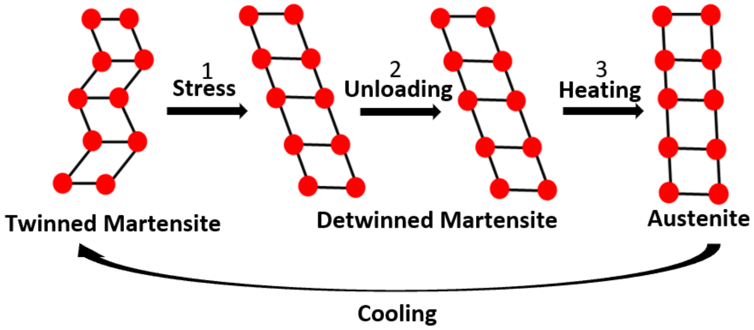

(c) SME Microstructure Evolution

Figure 1.2: The Shape Memory Effect (SME)

- **Pseudoelastic Effect** - Figure 1.3a then shows the loading path corresponding to the pseudoelasticity effect, which is characterized by a specimen held at a constant temperature (isothermal) above A_f and cycled between two loads. Transformation from Austenite to Martensite begins when the critical stress value σ_{Ms} is reached, analogous to the temperature thresholds for the SME. The transformation is complete when σ_{Mf} is reached, with Austenite transforming into detwinned Martensite (path 1). Upon unloading, the material transforms back to its Austenite phase when it crosses the Austenite thresholds (path 2).

The typical stress-strain response for the isothermal pseudoelasticity effect is shown in Figure 1.3b. The related microstructure changes are shown in Figure 1.3c.

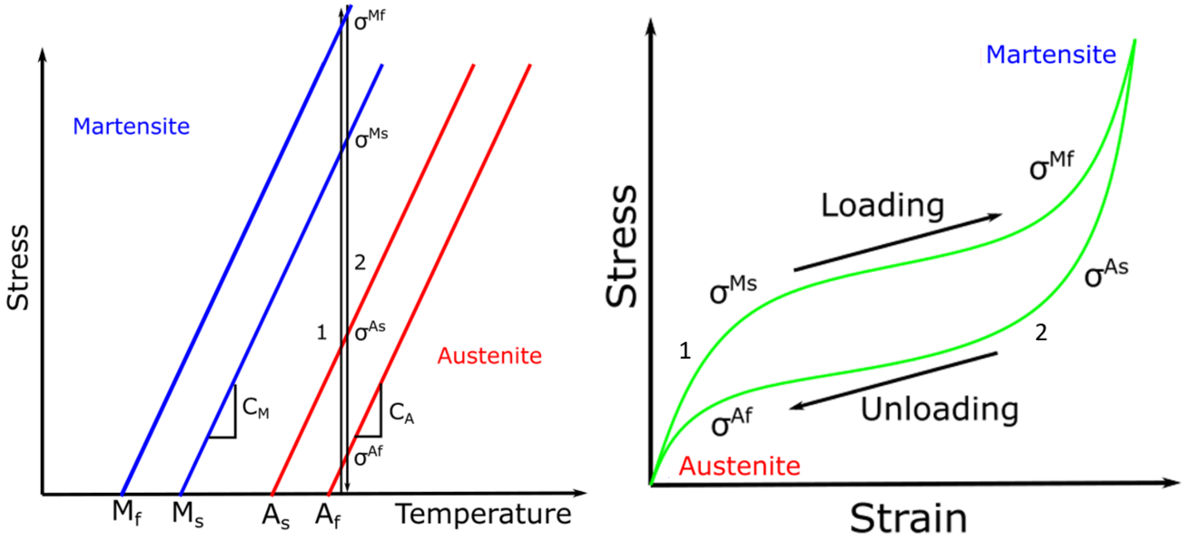

(a) Pseudoelastic Effect Path

(b) Pseudoelastic Curve

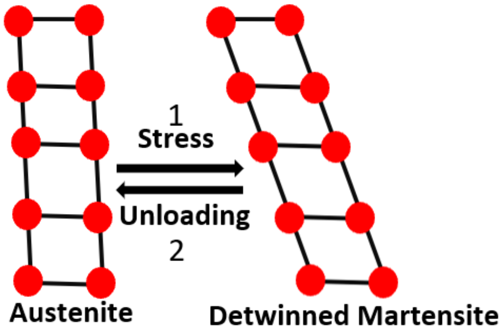

(c) Pseudoelastic Microstructure Evolution

Figure 1.3: The Pseudoelastic Effect

The SME and PE are both based on different thermomechanical paths within the same phase diagram and are fundamental to the multifunctionality of SMA's. As such, in the context of this research and established work in literature and engineering applications, we define a third thermomechanical path that is utilized and is exploited by SMA based actuator systems, known as

actuation cycling, shown below in Figure 1.4. Figure 1.4a shows the thermomechanical path on the phase diagram with the associated changes in microstructure as it relates to actuation cycling (see Figure 1.4c). Also shown is a typical temperature-strain response (see Figure 1.4b). This is when a specimen is under a constant bias load (isobaric) in its twinned martensitic phase that induces transformation, and with it, inelastic strain through the detwinning process of Martensite (path 1). Upon heating to above A_f temperature, the inelastic/transformation strains are recovered when the material transforms to Austenite (path 2). Upon cooling, the inelastic strain is restored when the material transforms back to its detwinned Martensite phase (path 3).

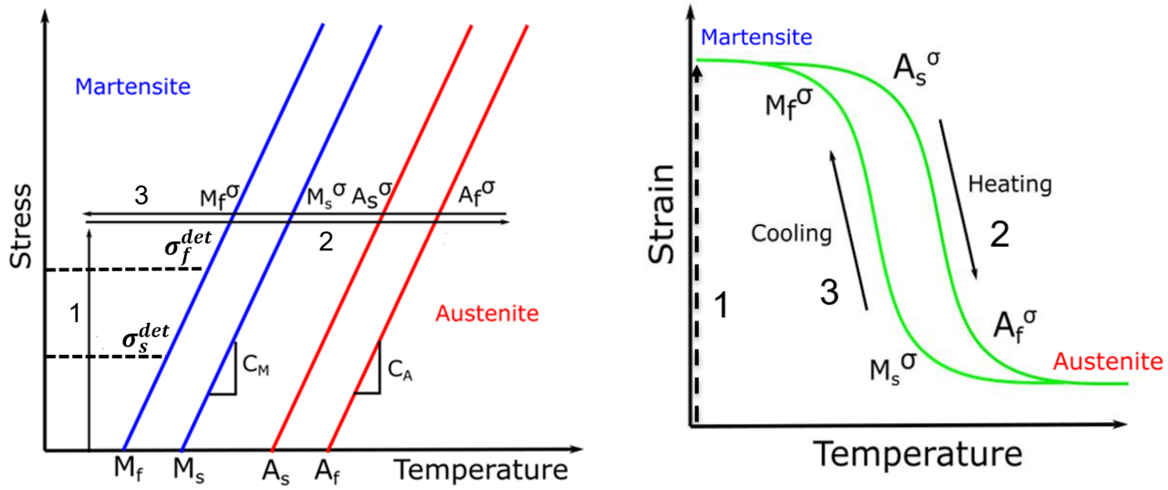

(a) Actuation Cycle Path

(b) Temperature-Strain Curve

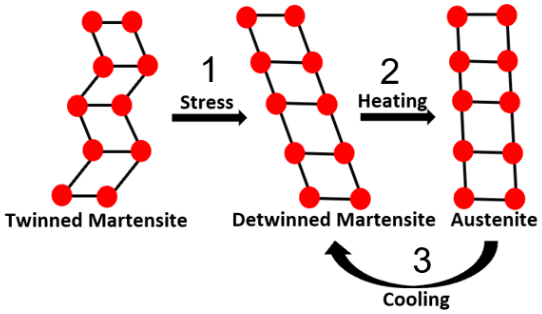

(c) Actuation Microstructure Evolution

Figure 1.4: Actuation Cycle Schematic

Previously, considerable work has been geared towards the actuation response and fatigue of SMA's for actuation based applications. More on this is discussed in the following sections. Since its discovery in the 1960s, Nickel-Titanium SMAs have been widely studied given their high work energy densities and corrosion resistance that has made it a viable candidate for use in many commercial applications including actuation applications for the automotive and aerospace industries [1], but more importantly the medicine field for its excellent superelastic properties and biocompatibility [2, 3]. NiTi materials were extensively used in the biomedical industry taking advantage of the pseudoelastic effect with uses in orthopedics and orthodontics, whereas the aerospace and automotive industries were more attracted by an SMA with high actuation strain density to be used in solid-state actuator systems. As such, the most prevalent and studied binary SMA, NiTi, although exhibiting amazing corrosion resistance, fatigue resistance and strain recovery, was characterized by low transformation temperatures including below freezing Martensite start and finish temperatures [4]. These temperatures were too low for certain application within the automotive and aerospace industries, where actuation systems are subject to higher temperature and overall harsher environments [5]. By adding a ternary element such as Gold, Palladium, Hafnium or Zirconium, researchers created a subclass of NiTi based high temperature shape memory alloys (HTSMA) which showcased much higher range of transformation temperatures (above 100 $^{\circ}C$). However, with the addition of ternary elements and high operating temperatures came the degradation in the material's functional abilities such as low transformation strains, low strain recovery and large Transformation Induced Plasticity (TRIP) leading to residual strains and dimensional (cyclic) instability. The addition of ternary elements amplified the incompatibility between the Austenite and the different Martensite modes, leading to increased dislocation plasticity [6]. Fortunately, further study into manufacturing and aging techniques showed that functional ability i.e. shape memory and cyclic stability can be restored by proper manufacturing techniques such as solid solution and precipitation hardening [7, 8, 9, 10]. Currently, some studies into precipitation hardened Ni-rich NiTiHf based alloys show high actuation strain energies (work outputs), excellent corrosive properties and a stable cyclic hysteresis response. Additionally, Hafnium being a cheaper option compared to the other ternary elements makes it an attractive option for study and potential usage in actuator systems [11]. Heat treatment introduces 'H-phase' nano-precipitates by depleting the matrix of Nickel, which in turns strengthens the matrix by acting as barriers against dislocation motion. More importantly, controlling the amount of precipitates in the matrix helps tailor material properties such as transformation temperatures to our design needs [12, 13, 14].

1.2 Applications

SMAs have a wide range of applications in the automotive, aerospace, civil and biomedical industries. Some interesting applications within the aerospace industry include the following.

In 2003, the Defense Advanced Research Projects Agency (DARPA) initiated a program to conduct research and build active and adaptive wing structures that have the ability to change their characteristics substantially [15]. Following, they started the Smart Wing Program (using SMAs to alter wing camber) followed by the SAMPSON program, which dealt with advanced engine inlet morphing [16]. The inlet of the F-15 jet was used to perform adaptive morphing (see Figure 1.5a). In this, a full scale inlet tested by NASA Langley was used wherein bundles of SMA wires were used to rotate the engine cowling (front end of the engine inlet that helps direct/condition the flow) up to nine degrees. This mechanism varies the inlet air flow cross-section to ensure smooth and high mass flow rates at high angles of attack. On the aft of the nozzle, SMA cables were laid circumferentially that morphed the nozzle exit area under different operating conditions.

To develop wheels resistant to the treacherous terrain of Mars, NASA has 'reinvented the wheel' by utilizing NiTi wire mesh tires for the next generation of vehicles on Mars. The pseudoelasticity effect of NiTi allows for the tires to conform to the terrain while retaining its original configuration (see Figure 1.5b).

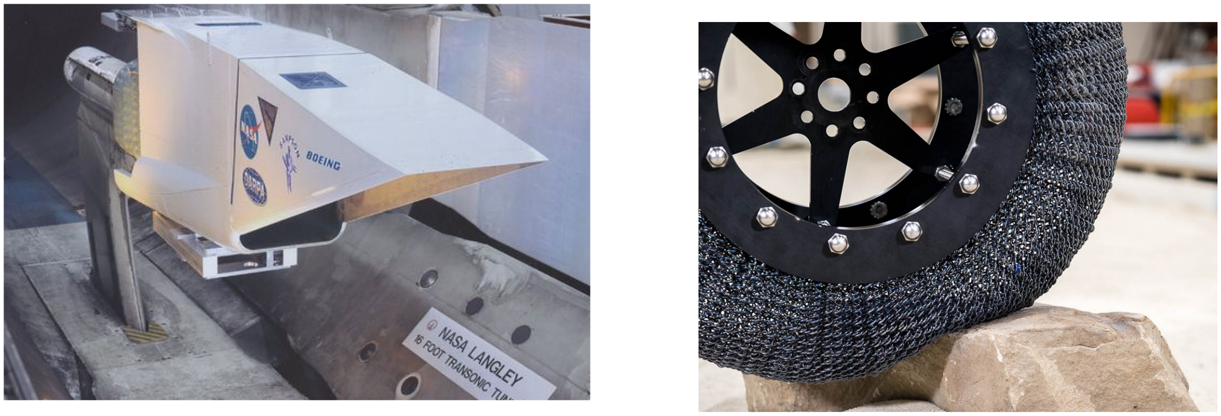

(a) SMA Embedded F-15 Inlet

(b) NASA NiTi Based Wheel

Figure 1.5: Aerospace Applications of SMAs (Credit: NASA)

SMAs were used on engine chevrons of a Boeing 777 that cover the rear edges of high bypass turbofans [17, 18] (see Figure 1.6). Mixing cold air from the fan and hot air from the exhaust correlates to how loud these engines can be. Using SMA strips embedded on the inside of chevrons, the configurations of the chevron can be altered at take-off, landing, and cruise based on ambient temperatures. These configurations reduce noise at low altitudes and drag at cruise altitudes, increasing engine efficiency.

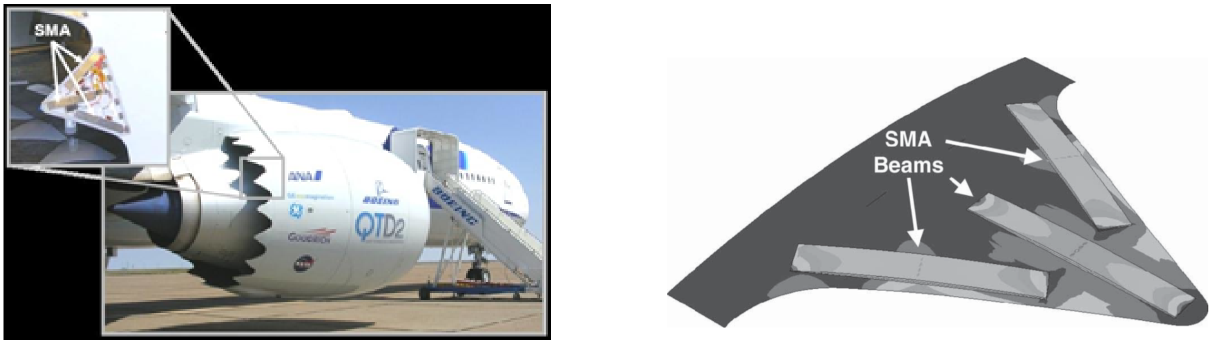

(a) SMA Chevrons on Engine Outlet[17]

(b) SMA Beam Layout on Chevron [18]

Figure 1.6: Using SMA Beams on Engine Chevrons for Noise Reduction

Barbarino et al. [19] implemented Ni-TI-Cu SMA based actuation devices to introduce local bumps to the upper surface of airfoils as means of transonic drag reduction caused due to shock waves. It is shown that SMAs can be used to alter an aerodynamic surface' profile to maximize aerodynamic efficiency.

NASA's Earth Observatory-1 satellite employs the use of SMAs shape memory effect for the deployment mechanism of the Lightweight Flexible Solar Array (LFSA) (see Figure 1.7) [20].

Implementing SMAs along the spanwise directions of a helicopter blade can be used to alter the camber and twist for increased efficiency at the given flight conditions [21].

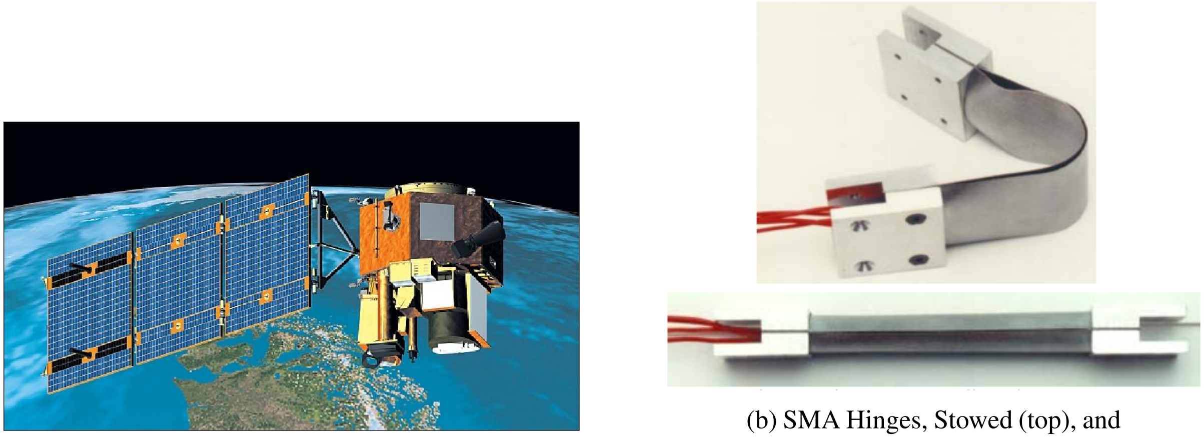

(a) NASA EO-1 Satellite

(b) SMA Hinges, Stowed (top), and Deployed (bottom)[20]

Figure 1.7: SMAs used in NASA's EO-1 LFSA for Solar Array Deployment (Credit: NASA/GSFC)

Apart from Aerospace, SMAs have wide applications in the civil, robotics and medical industries. SMAs can be used to create medical implants that can be easily inserted and then expanded once they are in place. For example, stents, which are used to open up narrowed or blocked blood vessels, can be made from SMAs and then expanded inside the body using heat or a magnetic field (for magnetic SMAs) [2]. SMAs are used to create dental braces that are more comfortable and effective than traditional braces, using the pseudoelasticity effect. NiTi rods are used to correct scoliosis and used to join fracture surfaces in orthopedics using its shape memory effect [2].

The pseudoelastic properties and subsequent energy dissipation and hysteresis of SMAs are also utilized, with its most effective application being that of vibration and impact attenuation. SMA coils/rods are used anywhere from vehicles and civil structures where high vibration environments exist [22]. Due to a hysteresis and hence mechanical energy dissipation, these materials can help with dampening when morphed.

1.2.1 NASA ULI X-59 Low-Boom Flight Demonstrator

The X-59 Quiet SuperSonic Technology (X-59 QueSST) low boom demonstrator aircraft is part of the next generation of supersonic transport in development by Lockheed Martin and NASA. The aircraft is expected to cruise at Mach 1.4 at an altitude of 54000 feet for a lower perceived loudness (decibel) on the ground [23]. The University Leadership Initiative (ULI) project concerns itself with the idea for a lower perceived sonic boom intensity on the ground using a series of morphing panels on the outer mold line (at the belly of the fuselage) of the aircraft. These morphing panels would attain a specific configuration based on the current flight conditions and atmospheric profile via SMA based solid-state torque tube actuators. As such, research into tailoring the ideal SMA for its work output and fatigue properties to be used in such actuators forms one of the basis of the ULI project.

1.3 Fatigue of Shape Memory Alloys

Actuator systems that use SMAs rely on its repeated cycling to attain the required work/strain output. Fatigue becomes an important property and design parameter that needs to be taken into account when designing such systems.

Fatigue in SMAs has characteristics different from conventional metals. Two types of fatigue mechanisms exist in SMAs in literature: structural, and functional fatigue [24].

- **Structural fatigue** involves the failure by repeated cyclic mechanical loading of the material. This usually pertains to loading between an upper and lower cycle stress level at a constant temperature for SMA's (referred to as mechanical fatigue here [25], see Figure 1.3 for schematic for $T > A_f$). Structural fatigue can further be generalized into **low cycle** and

high cycle fatigue. Low cycle fatigue refers to samples that undergo yielding to Martensite and hence some degree of reversible phase transformation and accumulation of plastic strains as cycling goes on. High cycle on the other hand refers to samples that are cycled below the σ_{Ms} values of the material, in the predominately elastic regime, resulting in no phase transformation and plastic strain accumulation. This is analogous to fatigue exhibited by conventional metals, where high cycle fatigue refers to cycling within the material's elastic limit, and low cycle fatigue where the material is cycled beyond the elastic limit, causing yielding and accumulation of plastic strains per cycle. The difference between SMA's and conventional metals is that SMA's undergo yielding due to phase transformation which is also reversible, unlike conventional metals that undergo yielding due to permanent plastic deformation. The micromechanisms for structural fatigue involves internal damage accumulation that leads to catastrophic failure. This involves dislocation generation and movement, micro-crack formation and propagation, macro-crack formation and propagation, and finally to failure. This type of fatigue involves recovery of recoverable inelastic deformation from the formation of stress induced martensite (SIM) during transformation

- **Functional fatigue** involves the degradation of shape memory properties for thermally induced phase transformation and pseudoelastic properties for stress induced phase transformations throughout the materials' lifetime. This occurs due to internal damage resulting from dislocation motion and microstructural irreversibility via accumulation of plastic strains [24]. This includes properties such as transformation stresses/temperatures, transformation strain, plastic strains, strain energy densities, and energy dissipation, leading to an evolving stress-strain and/or temperature-strain response. Functional fatigue therefore can be subdivided into functional pseudoelastic fatigue and functional actuation fatigue. Given that actuation cycling has been established, a third type of fatigue, actuation fatigue, is necessary to address the hypothesis laid out in this thesis

- **Actuation fatigue** involves thermally cycling the SMA at a constant bias load [26], which is the mechanism actuator systems rely on. This type of fatigue is unique to SMA's. The loading path, temperature-strain response and associated microstructure for actuation cycling is shown previously in Figure 1.4. Actuation lifetime response also involves the mechanisms of internal damage accumulation, as such thermally-induced structural fatigue makes up an important failure mode, similar to mechanical fatigue. This type of fatigue involves the recovery of recoverable inelastic deformation from the formation of temperature induced martensite (TIM) during transformation

Two approaches to studying fatigue in SMAs are commonplace in literature;

- The **microscopic** point of view. Investigations using microscopy to study mechanisms of crack initiation and propagation at the grain level using microscopy techniques including scanning electron microscopy (SEM), transmission electron microscopy (TEM), and X-ray tomography. These studies provide an insight into the internal mechanisms of damage accumulation from cyclic phase transformation, along with material microstructure characterization.

- The **macroscopic** point of view. This approach, which is the primary approach in this thesis, studies the effect of macroscopic properties of the material and environment including loading conditions on fatigue. This includes using variables such as stress, strain, and energy for the formation of models to create Wohler curves for fatigue lifetime modelling and prediction. Effect of properties such as heat treatments, geometry, composition among others on fatigue properties are also studied. Furthermore, studying the macroscopic evolution of functional properties such as transformation strain, transformation stresses/temperatures and plastic strains/TRIP gives an insight into the functional fatigue of the material

To reiterate, actuation fatigue is when a specimen is under a constant bias load and cycled between an upper cycle and lower cycle temperature (UCT and LCT, respectively). Pseudoelastic fatigue is when a specimen is held at a constant temperature and cycled between an upper cycle and lower cycle stress (UCS and LCS, respectively). Fatigue lifetime of a SMA depends on many factors, and studies on the fatigue properties of NiTi SMAs have been extensive, especially pseudoelastic fatigue of NiTi SMAs. These factors include composition [27], level of impurities and inhomogenieties in the matrix [28, 29], which can facilitate the formation of cracks by acting as regions of increased stress concentrations, annealing temperatures and heat treatments [30] that define a material's plastic properties and its resistance to plastic deformation, and surface texture and roughness [24, 31]. Additionally, loading conditions such as stress levels [24, 27, 32], temperature [33], and loading frequency [34] greatly affect the fatigue lifetime. Figure 1.8 summarizes the factors affecting SMA fatigue life. Research into thermomechanical and mechanical fatigue of HTSMAs is an ongoing and evolving field that is gaining momentum due to its recent relevance.

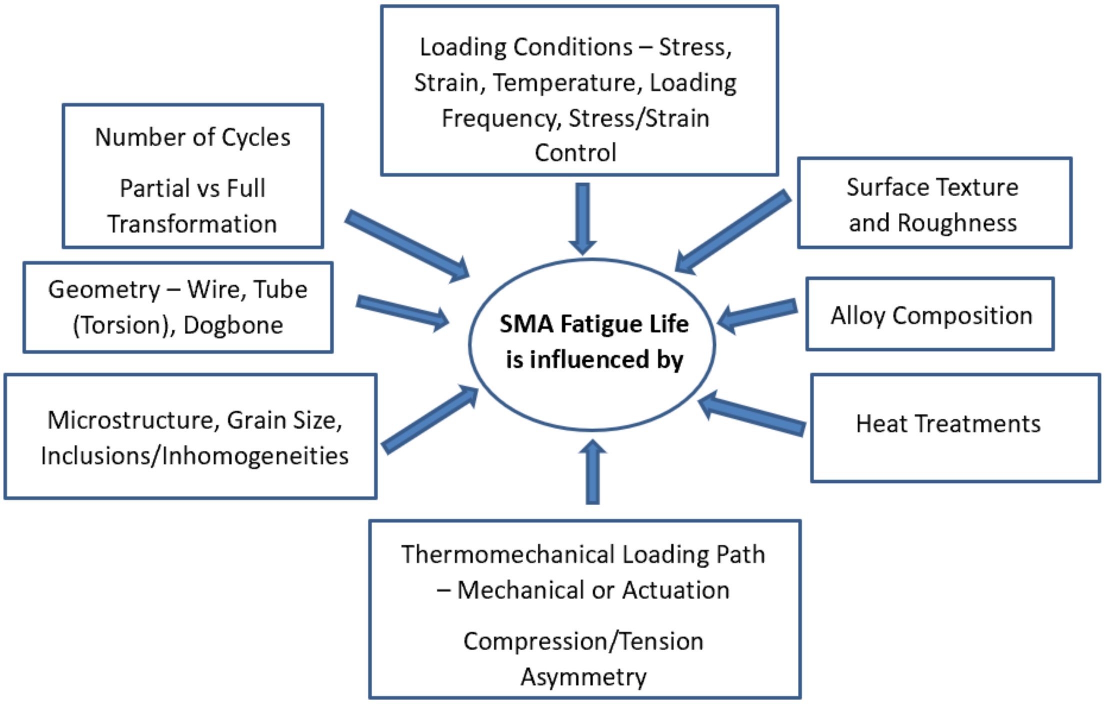

Figure 1.8: Factors Influencing Fatigue Lifetimes in SMAs

1.3.1 Micromechanisms of Fatigue in SMAs

During pseudoelastic cyclic deformation of SMAs, the SMA undergoes its 'training' period where there is a large accumulation of plastic strain before stabilization of the stress-strain response occurs, reaching what is called the shakedown state [35] (see Figure 1.9). This is assuming enough loads where the material yields to Martensite and reversible phase transformation during each cycle occurs. This continual accumulation of plastic strains due to cyclic loading of pseudoelastic SMA's is called ratcheting. This differs to the ratcheting that is seen with conventional metals, wherein there is accumulation of plastic strains during cyclic loading when the load is beyond the elastic limit of the metal. If phase transformation is minimal or non-existent, plastic strains accumulation is negligible and no ratcheting occurs. Instead, the material reaches elastic shakedown. An example of strain evolution during phase transforming mechanical cycling for SMA's is shown in Figure 1.9, showing a materials strain response saturating, i.e. reaching the shakedown state. In superelastic SMA's, due to the fact that this accumulation of plastic strains occurs via reversible transformation, it is also referred to as 'transformation ratcheting.' [36] On the other hand, during stress-controlled shape memory cyclic deformation of SMA's (in Martensite phase), no transformation occurs between Austenite and Martensite. The ratcheting deformations induced during such cycling occurs due to the viscoplastic reorientation or detwinning process of Martensite. This is similar in sense to conventional metals.

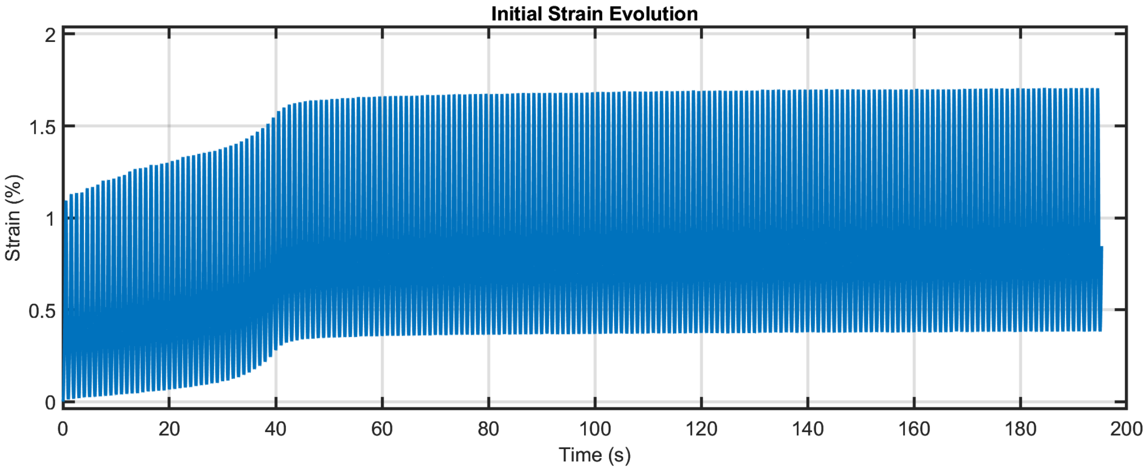

Figure 1.9: Cyclic Strain Response and Stabilization

During both actuation and mechanical cycling, the phase transformation leads to the accumulation of plastic strains. As such, similar to pseudoelastic cyclic, actuation cycling also undergoes training. Training is an important phase of a SMA, especially when tailoring material properties for SMA actuator systems. Training is done in order to attain stable reversible transformation after a period of plastic strain accumulation. For actuators, which utilize thermal cycling, training is done via thermal cycles under a bias load. After a certain number of cycles, ratcheting becomes minimal, plastic strains and temperature-strain response stabilize, and the actuator or specimen achieves a stable two-way shape memory configuration. Figure 1.10 shows an example of actuation (from Karakoc et al. [37]) and mechanical cycling to failure. For an actuation test lasting 21000 cycles on $Ni_{50.3}Ti_{29.7}Hf_{20}$, a large portion of the plastic strain accumulated (near half) occurs within the first 1000 cycles. Similarly, for the pseudoelastic cycling, which can be seen within the first 100 cycles. Both materials experience large initial plastic strain accumulation during this training phase, before a stable response is realized.

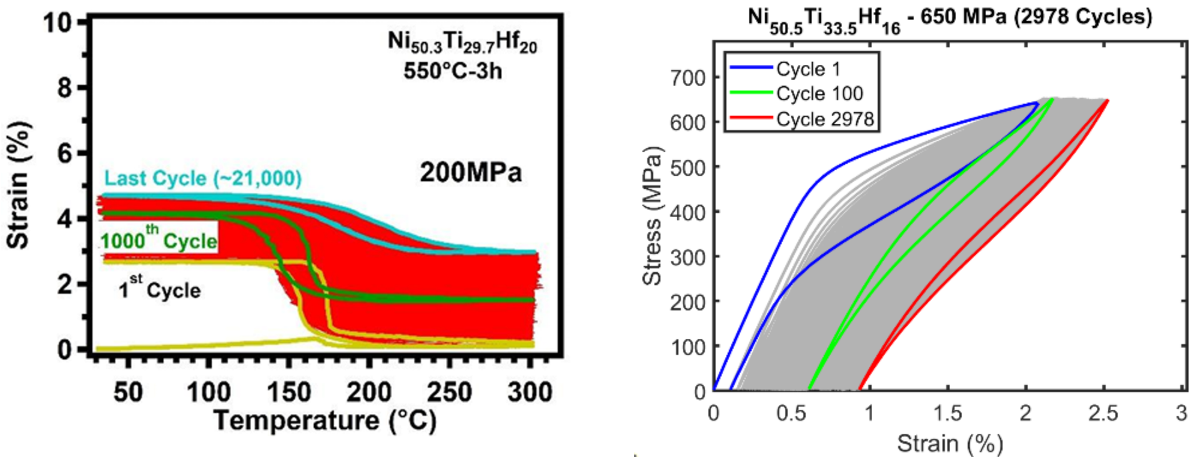

(a) Full Thermal Cycling (Reprinted with permission from [37])

(b) Mechanical/Pseudoelastic Cycling

Figure 1.10: Fatigue Cycles to Failure, Showcasing Initial Ratcheting and Training with Total Plastic Strain Accumulation

According to Phillips et al. [38], this large accumulation of initial plastic strains is due to the initial dislocation defects that existed prior to the fatigue cycling due to manufacturing constraints that move along the habit plane in Austenite, which is the interface between austenite-martensite (A-M) and martensite-martensite (M-M) regions. During loading, favorably oriented Martensite Variants will transform first, leading to the creation of A-M interfaces, with M-M interfaces existing between different Martensite variants. The strain and modulus incompatibility between the Austenite and Martensite phases (A-M) promote the existence of localized residual stresses and consequently the formation of dislocations at the interface [39]. As cycling continues, fewer dislocations will move while most will pile up and get pinned at grain boundaries, surfaces, or inclusions such as nano-precipitates which will facilitate the formation of microcracks. At the same time, these dislocations multiply and remain along the interface upon unloading and prevent the movement of the habit planes for reverse transformation, leading to the accumulation of plastic strains via the accumulation of residual martensite, and hence an increase in residual/irrecoverable strain. This in turn leads to the functional fatigue of the material [39]. Dislocation pile up from continuous cycling will cause a saturation of functional degradation, as seen with the stabilization of stress-strain curves or with strain evolution seen in Figure 1.9. It is apparent that dislocation generation and movement are major contributors in all types of fatigue.

According to Kang et al. [40], at cyclic stabilization, the material goes from dislocation dominated micro crack formation to micro crack propagation. This means that the transition can be characterized macroscopically. However, the transition from micro crack propagation to macro crack propagation and eventual failure can not be determined in such a way as the stress-strain response show no significant changes once the curves stabilize. This also means that distinguishing between crack initiation and propagation is not possible (total fatigue life = crack initiation + crack propagation). The accumulation of plastic strain is a consequence of increasing internal damage caused by the movement and pile up of dislocations at phase interfaces, increasing defect density and associated internal stresses that can lead to local plastic flow. Although this makes up a part of the total plastic/irrecoverable strains, a large part of the irrecoverable strain consists of residual martensite caused by micro-structural irreversibility due to the prevention of the movement of the habit plane as discussed earlier. These stabilized martensitic regions make up what is commonly known as transformation induced plasticity (TRIP). Both mechanical and actuation fatigue are characterized by accumulation of irrecoverable strains including stabilized martensite throughout the life of the material, indicative of similar mechanisms of dislocation generation and motion, with eventual crack formation and functional degradation, leading to failure. A study by Carmine et al. [41] shows heavy accumulation of martensitic regions near the fracture surface of a thermomechanically cycled NiTi dogbone shown by the use of atomic force microscopy (AFM), that alludes to the formation of martensitic plastic regions in the wake of the propagating crack.

It is imperative to understand how the loading conditions and repeated cycling of a SMA based actuators effects its longevity or fatigue life and its performance (i.e. cyclic or functional stability) throughout its life. A great deal of studies has been conducted on the actuation fatigue response of NiTi-based SMA's. Lagoudas et al. carried out novel thermomechanical fatigue testing to study fatigue and transformation characteristics of SMA's for high number of cycles [42]. Lagoudas et al. carried out actuation testing on NiTiCu wires at different stress levels and heat treatments, presenting results for ideal heat treatments and plastic strain accumulation [43]. Miller et al. carried out thermomechanical testing on NiTi and NiTiCu SMA's along various thermomechanical paths to characterize plastic strain accumulation for SMA actuators [44]. Bertacchini et al. [45, 46, 47, 48] in multiple studies characterized thermomechanical fatigue properties and cyclic behaviors of NiTi and NiTi-based SMA actuators. Wheeler at al. carried out thermomechanical fatigue characterization of NiTI SMA at various heat treatments and loading paths to calibrate a constitutive damage model [49]. Wheeler et al. carried out thermomechanical fatigue on SMA plate [50] and axial actuators [51] for lifetime predictions. In recent years, studies on HTSMAs such as NiTiHf due to its recent relevance and potential for application has garnered increasing interest in its actuation fatigue properties. Denowh et al. carried out thermomechanical training and characterization of NiTiHf and NiTiHfCu SMA's to study its effectiveness to be used in linear actuators [52]. Studies to determine and analyze ideal materials and compositions [29, 53, 54], effects of applied stress [55], temperature [56], and partial cycling [57] on actuation work output and fatigue life, characterizing microstructural reversibility and dimensional stability [58], transformation temperatures [59, 60] and fatigue resistance [54, 56, 55] showcase recent developments in this area. Ni-rich nano-precipitated NiTiHf SMAs have shown to possess some of the best properties in terms of dimensional stability and transformation temperatures. However, studies on NiTiHf pseudoelasticity remain scarce.

1.4 Motivation and Objective

In Haghgouyan et al., ‘A unified description of mechanical and actuation fatigue crack growth in shape memory alloys,’ the correlation between actuation and mechanical fatigue crack growth is derived using a single empirical power-law expression to provide a unified description of thermomechanical fatigue crack growth using the J-integral [61] (see Figure 1.11). To study and model crack growth rates, the authors conducted fast mechanical crack growth tests on disk compact tension specimens, along with actuation crack growth tests, which generally take much longer than mechanical tests due to their dependence on heating and cooling rates. Using a modified version of the Paris law crack growth equation, replacing the stress intensity factor ΔK with the energy density parameter ΔJ from the J-integral, the authors realized a correlation between actuation and mechanical crack growth when plotting ΔJ values against dN/da, the crack growth rate, describing them using a single equation. This showed the ability to predict actuation crack growth from mechanical and vice-versa. From the graph, all actuation tests are concentrated at the top right, where crack growth rates are high. This is because conducting actuation fatigue crack growth tests as low ΔJ values corresponding to mechanical fatigue would render very long test times.

Based on the success of unifying fatigue crack growth, uniaxial tensile mechanical fatigue tests were carried out to identify any correlation between tensile actuation and mechanical fatigue. Unlike crack growth tests, tensile fatigue concerns itself with total fatigue life (crack initiation + crack growth). The primary motivation of using mechanical fatigue as a predictor of actuation fatigue is long test time of the latter, similar to the crack growth tests. This stems from the contrast between time-consuming actuation fatigue experiments due to slow heating and cooling rates, and much faster mechanical tests due to high loading rates. During thermal cycling, a single heating and cooling cycle can take an average of 1 minute (10000 cycles = 1 week), with high cycle fatigue tests taking on the order of days to weeks to complete. Comparatively, a single loading and unloading cycle during mechanical cycling during these tests can take 1 second (10000 cycles = 2 hours 45 mins), with high cycle fatigue taking mere hours.

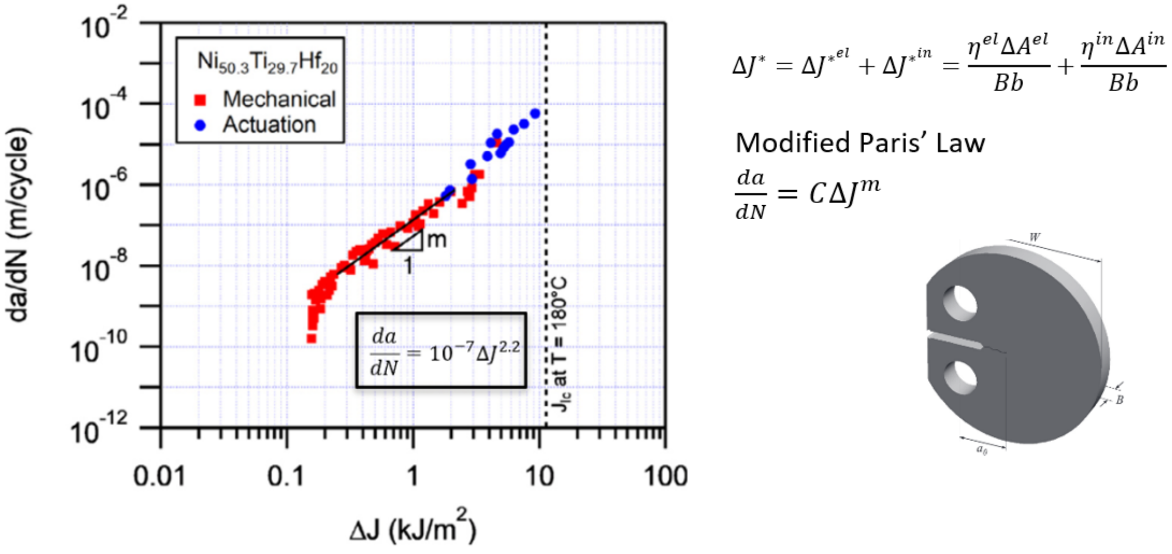

Figure 1.11: Unified Approach for Mechanical and Actuation Crack Growth Rates Using J-Integral (Reprinted with permission from [61])

Two objectives are identified. The first objective is concerned with the structural fatigue properties and the characterization of NiTiHf SMAs through experimental means, and to compare it to actuation fatigue data in an effort to achieve similarity between the two types of fatigues. Three compositions of Ni-rich NiTiHf SMAs are considered for the study: $Ni_{50.3}Ti_{29.7}Hf_{20}$, $Ni_{50.5}Ti_{33.5}Hf_{16}$, $Ni_{50.6}Ti_{30.6}Hf_{19}$. Given that SMA characteristics are highly sensitive to composition, the fatigue data from different materials would assess the repeatability of such an approach. The first composition $Ni_{50.3}Ti_{29.7}Hf_{20}$ has been the target of many studies mentioned earlier due to its promising actuation and fatigue response that make them a leading candidate for use in actuator systems. Before the mechanical fatigue tests, a characterization scheme is carried out to extract parameter values for critical yield stresses, phase diagram temperature-stress slopes, transformation temperatures, Young's Modulus etc. of the alloys in question. These tests allow for a reference on which to base required fatigue testing parameters on, including upper cycle stress (UCS) levels and test temperature for each material. Upon completion of characterization, mechanical fatigue testing will characterize the alloy's mechanical fatigue responses. The modelling and predicting of fatigue lifetimes is carried out using power law formulations derived by various studies in literature, which are strain based, stress based, and strain-stress (energy) based approaches. Given both actuation and mechanical fatigue results, the end goal is to further develop an empirical model to fit both fatigue life trends using a single set of parameters, or a set of comparative equations in an effort to achieve similarity between the two fatigues when characterized by different thermomechanical paths and loading rates, providing for a unified descriptor of tensile thermomechanical fatigue.

The second objective deals with characterizing the functional fatigue response. To achieve this, a generalized routine coupled with a graphical user interface is developed in MATLAB software to automatically analyze pseudoelastic stress strain data. The routine is designed to extract metrics that fully describe a pseudoelastic curve for how many ever cycles necessary. Using this approach, the macroscopic evolution of metrics such as transformation stresses, transformation strain, plastic strains, and hysteresis can be characterized. Additionally, Digital Image Correlation (DIC) images that showcase the mesoscopic evolution of strains in the sample are also discussed. This work characterizes the functional fatigue trends of the same three precipitation hardened NiTiHf alloys to study and compare plastic strains accumulation trends and how it influences the pseudoelastic properties, and as such the stress-strain response of the material, providing for a phenomenological description of the relationship between the changes that are observed in the macroscopic stress strain response to the evolution of plastic strains. Using these tools, the evolution of the aforementioned metrics throughout a lifetime is analyzed for trends that can give valuable insight into the functional fatigue response and the factors that influence it.

2. MECHANICAL AND ACTUATION FATIGUE OF NITIHF SMAS

2.1 Materials and Manufacturing

Material was prepared using high purity elemental constituents via Plasma Arc Melting (PAM) for $Ni_{50.6}Ti_{30.4}Hf_{19}$ and $Ni_{50.5}Ti_{33.5}Hf_{16}$, cast into 50.8 mm diameter ingots. $Ni_{50.3}Ti_{29.7}Hf_{20}$ was prepared using Vacuum Induction Skull Melting (VISM), cast into 30.5 mm diameter ingots. All casts were homogenized at 1050 $°C$ for 72 hours and furnace cooled before being hot extruded into individual 11 mm diameter bars at 900 $°C$ with an area reduction ratio of 7.7:1 for $Ni_{50.3}Ti_{29.7}Hf_{20}$ and 14 mm diameter bars at 900 $°C$ with an area reduction ratio of 9.2:1 for the remaining materials. The extruded rods were then cut into individual dogbone samples via wire electro-discharge machining (EDM), the dimensions of which are shown in Figure 2.2. The process is visualized in Figure 2.1. These dogbones are specifically used for mechanical fatigue testing done in this work. The one-inch gauge length is chosen to fit the one-inch length of the extensometer used in the tensile fatigue tests. A different set of sample geometry was cut for the characterization tests, shown in Figure 2.3. These samples were cut and heat treated in the same way as the tensile fatigue samples. These smaller samples were used for the thermal cycling characterization tests, with their smaller surface area allowing for reduced temperature gradient effects.

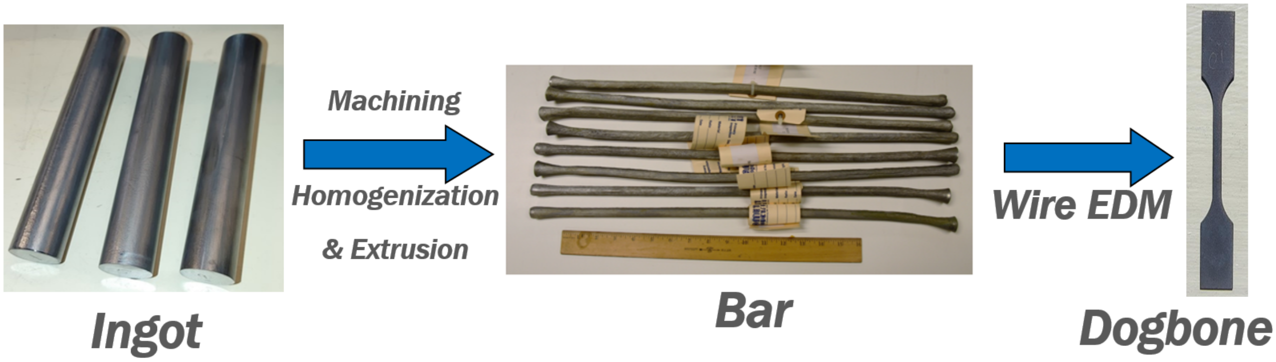

Figure 2.1: Material Production and Processing (Credit: Fort Wayne Metals)

Each sample is cut from bars extruded from homogenized ingots, transferring properties of the bulk material to each sample.

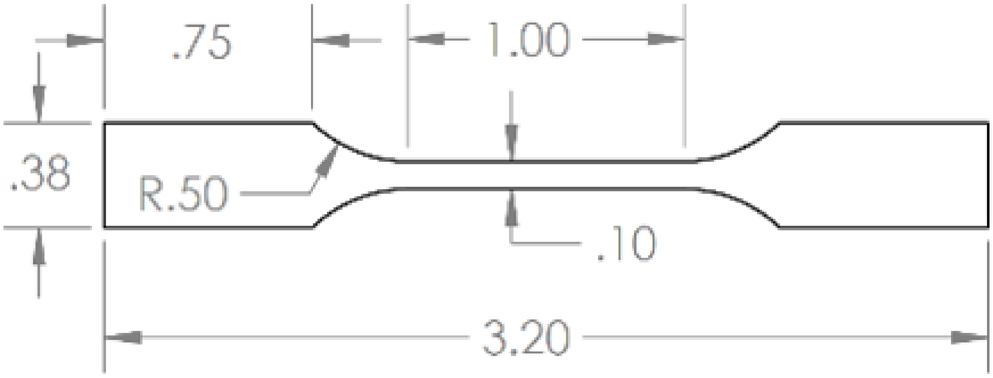

Figure 2.2: Dogbone Dimensions for Tensile Fatigue in **inches**

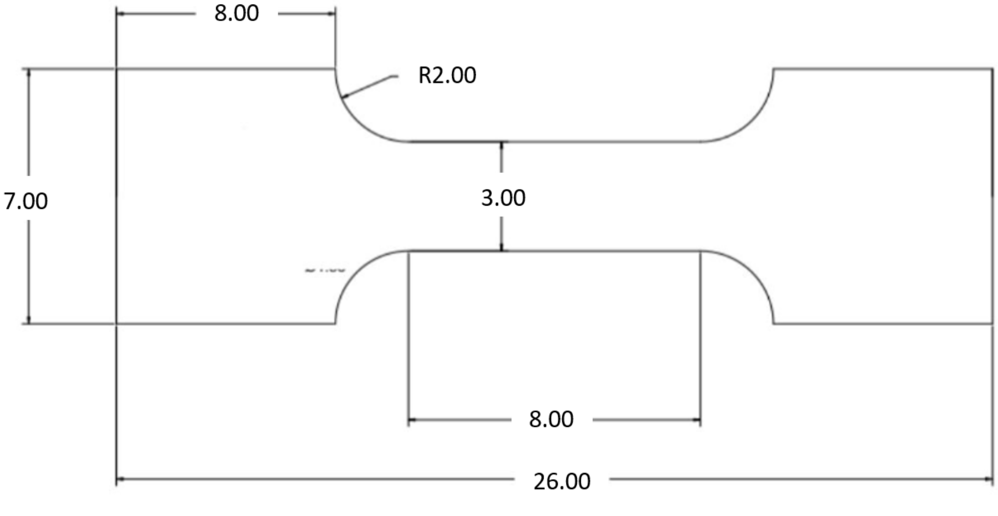

Figure 2.3: Dogbone Dimensions for Characterization in **mm**

2.2 Experimental Test Matrix and Setup

2.2.1 Test Matrix for Characterization

Characterization tests for the creation of a phase diagram were performed to extract pertinent information that will influence the values of the loading parameters of each material during mechanical fatigue tests. The test matrix for characterization tests in given in Table 2.1 below. To create a phase diagram, multi-stress level thermal cycling tests were carried out. This would be the main reference to determine loading parameters during mechanical fatigue tests, such as Upper Cycle Stress (UCS) levels based on the Martensite start (σ_{Ms}) and finish (σ_{Mf}) stresses, and test temperature based on the Austenite finish temperature at zero stress. Furthermore, tensile monotonic tests at 35 $°C$ and 25 $°C$ above A_f to characterize Young's Modulus of both phases were also carried out. These tests were carried out according to ASTM E8 criteria, defining a crosshead speed of 0.15 mm/min on the 1-inch gauge length dogbone samples. Strains were measured using an MTS contact extensometer. Some differential scanning calorimeter (DSC) results are showcased to point out similarity in transformation temperature values between DSC values and extrapolated values from thermal cycling tests. Hardness-Vickers tests were carried out on select samples to determine and validate ideal thermomechanical treatments. The following discussion showcases a detailed methodology for thermal cycling for the creation of a phase diagram.

Test Type	**No. of runs**
Multi Stress level thermal cycling	1
Tensile Monotonic pseudoelastic @ A_f+25 $°C$	1
Tensile Monotonic @ 35 $°C$	1

Table 2.1: Characterization Test Matrix

2.2.2 Characterization Setup and Results

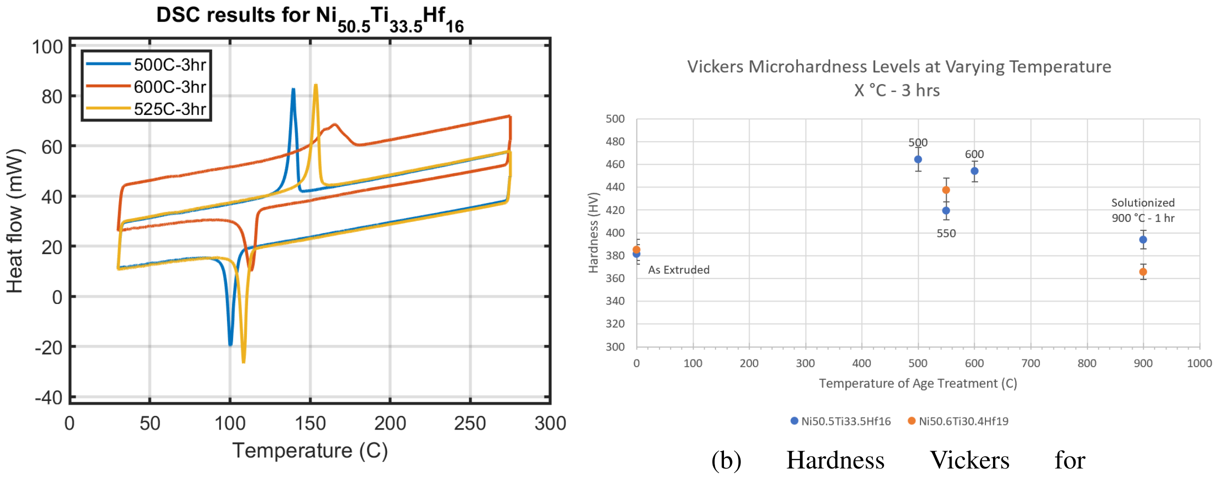

(a) DSC Curves for $Ni_{50.5}Ti_{33.5}Hf_{16}$

(b) Hardness Vickers for $Ni_{50.5}Ti_{33.5}Hf_{16}$ (blue) and $Ni_{50.4}Ti_{30.6}Hf_{19}$ (orange)

Figure 2.4: Characterization - DSC and Hardness

A heat treatment of 550 $^{\circ}C$ for 3 hours was set for all materials and samples. This heat treatment gives the material increased micro-hardness and enhanced plastic properties from the introduction of H-phase nano-precipitates which corresponds to increased martensite recovery or microstructural reversibility during reverse transformation. This increases cyclic stability, lowers hysteresis (energy dissipation) and retains ideal transformation temperatures [62]. This particular aging parameters corresponds to peak aging or highest micro-hardness level for $Ni_{50.3}Ti_{27.3}Hf_{20}$ materials. Figure 2.4b showcases the peak aging for $Ni_{50.5}Ti_{33.5}Hf_{16}$ and $Ni_{50.6}Ti_{30.4}Hf_{19}$ materials in terms of Hardness Vickers as a function of annealing temperature. It is inferred that peak aging exists between 500 $^{\circ}C$ and 600 $^{\circ}C$ and as such, the same heat treatment of 550 $^{\circ}C$ for three hours is applied on the remaining materials. This is also done for the sake of consistency between actuation and mechanical samples and between each composition. Figure 2.4a showcases the shift in Differential Scanning Calorimeter (DSC) curves for different heat-treatment temperatures, which correspond to an increase in transformation temperatures for the $Ni_{50.5}Ti_{33.5}Hf_{16}$

material. Since phase diagram results were used to determine stress level ranges for the fatigue tests, the nominal testing temperature which is a function of the Austenite Finish Temperature A_f were extracted from the phase diagram itself. It is seen that transformation temperature values from DSC correlate well with phase diagram results.

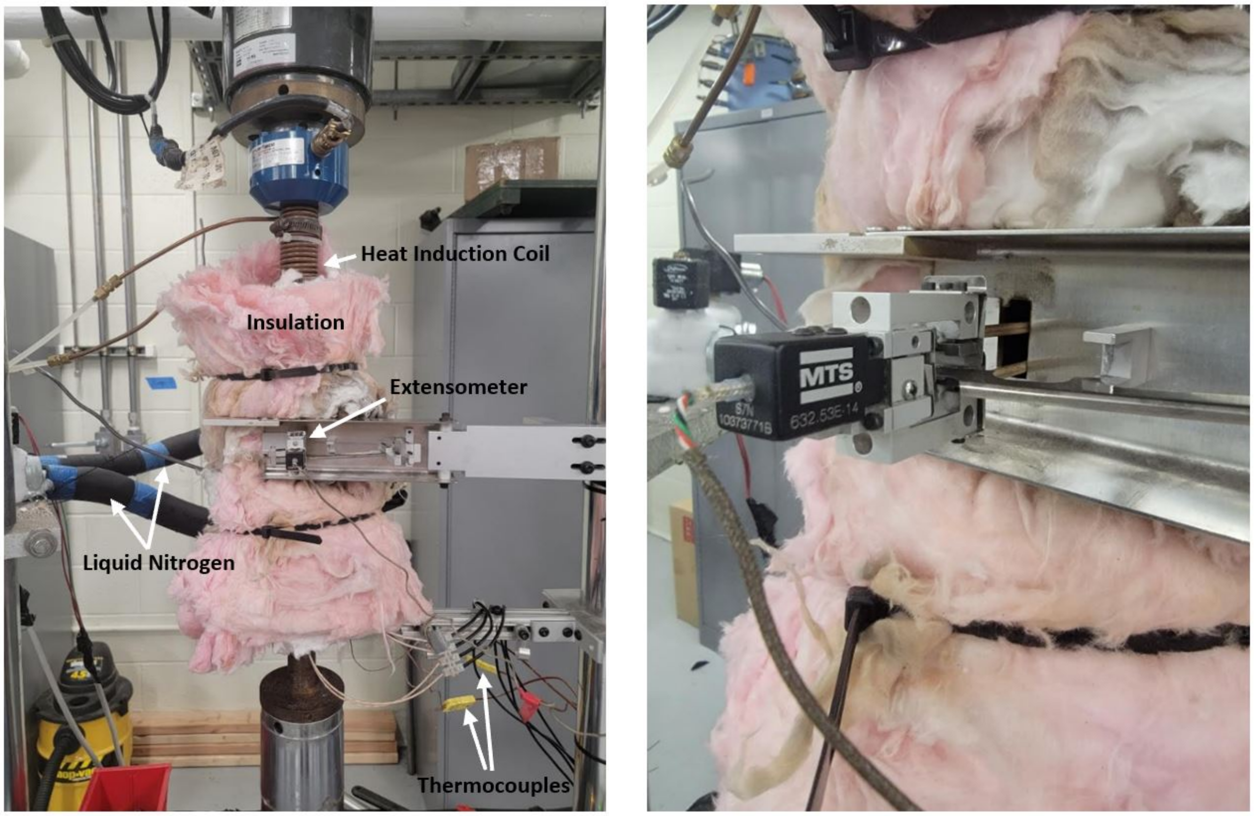

(a) Thermal Set Up

(b) Thermal Set Up - close up

Figure 2.5: Thermal Test Setup

Figure 2.5 above shows the test set up for the thermal cycling characterization tests. The characterization samples from Figure 2.3 were used for these tests. Small 1 mm diameter holes were drilled centered onto the grip faces. The sample was fixated on the frame grips with a heat treated steel rod through the holes in the grips and sample to prevent slippage. Heat induction was the primary method for heating the sample. Liquid nitrogen was the primary method for cooling. Insulation foam was wound around the sample area to isolate and insulate the sample during heating and cooling. A small area without insulation was kept in order to fix an MTS contact extensometer, which in turn was held up by an extensometer holder. A procedure was set up where heating and cooling rates were set at 10 $^\circ C$/min. Lower and upper cycle temperature were set at 30 $^\circ C$ and 300 $^\circ C$ respectively. A 10-minute hold was set in place at each temperature extreme before beginning each cycle for the sample to reach thermal equilibrium. After each heating and cooling sample, the applied load is changed via a linear ramp. The applied stress levels were 50, 100, 150, 200, 300, 400, 500, 600 MPa. These stress levels would provide enough data, while it was determined to be improbable that the samples would survive beyond 500 MPa. The corresponding temperature-strain curves are shown in Figure 2.7. The data generated from the cycles is then used to extract maximum transformation strain (H_{cur}), and the transformation temperatures using the tangent line method for each cycle (see Figure A.1c in **APPENDIX A**). This gives the four temperature transformation values at each stress level. The slope of the tangent line in the pure phase regions gives the thermal expansion coefficients (see Figure 2.6c). With this, enough information to form the phase diagram is available. The phase diagram with transformation temperature data is shown in Figures 2.8a, 2.9a, and 2.10a. The maximum transformation strains (H_{cur}) are shown in Figures 2.8b, 2.9b, and 2.10b. Figure 2.6a and 2.6b shows how the Martensite and Austenite Young's Modulus are calculated, respectively. Values are tabulated in Table 2.2.

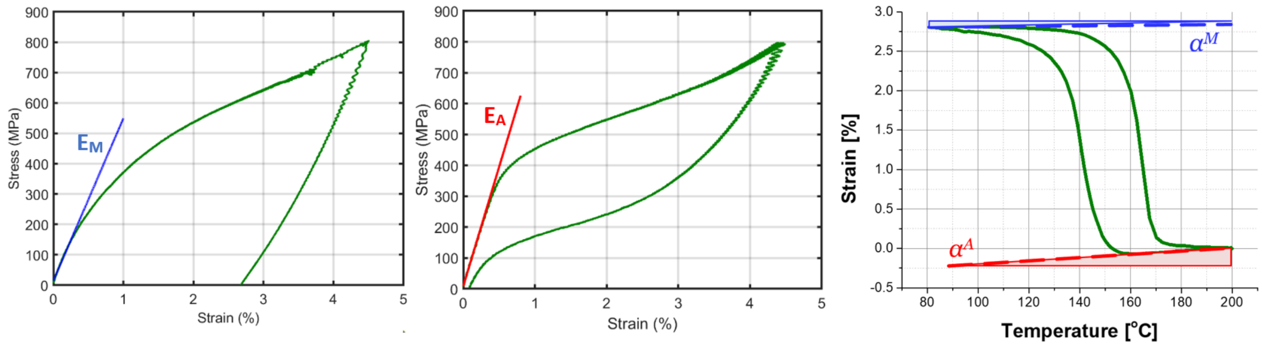

a) Martensite Modulus ($T = 35$ °C)

b) Austenite Modulus ($T = A_f + 25$ °C)

c) Thermal Expansion Coefficient

Figure 2.6: Calculation of Young's Modulus and Thermal Expansion Coefficient

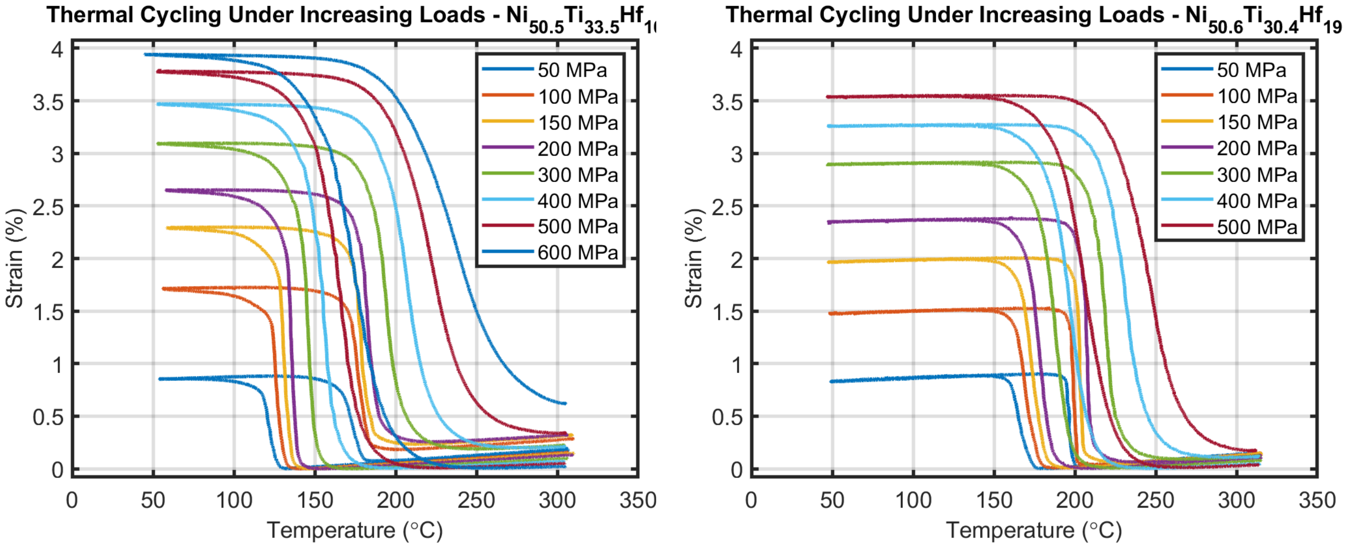

(a) Thermal Cycling - $Ni_{50.5}Ti_{33.5}Hf_{16}$

(b) Thermal Cycling - $Ni_{50.6}Ti_{30.4}Hf_{19}$

Figure 2.7: Thermal Cycling Raw Data

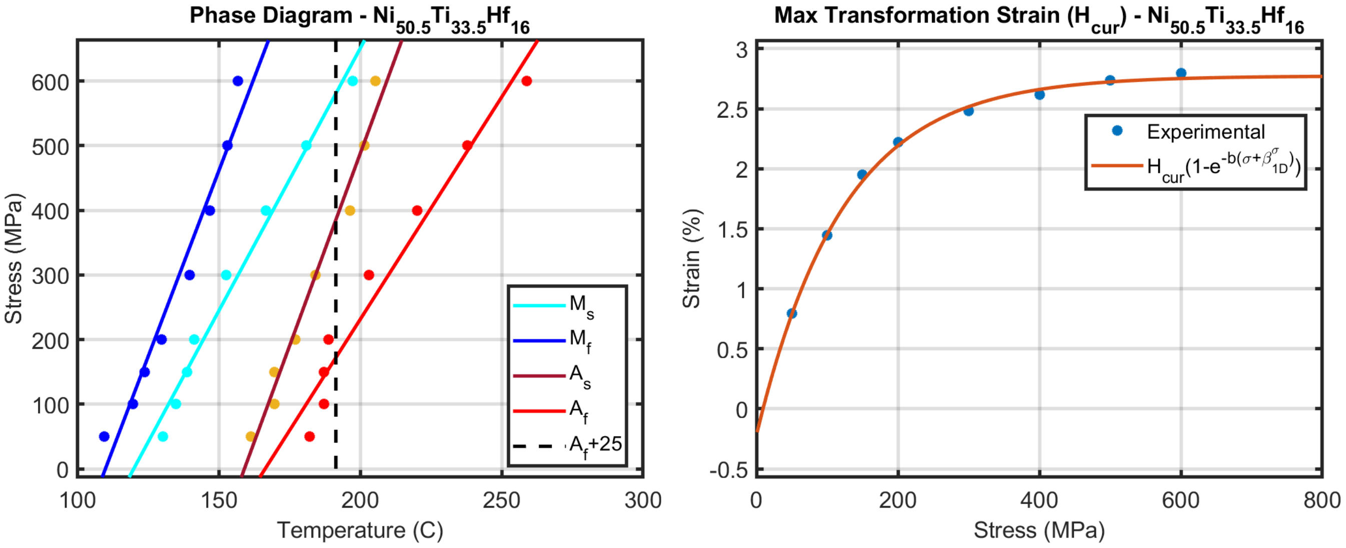

(a) Phase Diagram

(b) Max Transformation Strain

Figure 2.8: Characterization Results for $Ni_{50.5}Ti_{33.5}Hf_{16}$

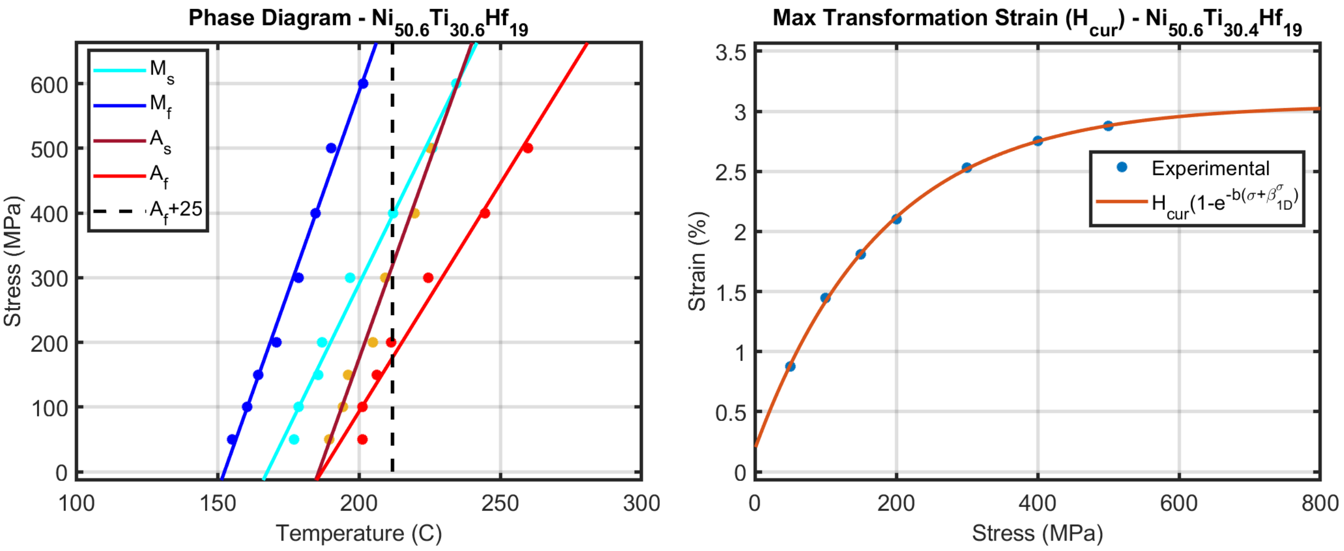

(a) Phase Diagram (b) Max Transformation Strain

Figure 2.9: Characterization Results for $Ni_{50.6}Ti_{30.4}Hf_{19}$

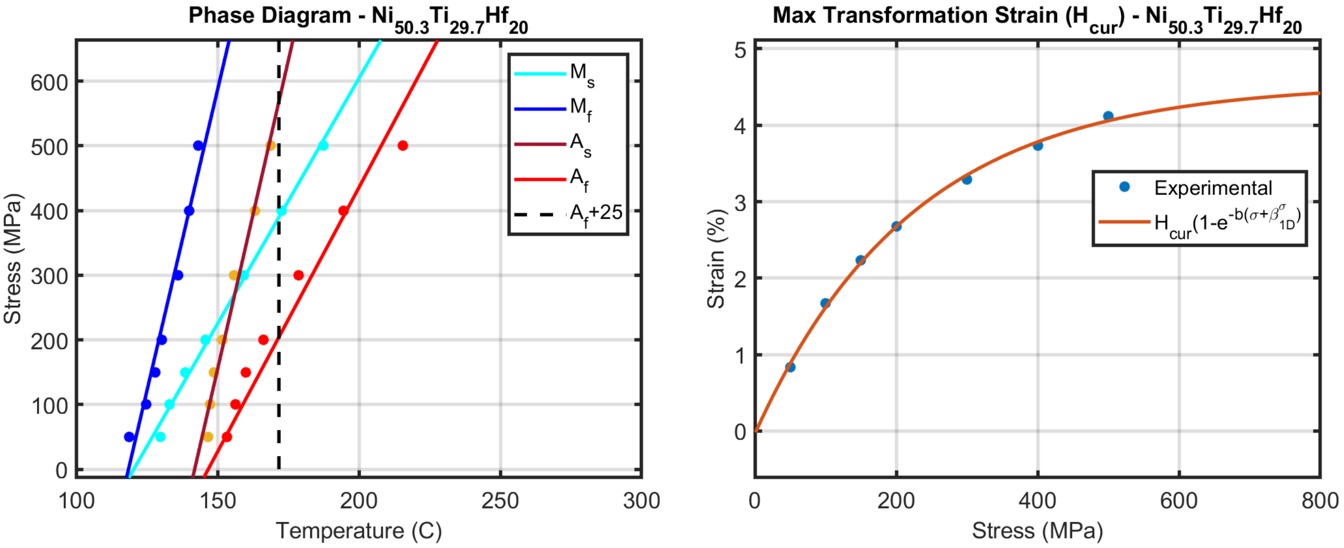

(a) Phase Diagram (b) Max Transformation Strain

Figure 2.10: Characterization Results for $Ni_{50.3}Ti_{29.7}Hf_{20}$

Results from the characterization tests are tabulated in Table 2.2 below.

Symbol	**Description | Unit**	$Ni_{50.6}TiHf_{19}$	$Ni_{50.5}TiHf_{16}$	$Ni_{50.3}TiHf_{20}$
E_A	Austenite Modulus | GPa	77.19	68.32	68.17
E_M	Martensite Modulus | GPa	64.52	47.37	57.34
v	Poissons Ratio | -	0.3	0.3	0.3
α_A	Thermal Expansion Coefficient of Austenite | %/$°C$	1.18e-3	1.027e-3	1.17e-3
α_M	Thermal Expansion Coefficient of Martensite | %/$°C$	6.29e-4	4.35-4	3.1e-4
M_s	Martensite Start Temperature at zero stress | $°C$	167.6	120	120.34
M_f	Martensite Finish Temperature at zero stress | $°C$	152.5	110	118.52
A_s	Austenite Start Temperature at zero stress | $°C$	185.8	159.1	141.92
A_f	Austenite Finish Temperature at zero stress | $°C$	186.9	166.42	146.72
C_{As}	Stress Influence Coefficient Austenite Start | MPa/$°C$	12.23	11.92	19.07
C_{Ms}	Stress Influence Coefficient Martensite Start | MPa/$°C$	8.95	8.13	7.59
C_{Af}	Stress Influence Coefficient Austenite Finish | MPa/$°C$	7.06	6.88	8.17
C_{Mf}	Stress Influence Coefficient Martensite Finish | MPa/$°C$	12.34	11.5	18.62
H_{cur}	Maximum Transformation Strain | %	2.98	2.81	4.55
β^{σ}_{1D}	1D Back Stress | MPa	11.42	-9.41	-1.83
k_t	Variation Rate of Transformation Strain with Stress | MPa^{-1}	0.0064	0.0074	0.0045

Table 2.2: Material Properties and Model Parameters

2.2.3 Test Matrix for Mechanical Fatigue

Upper cycle stress (UCS) levels are the only loading parameter that are varied between each sample, as this dictates the level of transformation and potentially, corresponding fatigue lifetime, forming a trend on fatigue life (S-N curve). At least five different stress levels are chosen to test at, with two repeats (total of three) for certain stress levels (Table 2.3 and 2.4). The stress levels and temperature determinations in Tables 2.3 and 2.4 above respectively are based off of the phase diagrams created from the multi-stress thermal cycling tests. As such, UCS values are between the Martensite Start (σ_{Ms}) and Martensite Finish Stresses (σ_{Mf}) of the material (see Figure 2.11). UCS's within this range were chosen such that the materials retains a sufficient fatigue lifetime range to model a lifetime trend that would also overlap with actuation fatigue lifetimes ($N_f > 10^4$), and as such, not fail too quickly (e.g. less than 100 cycles). A loading rate of 1 hertz was chosen that provided for fast testing while minimizing thermomechanical coupling effects caused by the generation and accumulation of latent heat and limit its effect on fatigue lifetime. More on the rationale behind the chosen frequency will be discussed in greater detail in section 2.3.2 regarding cyclic effects on sample temperature. The temperature is set to be $A_f^0 + 25°C$ where A_f^0 is the Austenite Finish Temperature at zero stress for each material. If the temperature were to be set higher, it would become increasingly difficult to transform without loading to very high stresses. Inversely, if the temperature were to be set lower, we risk not transforming completely upon unloading due to the fact that the linear fit used to model the Austenite Finish Temperatures as a function of stress (C_{Af}) tends to underestimate the A_f^0 value at stress levels near zero as seen in the phase diagrams for each material. Lastly, given the relatively low test temperature compared to the high melting point of the materials, vicsoplastic effects are considered negligible and not taken into account.

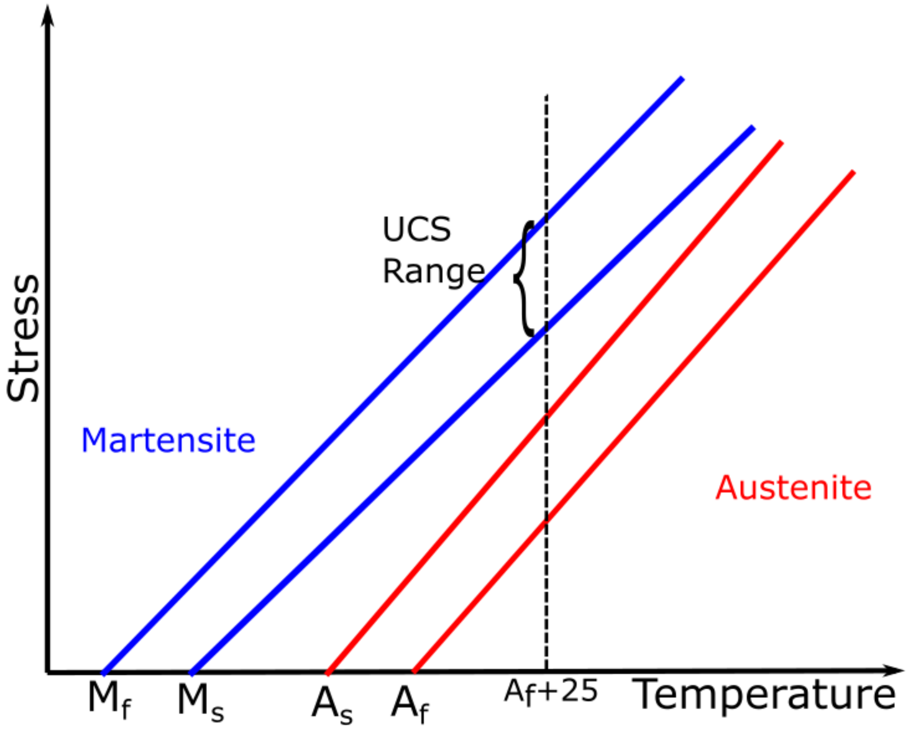

Figure 2.11: UCS Range Visual for Mechanical Fatigue

Stress Level (MPa)	$Ni_{50.5}TiHf_{16}$**-Runs**	$Ni_{50.6}TiHf_{19}$**-Runs**	$Ni_{50.3}TiHf_{20}$**-Runs**
375 MPa	-	-	1
400 MPa	-	3	3
425 MPa	-	-	3
450 MPa	-	3	1
475 MPa	-	-	3
500 MPa	3	3	1
525 MPa	1	-	3
550 MPa	3	3	1
575 MPa	1	-	3
600 MPa	3	3	-
625 MPa	1	-	-
650 MPa	3	1	-

Table 2.3: Tensile Fatigue Test Matrix - Upper Cycle Stress Levels

Parameter	$Ni_{50.3}Ti_{29.7}Hf_{20}$	$Ni_{50.5}Ti_{33.5}Hf_{16}$	$Ni_{50.6}Ti_{30.4}Hf_{19}$
Loading Control	Load Control	Load Control	Load Control
Loading Frequency	1 Hz	1 Hz	1 Hz
Temperature (A_f+25 $°C$)	175 $°C$	190 $°C$	210 $°C$
Upper Cycle Stress Range	575 to 375 MPa	650 to 500 MPa	650 to 400 MPa

Table 2.4: Tensile Fatigue Test Matrix

2.2.4 Mechanical Fatigue Setup

The fatigue tests have three different components - The tensile tester, LabVIEW interface and DIC (certain experiments). Heat treated samples were mounted in the 801 Material Test System servo-hydraulic frame with a maximum load capacity of 20 kips enclosed by an environmental chamber. The MTS software was used to set up a procedure for the fatigue tests. The procedure collected force, cross-head displacement via a linear variable differential transformer (LVDT), cycle/segment number, and time values at a rate of 100 data points a second. A 1-inch gauge length EPSILON high-temperature axial extensometer was attached to the sample itself using high-temperature silicon strips and springs. A close up of the sample in the frame is shown in Figure 2.12 below, along with a schematic of the test in Figure 2.13. The extensometer also recorded data at 100 data points a second. The procedure was set up such that the test would begin at a lower load level of 5 newtons. The sample would then be cycled at 1 Hz between 5 newtons and the input upper cycle load level applied as a sine wave input. Stress levels are based on the initial cross-section of each individual sample. This continues until the material fails. For certain experiments on the $Ni_{50.3}Ti_{29.7}Hf_{20}$, DIC images using correlated solutions Nikon Tokina lens on speckled samples were taken to showcase the evolution of localized transformation and plastic strains corresponding to potential irrecoverable/stabilized martensite regions. A speckle pattern is painted on the gauge length using white paint to contrast with the material's dark gray color. The DIC is set up such that 20 images are taken every 10^{th} of a second every 100 seconds. In other words, 20 images corresponding to two cycles are taken every 100 cycles. The images are then post processed in the VIC-2D software to extract strain contours.

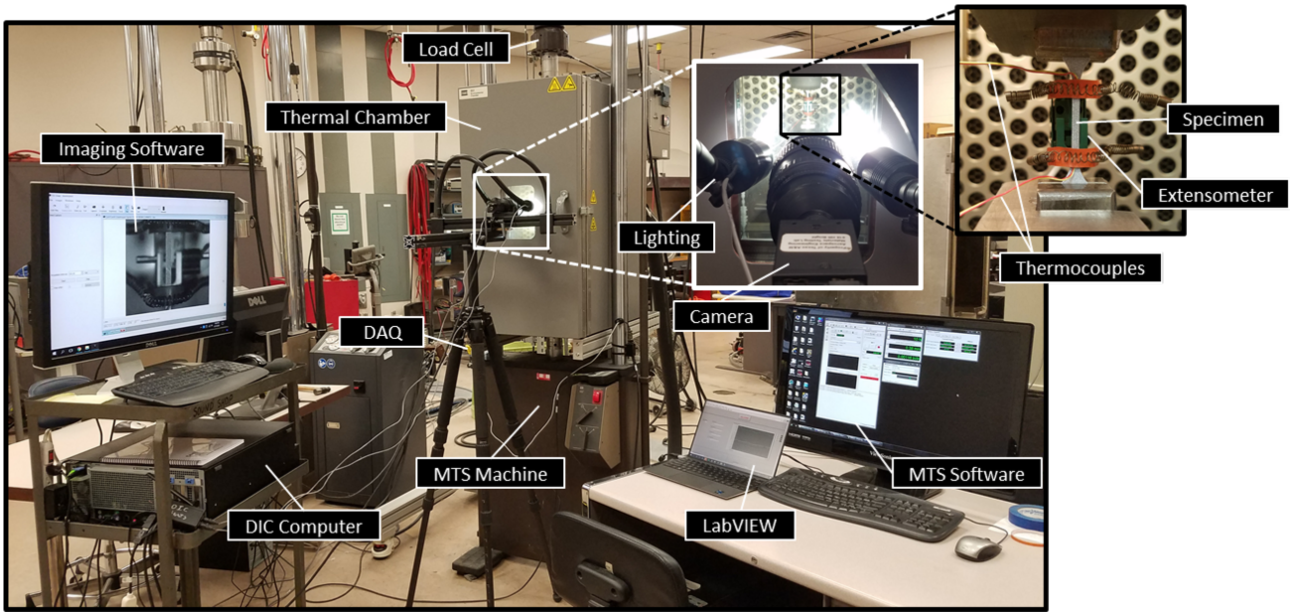

Figure 2.12: Mechanical Fatigue Test Setup

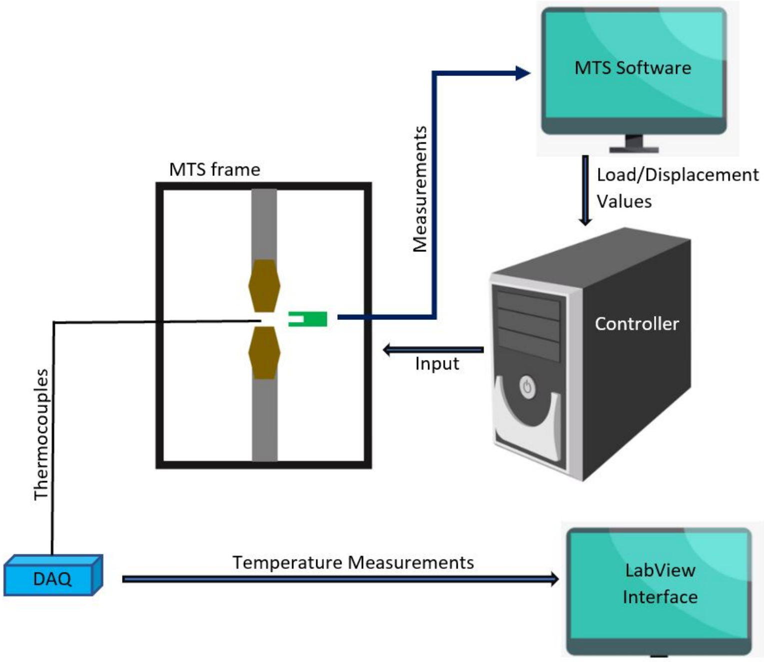

Figure 2.13: Mechanical Fatigue Test Schematic

Three type-k thermocouples are used to measure temperature in the heat chamber. Two of the thermocouples are fixed to the top and bottom of the mounted sample, secured by the silicon strips. This is also seen in Figure 2.12. The third thermocouple is free in the chamber to measure the ambient temperature. The information transmitted via the thermocouples is relayed via a Measurement Computing Data Acquisition (DAQ) board to a LabVIEW interface. During testing, the values, along with a moving plot of all three thermocouple data along with the average, is visualized. Temperature is collected in Celsius. Temperature data is collected at 25 data points per second, the maximum allowed data requisition rate given the tools and software used. All three systems worked in tandem during testing, with thermal probe beginning 5 seconds before the test is initiated.

2.3 Mechanical Fatigue Results and Discussion

2.3.1 Fracture Morphology

All tested samples, after failure, showcased a fracture surface perpendicular to the tensile load direction as shown in Figure 2.14. Fracture regions all occurred within the gauge section, with many fractures occurring at either ends of the 1-inch gauge section. Additionally, no necking or thinning features were noticed around the fracture surface regardless of upper cycle stress level, as also shown in Figure 2.14. Scanning Electron Microscopy (SEM) images of a $Ni_{50.6}Ti_{30.4}Hf_{19}$ fatigue sample lasting 12746 cycles is shown in Figure 2.15. The corner (right) image showcases river patterns near the right edge, corresponding to a probable crack initiation site. The smooth faceted regions showcase regions of quasi-cleavage steps in Austenite from stable crack propagation, which speaks to the brittle nature of fatigue fracture for NiTiHf SMAs. The left image shows a region near but within the fracture surface showing the transition from crack propagation to final rupture leading to failure. The rupture zone consists of a dense sea of randomly oriented ridges corresponding to unstable fracture through different Martensite variants. Images also showcase surface morphology, its texture and roughness attributes at failure, known in SMAs as a significant region for microcrack initiation [31]. It is well known that SMAs being intermetallic materials, exhibit brittle behavior.

(a) Fractured Samples - $Ni_{50.5}Ti_{33.5}Hf_{16}$ (Top; 500 MPa UCS), $Ni_{50.6}Ti_{30.4}Hf_{19}$ (Middle; 400 MPa UCS), $Ni_{50.3}Ti_{29.7}Hf_{20}$ (Bottom; 525 MPa UCS)

(b) Fractured Sample Close Up on $Ni_{50.5}Ti_{33.5}Hf_{16}$ Sample - 500 MPa UCS

Figure 2.14: Samples with Fracture Region

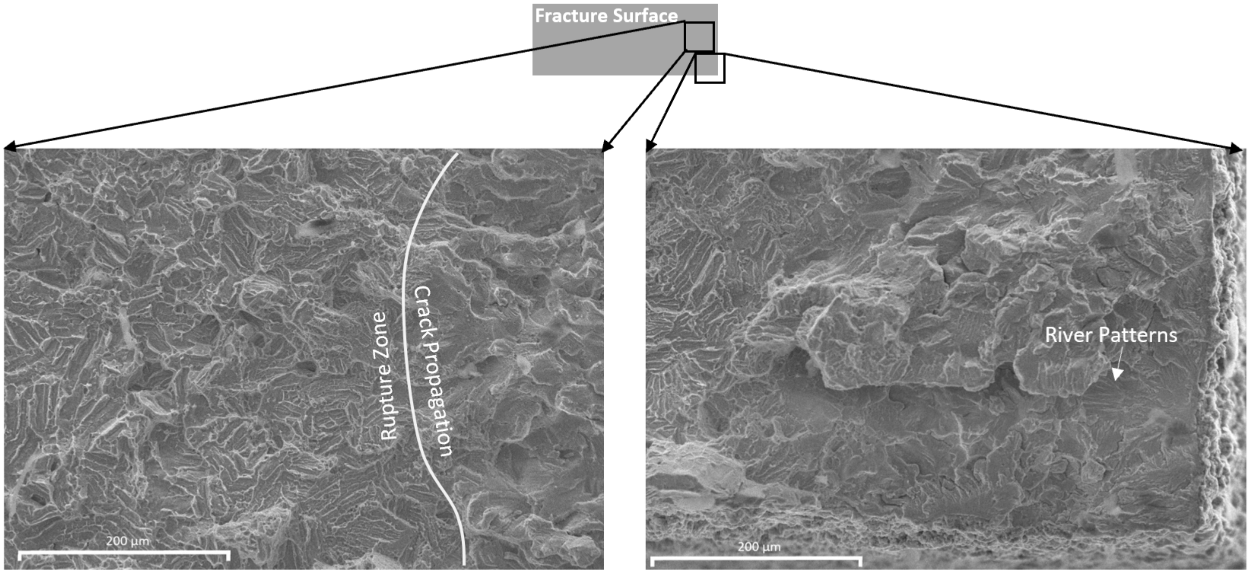

Figure 2.15: SEM Images of Fracture Surface of $Ni_{50.6}Ti_{30.4}Hf_{19}$ (400 MPa UCS - N_f = 12746)

2.3.2 Thermomechanical Coupling Effects from Cyclic Loading

During mechanical cycling, the stress-strain loading and unloading branches form a hysteresis loop. The phase transformation from Austenite to Martensite and Martensite to Austenite result in the release of net energy. The area between the curves correspond to the energy dissipation and hysteresis for the cycle. This energy is released in the form of heat, that can either be absorbed by the material or dissipated into the environment. At low strain rates, the dissipated energy has ample time to diffuse into the environment, leaving the temperature of the material unchanged after unloading as the energy diffused is equal to the energy that is dissipated by the material. However, as loading rate increases, so does energy dissipation per unit time. At high loading rates, the energy diffusing per cycle is lower than the energy accumulating from cyclic loading due to a small-time frame that allows dissipated energy from each cycle to diffuse to the surroundings. This net energy is then absorbed by the material that increases its temperature. The associated thermomechanical coupling changes the stress-strain and even fatigue response of the sample. As a result, SMAs are rate sensitive, and the loading rate plays a significant role in material response. It then becomes important to take into account the effect of loading rate set as part of the experimental design to prevent excessive effects of thermomechanical coupling from the absorption of latent heat.

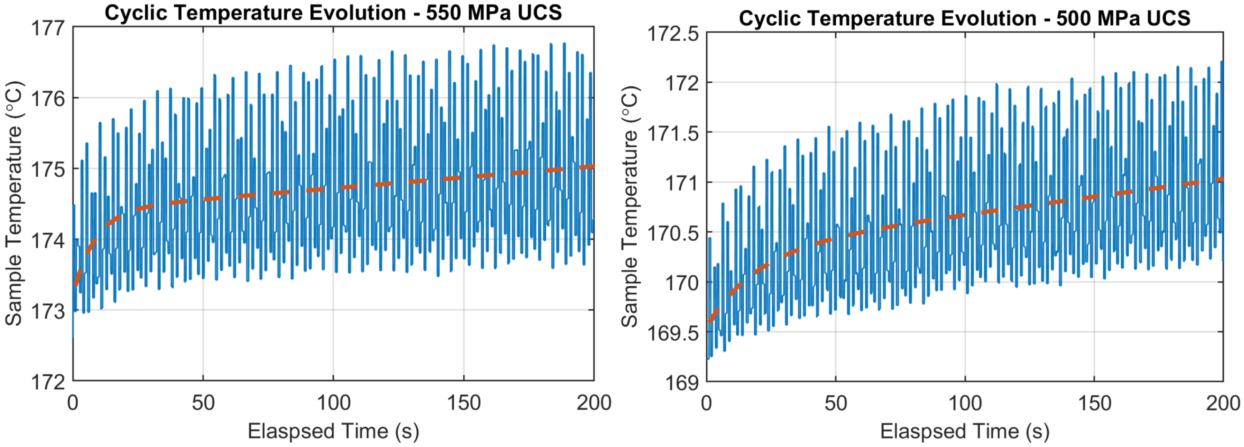

(a) 550 MPa UCS (b) 500 MPa UCS

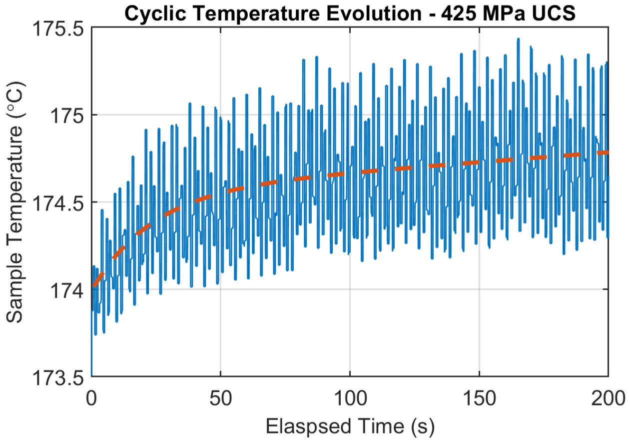

(c) 425 MPa UCS

Figure 2.16: Temperature Effects from Mechanical Cycling

Figure 2.16 above showcases oscillatory temperature fluctuations during the initial cycling for $N_f < 10^4$ (Figures 2.16a [550 MPa UCS] and 2.16b [500 MPa UCS]) and for $N_f > 10^4$ (see Figure 2.16c [425 MPa UCS]) for $Ni_{50.3}Ti_{29.7}Hf_{20}$. The first 200 seconds of each test (first 200 cycles) at a loading rate of 1 hertz are shown. Each 'line' within each graph corresponds to the temperature fluctuation. This particular temperature measurement corresponds to the thermocouple on the lower end of the gauge section of the sample. This is done via thermocouples embedded between the sample and a silicon strip. With all upper stress levels, there is a marked increase in sample temperature during initial cycling before reaching near asymptotic stabilization, in sync with stabilization seen during material training. During loading, temperature increases due to the forward transformation being an exothermic process, wherein energy dissipation in the form of heat is released. Upon unloading, the temperature decreases. As discussed earlier, the released energy may not have time to diffuse into the surroundings before the next cycle commences. Constant cycling leads to a pile up of dissipated energy that in turn heats the sample, leading to a mean temperature increase. As cycling continues, equilibrium is reached whereby the energy dissipated is equivalent to the energy diffused to the surroundings, leading to a saturation of sample temperature. From the figures, certain observations are made. Saturation occurs within the first 50 seconds (50 cycles), with higher stress levels observing faster stabilization. Second, amplitude of temperature fluctuations, and increase in mean temperature, is larger for higher stress levels. This is due to the higher degree of transformation and hence, larger energy dissipation associated with the stress level. The 550 UCS test shows an average total fluctuation of near 2.5 $^{\circ}C$, with 1.7 $^{\circ}C$ for the 500 UCS test, and 0.9 $^{\circ}C$ for the 425 MPa UCS. The increase in temperature from initial temperature to stable temperature corresponds to 1.3 $^{\circ}C$ for 550 MPa, 0.9 $^{\circ}C$ for 425 MPa, and 0.6 $^{\circ}C$ for 400 MPa. The gradual increase of the stabilized temperature is due in part from the environmental chamber continuing to heat the sample to equilibrium. It may be noted that the recording frequency for temperature measurements was limited to 25 data points per second, leading to the jagged and boxy nature of the curves. However, in the context of these experiments, the primary concern of temperature increase associated with the loading rate is studied, with the temperature increase and its effects on thermomechanical coupling considered to be inconsequential to the stress-strain response and functional properties of the materials.

Additionally, apart from temperature effects, the frequency can also affect fatigue lifetimes. Zhang et al. [34] conducted an experimental study on the frequency effects on low cycle pseudoelastic fatigue of NiTi. In these tests, they observed that for stress controlled tests, fatigue life as a function of frequency also depended on the applied stress level. At low stress levels (partial transformations), fatigue life stays stagnant until past about 1 hertz, when fatigue life increases dramatically. At high stress levels (near or at full transformation), the opposite is observed, wherein the fatigue life decreases with increasing loading rates. For in-between stresses, no change in fatigue life is seen with respect to a change in loading rates. Given this, it shows that a high loading rate can dramatically change the fatigue response. However, the stresses applied correspond to mid to low loads for the NiTiHf materials relative to their martensite start/finish stresses in this work. Furthermore, some in house tests to gauge the stress-strain response at different loading rates were conducted by Behrouz Haghgouyan as part of the ULI project (see Figure 2.17). The curves show increased stable response during initial cycling as loading rate increases from 0.2 hertz to 1 hertz. Additionally, a small reduction in the total and a significant reduction in the plastic strains (ratcheting) is also observed. Given the information presented so far, a loading rate of 1 hertz is chosen to allow for fast testing while limiting influence on fatigue lifetime, and a stable stress-strain response by minimizing changes in temperature due to thermomechanical coupling from latent heat accumulation.

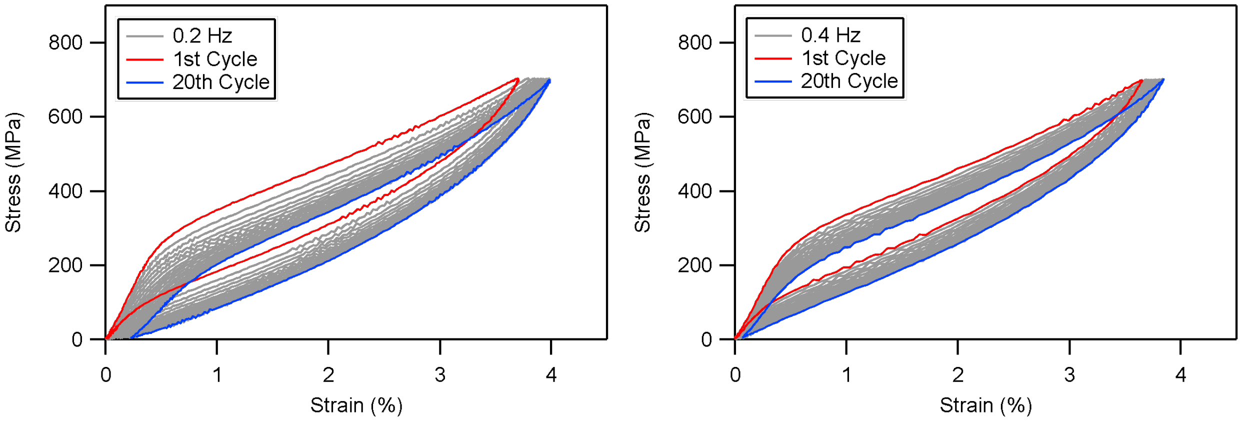

(a) 0.2 Hertz (b) 0.4 Hertz

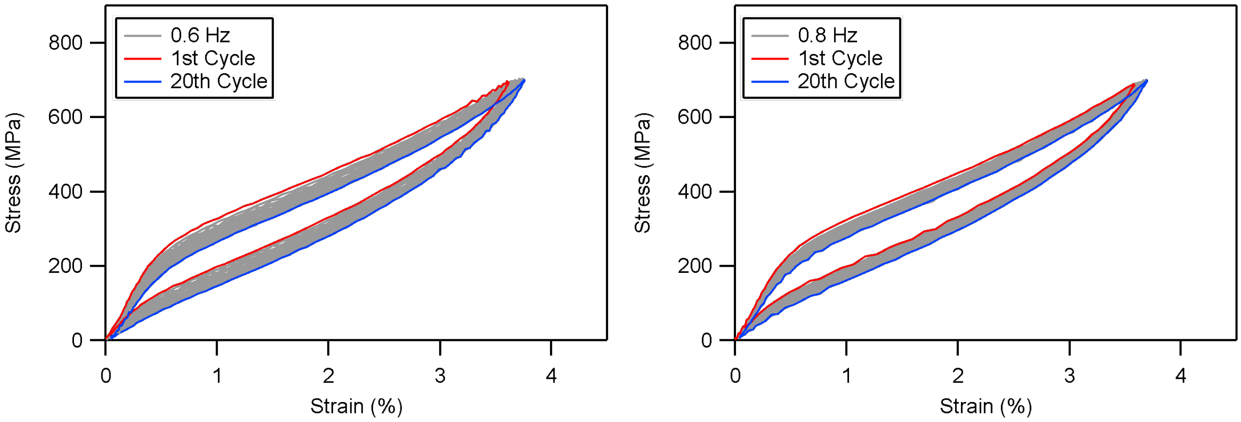

(c) 0.6 Hertz (d) 0.8 Hertz

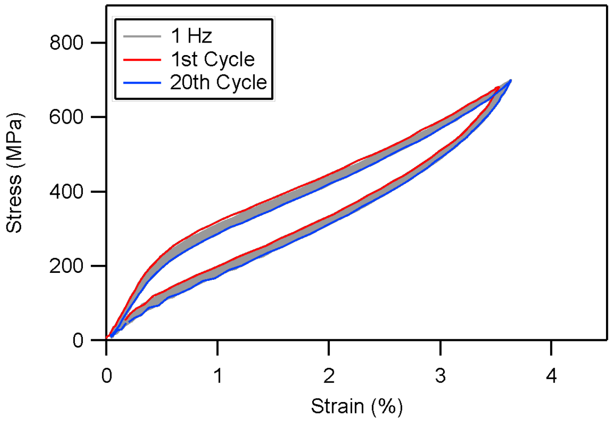

(e) 1 Hertz

Figure 2.17: Frequency Effects on $Ni_{50.3}Ti_{29.7}Hf_{20}$

2.3.3 Mechanical Fatigue Lifetime Modelling and Formulation

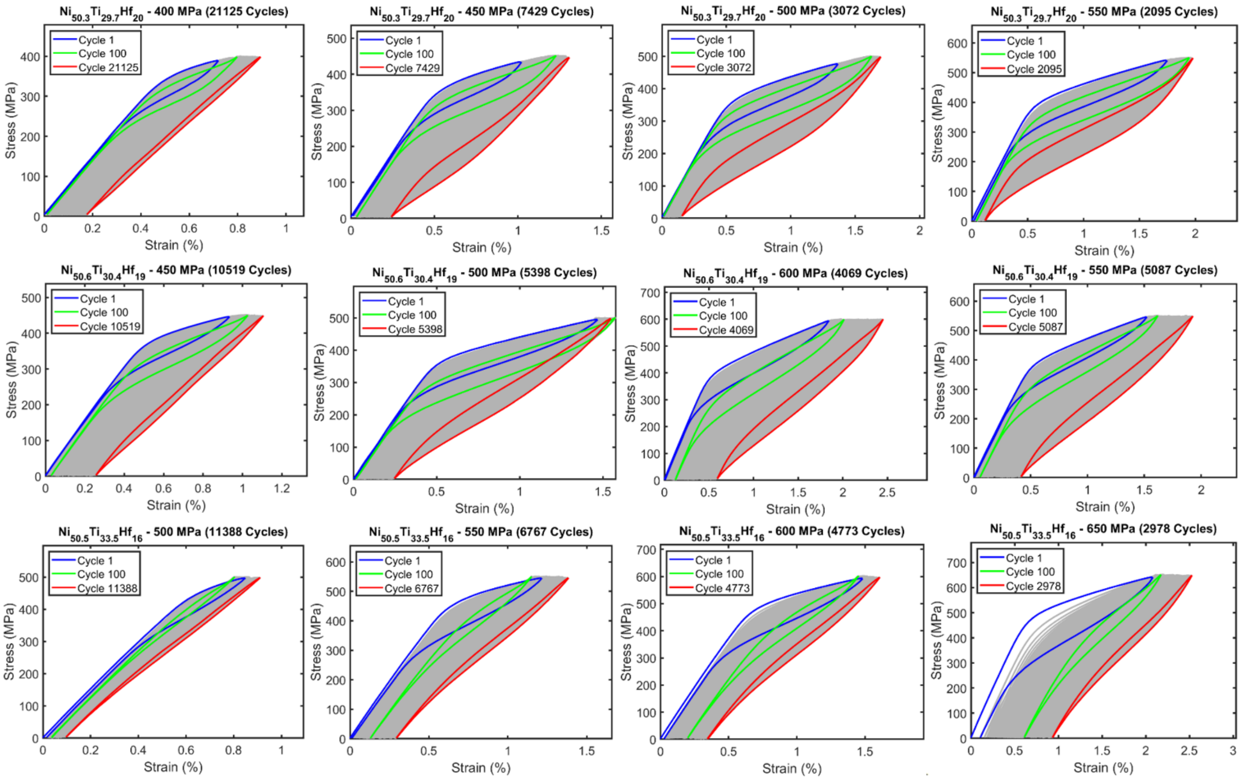

Figure 2.18: Mechanical Stress-Strain Curves (1^{st}, 100^{th}, Final Cycle at Failure) for all 3 Materials

Figure 2.18 shows the mechanical stress-strain curves across a range of upper cycle stress levels associated with each material (each row represents a different material). It is seen with all materials that with increasing UCS, comes an increase in recovered strain per cycle and with it, a higher degree of transformation (larger Martensite volume fractions), and a shortened fatigue life.

Modelling of fatigue in general has begun with the introduction of the Wohler S-N curves, which is based on the relationship between applied stress (S) or mean stress and fatigue life (N or N_f) using the power-law formulation $y = aN_f^b$, where y is the fit parameter, and a and b are material specific parameters. Fatigue modelling and prediction of SMAs is similar, with approaches that can be strain based, stress based or energy (stress-strain) based. Many SMA fatigue models are based on the empirical model first proposed as the Coffin-Manson approach, which used the plastic strain amplitude as a fitting parameter with fatigue life for conventional low cycle fatigue [63, 64]. Tobushi et al. [65] used strain amplitude along with temperature and frequency to estimate fatigue life. Maletta at al. [66] formulated a modified Coffin-Manson model by separating the elastic and inelastic (transformation) strains, allowing for a cohesive model to describe the transformation zone independently. Kollerov et al. [67] also formulated a modified Coffin-Manson equation to estimate fatigue life for SMAs undergoing large strain amplitudes. Lagoudas et al. [26] used the same empirical law approach to model fatigue life based on total plastic strains. The studies mentioned above make use of the different types of strain for the modelling of fatigue response. Many models that make use of energy based approaches have been formulated. Moumni et al. [68] formulated an empirical equation that predicts fatigue life using the dissipated energy (area between the hysteresis loops). Zhang et al. [69] extended the previous equation by including the effect of thermomechanical coupling on fatigue life arising from different strain rates. Zhang et al. [34] also studied the effect of loading frequency on thermomechanical coupling, temperature changes and fatigue life. In a different study [70], they also formulated a model for fatigue life prediction using stored energy. The stored energy arises from the idea that before reaching the shakedown state, some of the hysteresis work goes into dislocation motion and stabilized Martensitic regions, which can be used as a metric to predict failure. Song et al. [71] used the ratio between the total dissipated energy till the N^{th} cycle to the total dissipated energy till the final cycle. Calhoun et al. [72] used the critical plane stress-strain model by Smith-Watson-Topper (SWT parameter) to model SMA actuation fatigue life. The figures below (see Figure 2.19) showcase modelling of fatigue lifetime prediction using various parameters for all three compositions. These include the Smith, Watson and Topper (SWT) parameter ($\sigma_{max}\Delta\epsilon$), total strain energy ($\int \sigma d\epsilon$), energy dissipation ($\oint \sigma d\epsilon$), recovered strain ($\Delta\epsilon$) and upper cycle stress ($\sigma_{UCS}/\sigma_{max}$). As applicable, the values for these parameters corresponds to the 300^{th} cycle in each test, which is indicative of an ideal stabilized cycle after reaching the shakedown state. Refer to Figure A.1 and Table A.1 in APPENDIX A on the calculation of the parameters from the stress-strain response.

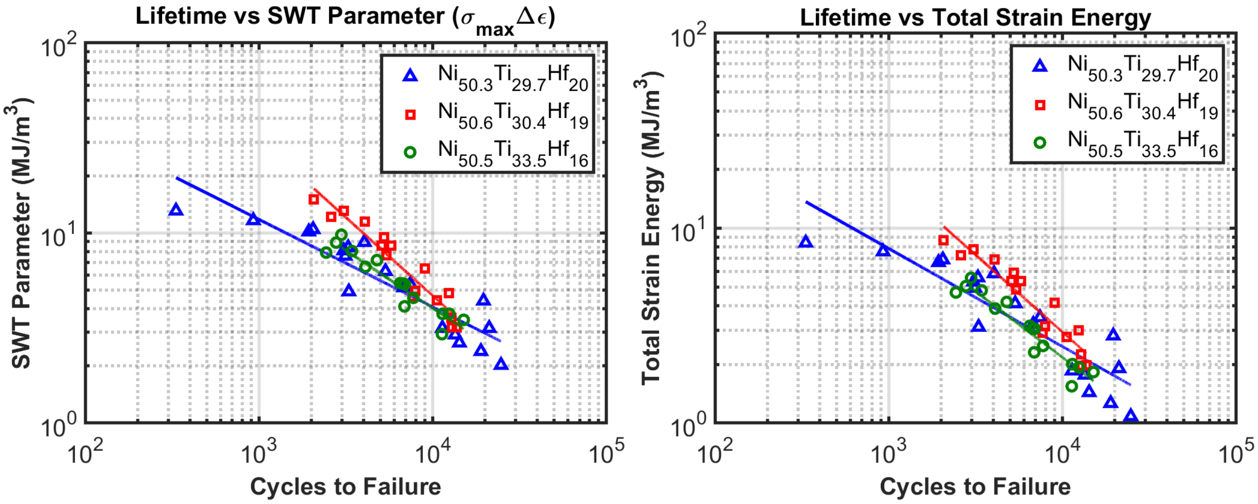

(a) SWT Parameter

(b) Total Stain Energy

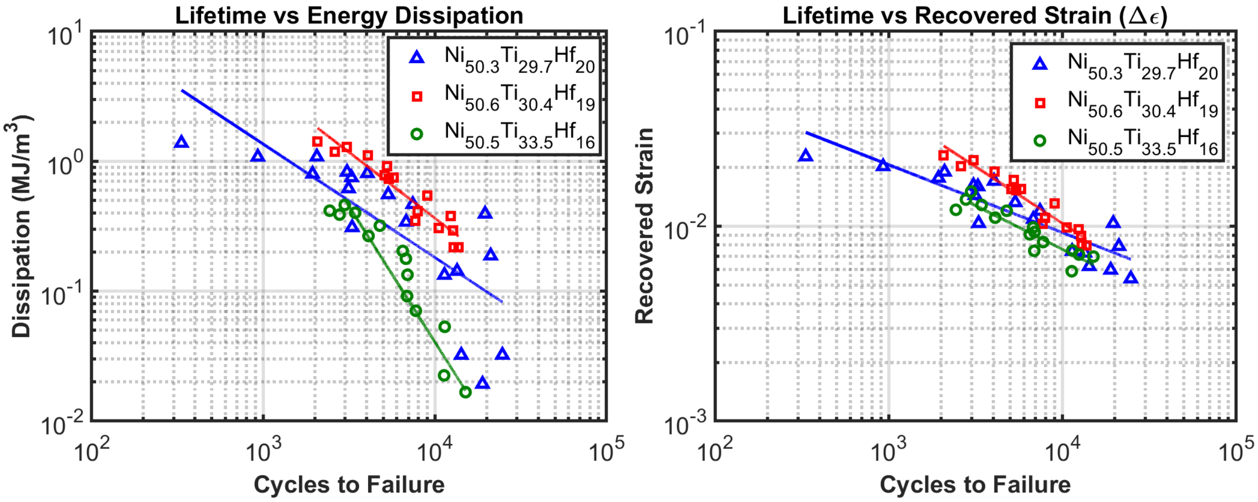

(c) Energy Dissipation

(d) Recovered Strain ($\Delta\epsilon$)

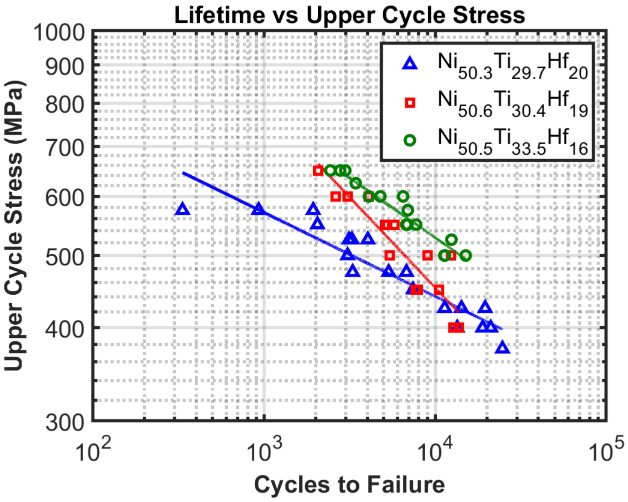

(e) Upper Cycle Stress

Figure 2.19: Mechanical Fatigue Trends

	$Ni_{50.3}Ti_{29.7}Hf_{20}$			$Ni_{50.5}Ti_{33.5}Hf_{16}$			$Ni_{50.6}Ti_{30.4}Hf_{19}$		
Coefficients	a	b	R^2	a	b	R^2	a	b	R^2
SWT Param	283.78	-0.46	0.83	9268.88	-0.82	0.9	1097.84	-0.61	0.91
Total Strain Energy	253.98	-0.5	0.8	4324.14	-0.79	0.91	1117.6	-0.68	0.9
Energy Dissipation	559.75	-0.87	0.62	4168.61	-1.02	0.82	9.123E6	-2.09	0.89
Recovered Strain	0.2288	-0.35	0.8	2.199	-0.58	0.85	0.476	-0.45	0.93
Upper Cycle Stress	1240.28	-0.11	0.87	4214.91	-0.24	0.93	2306.15	-0.16	0.83

Table 2.5: Mechanical Fatigue Trends - Power Law Coefficients

R-squared values in Table 2.5 indicate that the aforementioned parameters were able to aptly capture fatigue trends, showing definitive correlation. Among the three materials, $Ni_{50.3}Ti_{29.7}Hf_{20}$ shows the lowest R-squared values, especially when using energy dissipation ($R^2 = 0.62$) for the data points with fatigue lives greater than 10^4 cycles. At this point, a large scatter is seen. This is most likely due to the fact that at those high fatigue lives, the UCS values were near the σ_{Ms} values, which can vary between samples. As such, at these low UCS's, some samples may observe transformation and some may not and remain largely in the elastic response, allowing for a large variability in dissipation values.

2.4 Actuation Fatigue and Correlation with Mechanical Fatigue Data

The actuation fatigue tests were conducted on a custom-built test frame. Test specimens were dogbone shaped similar to the mechanical fatigue test specimens, with the only difference being a 40 mm gauge length for the actuation test specimens. All samples were also heat treated at 550 $^{\circ}C$ for 3 hours to induce nano-precipitates within the matrix. Required stress levels were reached using weights at room temperature, after which samples were heated to the upper cycle temperature (UCT) and subsequently cycled between the low cycle and upper cycle temperature until failure. Heating was implemented via joule heating, while a low speed electric fan was used to cool the samples. Heating and cooling rates were kept at approximately 15 $^{\circ}C/s$ and 8 $^{\circ}C/s$ respectively. This allowed the test frame to perform about 1500 thermal cycles per day. Displacement measurements were performed using a linear variable differential transformer (LVDT) sensor attached at the grips of the frame. Temperature was measured using a Micro-Epsilon CTLaser infrared thermometer at the center of the gauge section. The test procedure was controlled via a script in LabVIEW, which collected real time temperature, displacement, time, number of cycles to failure and peak displacements at each temperature extreme for each cycle. Stress levels for the tests were set between 300 and 400 MPa. LCT and UCT for full actuation tests were set at 40 $^{\circ}C$ and 300 $^{\circ}C$.

Partial heating actuation tests were carried out from 100% Martensite volume fraction (MVF) to values of 50/25/10% MVF (see Figure 2.20a). Initially, full temperature-control cycles were carried out to determine total accumulated actuation strain from 100% to 0% MVF. At this point, based on the desired MVF range, tests were then switched to strain-control to reach the desired actuation strain that reflects the final MVF value.

In the previous section, mechanical tests were conducted at varying upper cycle stress levels to allow for different levels of transformations and fatigue lives, that would allow for the creation of fatigue curves in the form of power law correlations to predict lifetime response of the material. Similarly, load levels and temperature range for actuation cycling is varied to produce corresponding changes in transformation and fatigue lives that would allow for the creation of similar power law correlations for actuation fatigue. It has been shown that actuation work output and fatigue lives for NiTiHf SMA's are sensitive to load levels and temperature range that dictates the level of transformation. The studies show that with increasing load levels, actuation strain increases at the expense of fatigue life for full transformation ($UCT > A_f$) [55]. For partial heating actuation cycles ($UCT < A_f$), where both loads and upper cycle temperatures were varied, it was shown that there is a considerable increase in fatigue life compared to full actuation cycling even when work output is the same [57]. It was also shown that these actuation fatigue lives were well captured using power law correlations using the average actuation work output.

Efforts to model fatigue life has led to the formulation of strain based, stress based, and strain-stress (energy) based equations. For conventional metals, strain based equations work well when plastic strains are large (low cycle fatigue), and stress based equations work well when plastic strains are negligible (high cycle fatigue). For SMAs however, due to its phase transformation capabilities dependent on parameters such as stress, strain and temperature, sole strain and stress based models may lack in encapsulating the complexity that phase transformation brings in. By using a stress based criterion such as stress amplitude $\sigma_a = aN_f^b$, material parameters *a* and *b* will have different values depending on the strains the material achieves despite the stress levels not changing, as in the case with partial and full transformations. Similarly, using a strain based criterion such as strain amplitude, $\epsilon_a = aN_f^b$ the *a* and *b* parameters will change based on the applied stress level despite the strain levels not changing. This is possible for both mechanical and thermal cycling due to the dependence of temperature on strain accumulation. Such parameters bring in dependence of loading conditions during fatigue modelling. As a result, a cohesive stress-strain critical plane model for conventional elastic-plastic material, first proposed by Smith, Watson and Topper (SWT) as the product between the maximum normal stress and corresponding normal strain is used as the predictive model for both actuation and mechanical fatigue in this section. It can be noted that the SWT parameter for actuation cycling corresponds to the area under its stress-strain curve, which is equivalent to the strain energy density and as such this parameter can also be seen as an energy parameter. This parameter can then be used to effectively model fatigue at any range of stress and strain values, adding an element of generalization for any set of loading conditions. Additionally, an added capability of this model allows us to not only predict fatigue lifetime, but to determine the loading conditions (stress and strain) needed to achieve said lifetime. Hereinafter, this model will be referred to as the actuation work output model, as referred in [72].

The definition of work output as it applies to actuation cycling is not wholly applicable to mechanical cycling due to the lack of a mechanical work 'output.' As a result, defining energy parameters for mechanical fatigue is open to interpretation. Actuation work output model $\sigma_{max}\epsilon_{actuation}$ [72] ($\epsilon_{actuation} = \epsilon_{recovered} = \Delta\epsilon$) is employed to predict lifetime and required loading conditions. Due to a lack of work output definition for mechanical cycling, a mechanical work equivalent of $\sigma_{max}\epsilon_{rec}$ or $\sigma_{max}\Delta\epsilon$, also based on the SWT parameter, is defined as visualized in the Figure 2.20. Partial heating and partial cooling (dotted blue lines) loading paths on the full actuation cycle (red) are also shown. Actuation work output utilizes the average ϵ_{act} of the cycles in each test, whereas mechanical work equivalent uses $\Delta\epsilon$ corresponding to the first cycle in each test. This is because during mechanical cycling, changes are observed in stress (for strain controlled tests) or strain (for stress controlled tests) values due to inevitable functional fatigue, which leads to changes in work equivalent values throughout life. This is unlike partial actuation tests, which were carried out using strain control, whereby $\sigma_{max}\epsilon_{rec}$ remains relatively constant despite changes in its functional properties from functional fatigue. As such, to remove this effect of functional fatigue on work equivalent values, the values corresponding to the first cycle during mechanical cycling are chosen.

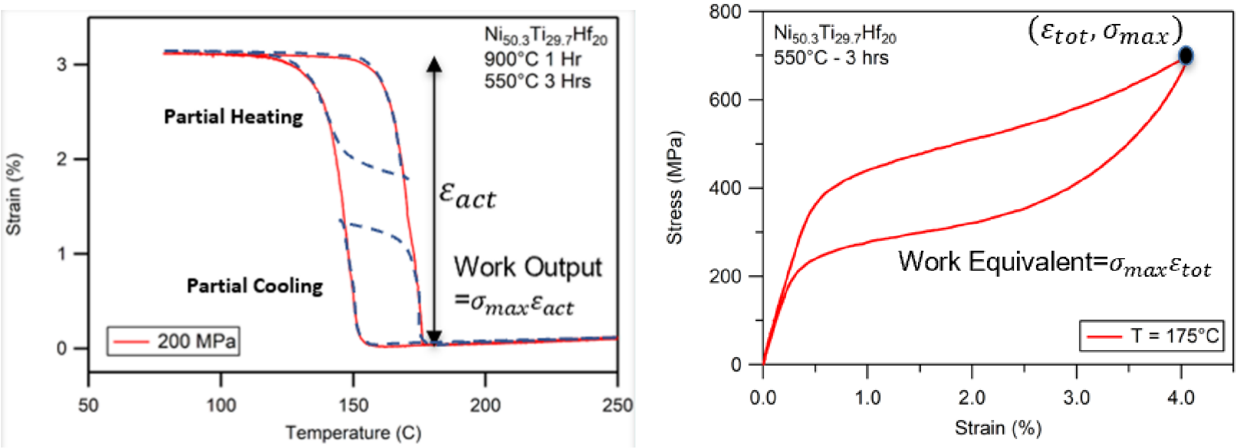

(a) Work Output for Actuation Cycling

(b) Work Equivalent for Mechanical Cycling

Figure 2.20: Work Output Definitions

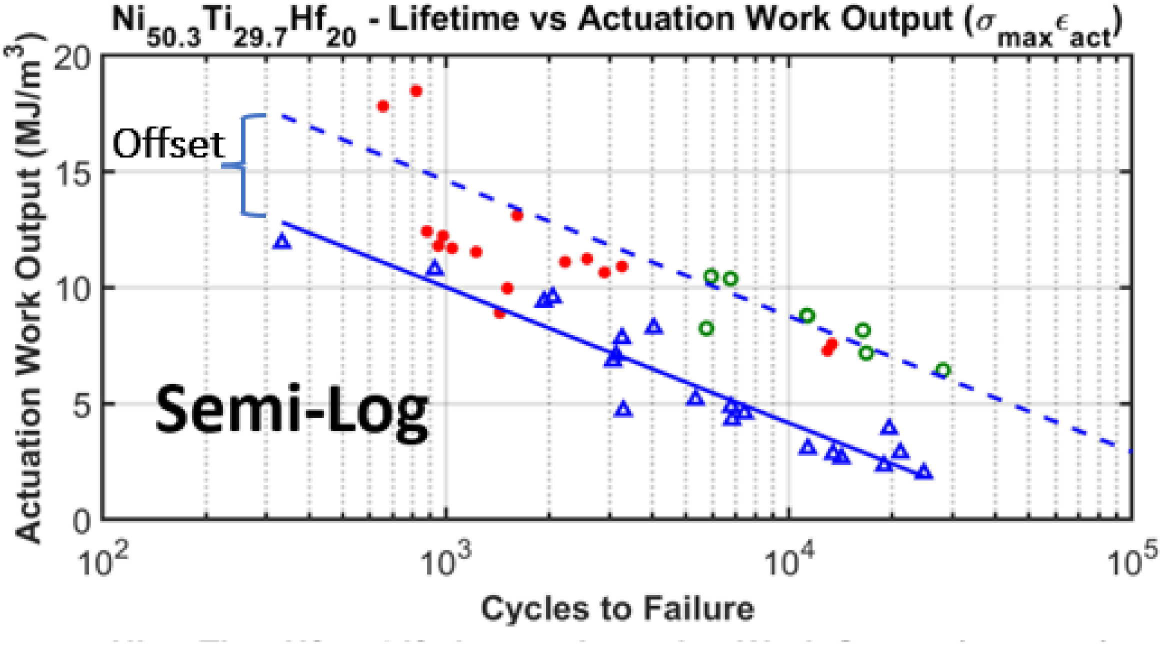

Figure 2.21: Work Output/Equivalent Curves for $Ni_{50.3}Ti_{29.7}Hf_{20}$-semilog

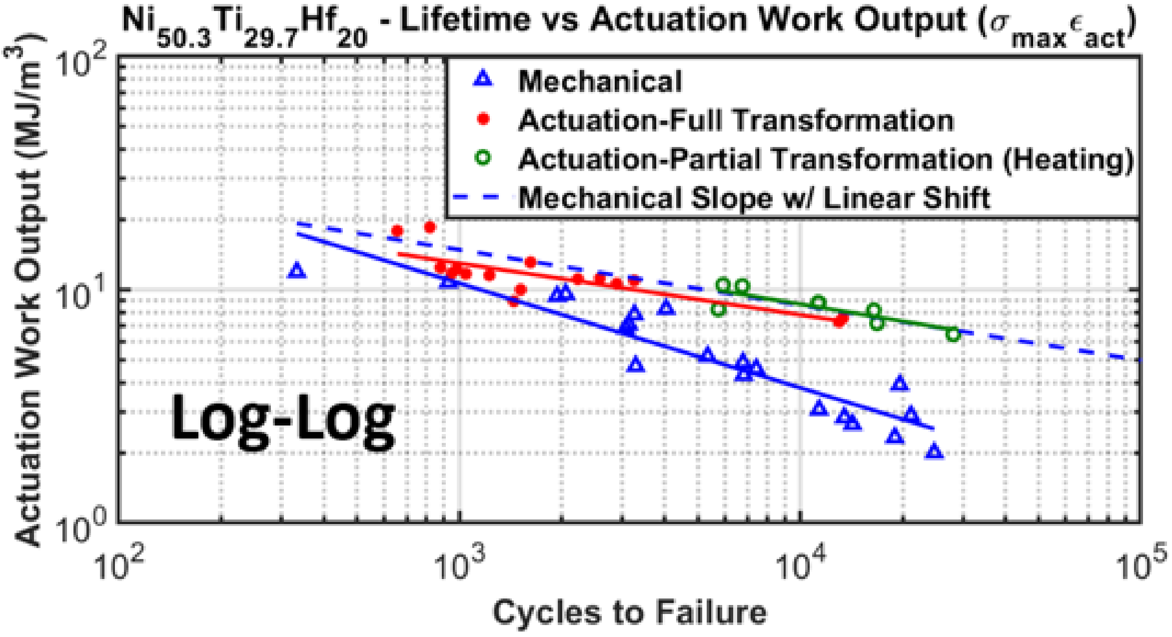

Figure 2.22: Work Output/Equivalent Curves for $Ni_{50.3}Ti_{29.7}Hf_{20}$-loglog

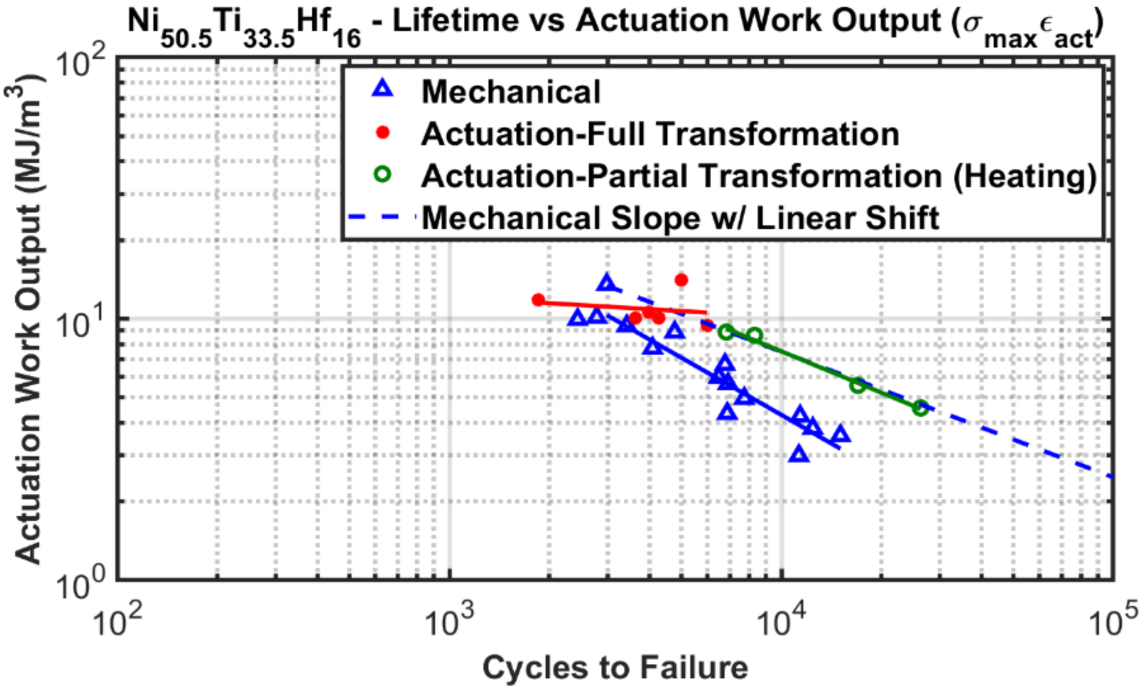

Figure 2.23: Work Output/Equivalent Curves for $Ni_{50.5}Ti_{33.5}Hf_{16}$

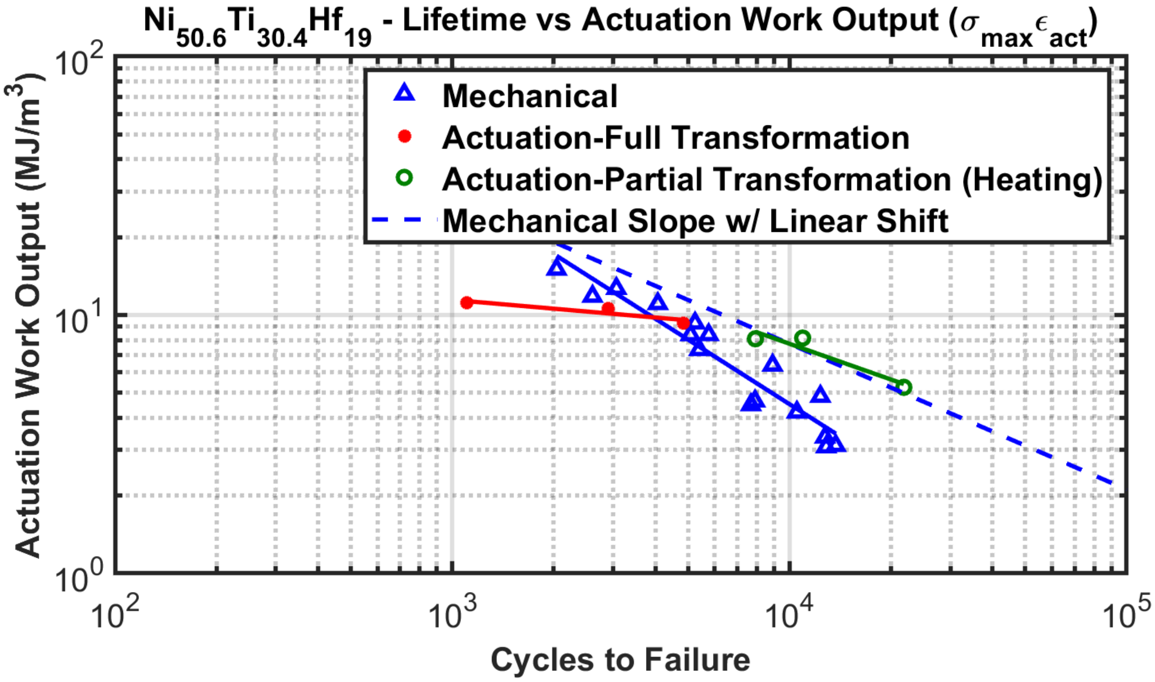

Figure 2.24: Work Output/Equivalent Curves for $Ni_{50.6}Ti_{30.4}Hf_{19}$

	$Ni_{50.3}Ti_{29.7}Hf_{20}$		$Ni_{50.5}Ti_{33.5}Hf_{16}$		$Ni_{50.6}Ti_{30.4}Hf_{19}$	
Coefficients	a	b	a	b	a	b
Partial Actuation	82.59501	-0.24466	941.52768	-0.52450	533.96641	-0.45970
Mechanical	235.46639	-0.44816	3443.4300	-0.7260	9726.84090	-0.83321

Table 2.6: Power Law Coefficients (Work Output = aN_f^b)

Shown above in Figures 2.21, 2.22, 2.23, and 2.24 are the actuation (full [red] and partial heating [green]) and mechanical fatigue results (blue). A semi-log and log-log graph for $Ni_{50.3}TiHf_{20}$ and a log-log for $Ni_{50.5}TiHf_{16}$, and $Ni_{50.6}TiHf_{19}$ each. When using the defined mechanical work equivalent, a similarity in the slopes between mechanical and partial heating actuation fatigue is observed, with the mechanical data being offset negatively along the y-axis shown in Figure 2.21. A linear projection/shift of the mechanical data onto the partial actuation data (dotted blue line) showcases the agreement in slope. The same data projected onto the log-log scale in Figure 2.22 shows the level of coincidence of the offset mechanical curve to the partial actuation curve. A similar trend is seen for the remaining materials in Figure 2.23 and Figure 2.24 showing repeatability between the compositions. Table 2.6 lists the values of the *a* and *b* coefficients as part of the work output equation.

The offset is dependent on material properties and loading conditions, as the quantitative value differ marginally for each composition. $Ni_{50.3}TiHf_{20}$ has an offset value of 4.6 MJ/m^3 with $Ni_{50.5}TiHf_{16}$, and $Ni_{50.6}TiHf_{19}$ having similar offset values of 3.15, 3.13 MJ/m^3 respectively.

Actuation strain is a function of set stress level and the temperature range it is cycled through. In mechanical cycling, the amount of strain is a function of applied stress and set temperature. In this case, to achieve the same level of strain as during thermal cycling, mechanical cycling requires much higher upper cycle stress levels due to the high stress values to reach yield stress for transformation compared to actuation operating stress levels. This is amplified with the set temperature the material is at (higher the temperature, higher σ_{Ms}, σ_{Mf} values). Additionally, frequency effects on the strain accumulation for $Ni_{50.3}TiHf_{20}$ shown in Figure 2.25 (courtesy of Behrouz Haghgouyan) shows a clear reduction in strain values for increasing frequency. Given the loading rate of 1 Hz, the change in recovered strain ($\Delta\epsilon$) is significant, increasing the divide between actuation and mechanical strain despite higher stresses for mechanical cycling. As per its definition, for mechanical work equivalent to be equal to actuation work output, a higher stress level has to be applied to attain a sufficient yet lower strains than actuation cycling. Accordingly, the offset in the fatigue trend lines can be understood as deriving from a combination of insufficiently low strain accumulation during mechanical cycling resulting in lower 'work equivalent' values and its operation at a higher upper cycle stress (UCS) range compared to actuation cycling, possibly factoring in the earlier failure of the material.

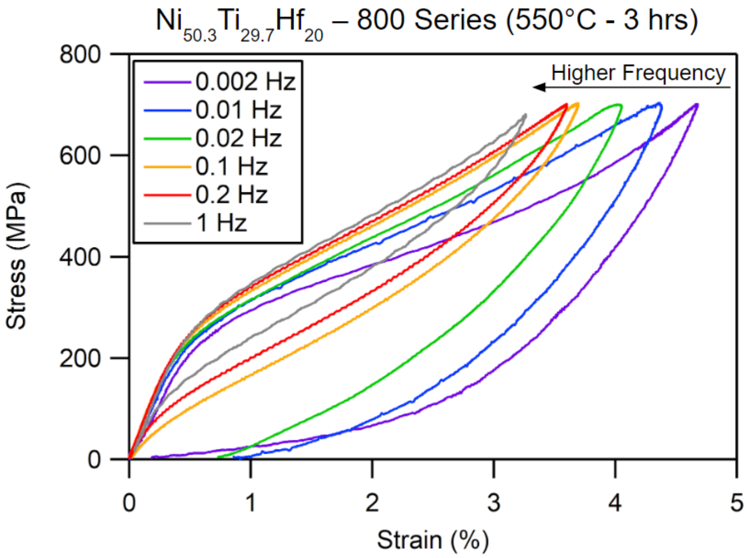

Figure 2.25: Frequency Effects on Stress-Strain Response

The full actuation fatigue data points (red) do not align well with either mechanical or partial actuation data. This is more pronounced for certain compositions. This is likely due to the fact that the upper cycle temperature of the tests were well above Austenite finish temperature of between 275 $^\circ C$ and 300 $^\circ C$. According to Karakoc et al. [56], it is shown that high upper cycle temperatures lead to higher and stable actuation strains but early failure of the material. It is likely that high UCT's can be a driving force for the reversal of stabilized martensite regions, resulting in higher actuation strains per cycle. Additionally, thermal energy contributes to increased likeness of dislocation motion and plasticity. Factoring in these reasons, potential correlation to mechanical data would be skewed or misrepresented.

To estimate actuation fatigue lifetime and loading conditions, one can conduct a series of mechanical tests to determine the slope, and a minimum of one actuation test to determine the offset and required shift, saving on run time and experiments. Additionally, one can then use this trend to predict loading conditions for practical application. An example of this process is given below in Table 2.7 and Figure 2.26 below.

No.	Procedure
1	Run isothermal mechanical fatigue tests at varying upper cycle stress levels, similar to the mechanical test matrix shown in this document for mechanical fatigue. Calculate and record $\sigma_{max}\Delta\epsilon$ and N_f on a log-log graph
2	Determine power law trend ($\sigma_{max}\Delta\epsilon = aN_f^b$), *a* and *b* parameters
3	To determine the offset, run quick low-cycle high work output actuation fatigue test(s). As an example, partial actuation tests at a load of 300 MPa with 100%-50% or 25% or 10% MVF transformation. Although one test would provide the necessary input, additional and/or repeat tests may increase accuracy
4	Project mechanical slope onto actuation data by adding a constant to power law correlation ($\sigma_{max}\Delta\epsilon = aN_f^b + const$)
5	Based on the design requirements, determine loading conditions that satisfy lifetime and work output requirements. In this example, a design requirement of 10000 cycles would observe 9 MJ/m^3 of work output. To satisfy the 2% strain requirement, the loading conditions can thus be 3% strain at 300 MPa or 2% strain at 450 MPa, given that these particular loading conditions and strain output at said loading conditions are applicable to the material being tested

Table 2.7: Predict Actuation Using Mechanical Fatigue - Process (1 to 5) - Tabular

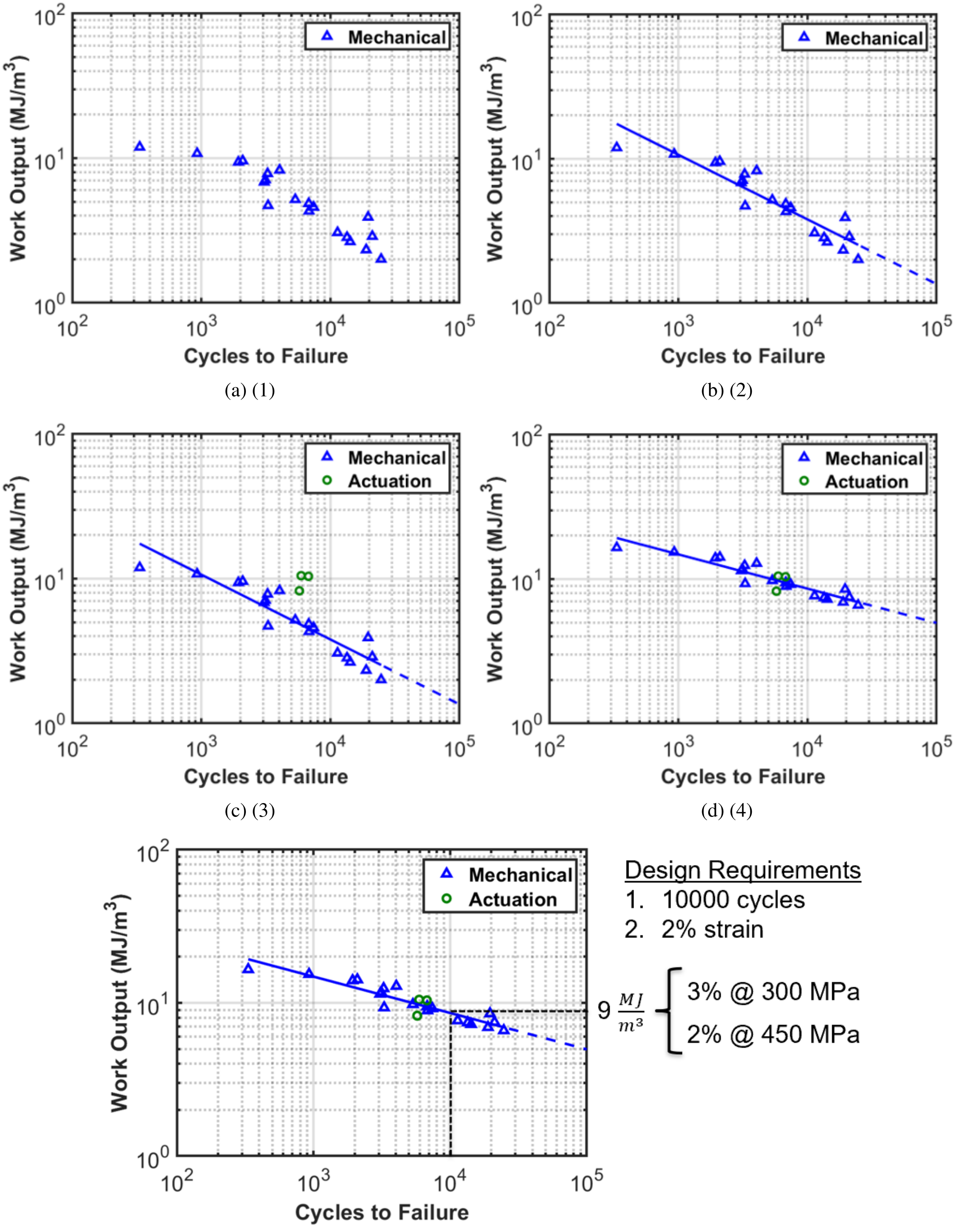

(a) (1)

(b) (2)

(c) (3)

(d) (4)

(e) (5)

Figure 2.26: Predict Actuation Using Mechanical Fatigue - Process (1 to 5)

3. FUNCTIONAL FATIGUE OF PSEUDOELASTIC NITIHF ALLOYS

3.1 Introduction

When studying fatigue of SMAs, it is important to consider the effect of microstructure on the cyclic stress-strain response. Earlier, hardness-vickers tests and peak-aging were mentioned as part of the pre-processing of the material before testing. Thermal processing such as heat treatments induce nano-precipitates within the matrix in Ni-rich NiTiHf materials that in turn reinforces the matrix. This process, also called precipitation hardening, allows the material to exhibit a stable stress-strain response. This is because for a pseudoelastic material to exhibit stable cycles, it is necessary to ensure that the stress levels required for transformation to Martensite are below that of the plastic yield stress of the material. Peak aging refers to the material having as high a hardness, in other words as high as yield stress, to ensure minimum dislocation motion and nucleation resulting in plasticity and the accumulation of plastic strains in the material. From the discussion on fatigue in the introduction section, we find that despite the heat treatments, plastic strains arise from dislocation motion that lead to an increase in dislocation density and pile ups, which promote regions of high internal stresses.

Although the lifetime of a material, alluding to the material's structural fatigue properties, is important, the functional fatigue properties which describe the evolution of shape memory and pseudoelastic properties such as transformation strains of the material are important to characterize for proper material selection and implementation for use in actuator systems. The inevitable changes in microstructure from cyclic deformation leads to the functional degradation of the material. Here, it is important to distinguish between high and low cycle fatigue. Functional fatigue is applicable to low cycle fatigue, which refers to samples that undergo some degree of reversible phase transformation and accumulation of plastic strains. High cycle on the other hand refers to samples that are cycled below the σ_{Ms} values of the material, in the predominately elastic regime, resulting in no phase transformation and plastic strains. As such, functional fatigue of SMA's is ultimately tied to the phase transformation properties of the material. The changes in microstructure are influenced by loading conditions, functional fatigue trends are heavily influenced by intrinsic material properties such as ductility. As a result, pseudoelastic or mechanical cycling of these alloys can be conducted in actuation cycling's stead to characterize the material's functional trends via the accumulation of plastic strains, allowing for a preliminary material screening before extensive actuation fatigue analyses. This work aims to characterize the functional fatigue trends of the same three precipitation hardened NiTiHf alloys using data accumulated from the structural fatigue study to compare plastic strains accumulation trends, and how it influences the pseudoelastic properties, and as such the stress-strain of the material. Further developing a phenomenological description of the relationship between the changes that are observed in the macroscopic stress-strain response to the evolution of plastic strains.

While total and plastic strain evolution can be seen on a macroscopic scale, it does not tell us about the origins of localized plastic and transformation strain accumulation. To study this closely, digital image correlation (DIC) images have been taken over the course of the fatigue life of the material for certain experiments on $Ni_{50.3}Ti_{29.7}Hf_{20}$ samples at various upper cycle stress levels to showcase localized strain evolution. Functional fatigue affects both the shape memory and pseudoelastic properties of the SMA. Over the course of a lifetime during mechanical fatigue, the stress-strain curves show drastic changes from what is initially a stable hysteresis response resulting from changes in various parameters (such as transformation stresses among others) due to the inevitable functional degradation of the material (see Figure 3.8). Consequently, in this section, along with evolution of plastic strains, evolution of other parameters such as recovered strain ($\Delta\epsilon$), Martensite Start Stress (σ_{Ms}), hardening slope (s_{load}), energy dissipation (E_{diss}), strain energy (E_{diss}), and hysteresis width (H_{width}) will be showcased to provide a broader picture on how the stress-strain response evolves as cycling continues. This is done in order to find the phenomenological link of these parameters to plastic strain accumulation, and to each other. Many studies have shed light into the functional fatigue response of SMAs. Gao et al. [73] studied the physical origin of functional fatigue in SMAs from a crystallographic and defect generation point of view via both theoretical and experimental means. Abuzaid et al. [74] studied the heterogeneity of phase transformation during thermal cycling and changes in transformation strain as it relates with increasing plastic strains and TRIP in $Ni_{50.3}Ti_{25}Hf_{24.7}$ using DIC. Dornelas et al. [75] developed a 3D constitutive model for SMA functional fatigue using continuum damage mechanics (CDM). Sidharth et al. [76] showed the frequency effects of the functional properties on single crystal NiTi along with using Transmission Electron Microscopy (TEM) to analyze sources of dislocation generation and motion. Following, macroscopic measurements from the stress-strain response are compared and discussed, with DIC results visualizing the evolution of localized strain.

For reference in the following sections, Figure 3.1 shows the definitions of the calculated strains among other pseudoelastic metrics that will be used. Refer to **Appendix A** for more details.

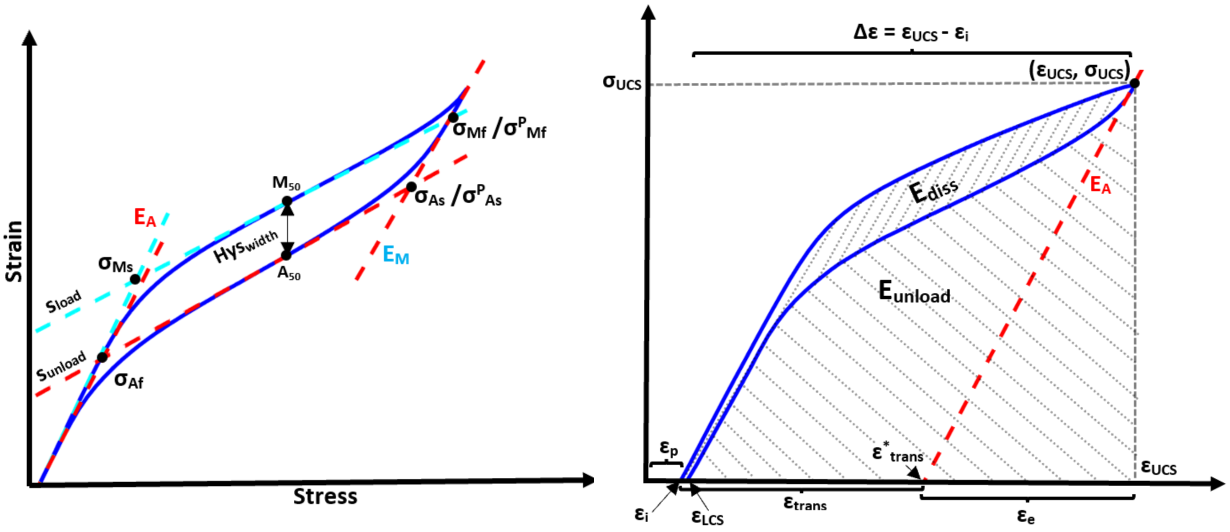

Figure 3.1: Pseudoelastic Metrics Definitions

3.2 Macroscopic and Mesoscopic Strains (DIC) Evolution

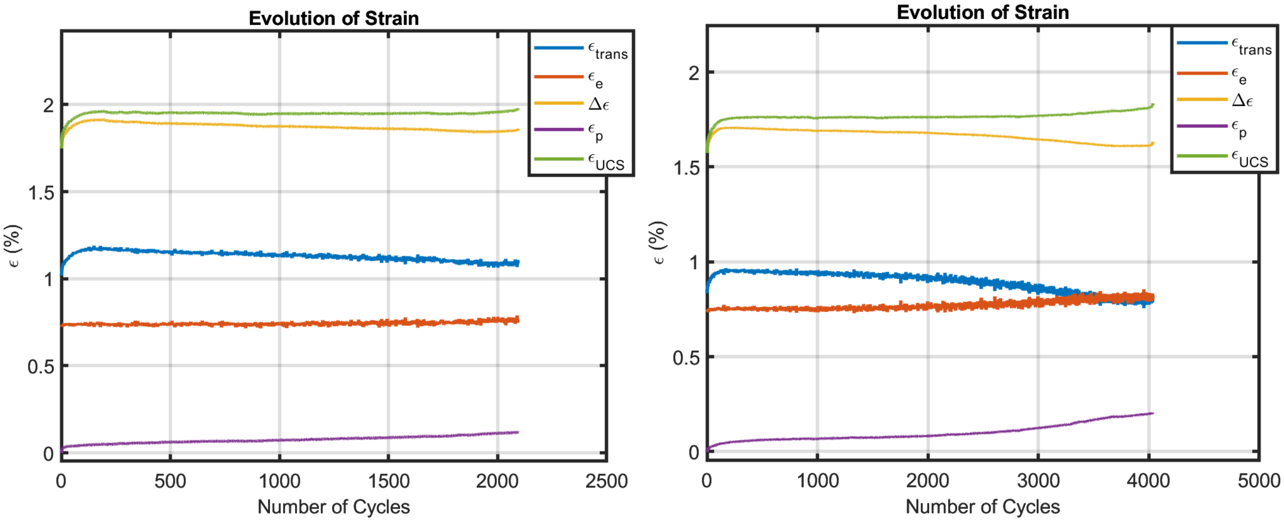

(a) 550 MPa UCS

(b) 525 MPa UCS

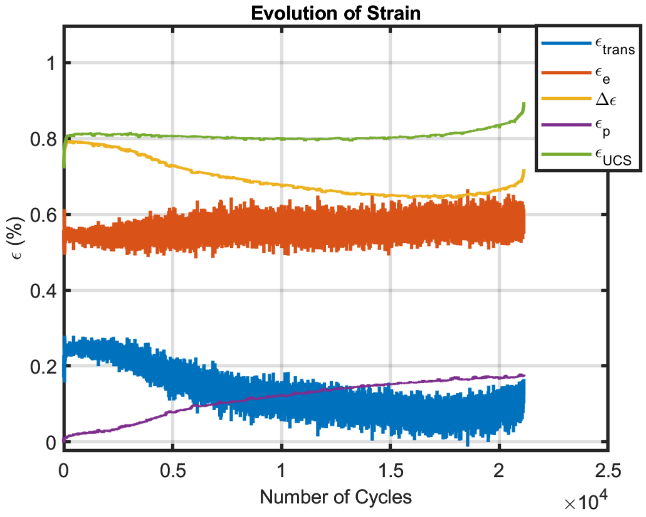

(c) 400 MPa UCS

Figure 3.2: Strain Evolution

Here, the macroscopic strain values of certain $Ni_{50.3}Ti_{29.7}Hf_{20}$ samples at different UCS's are showcased. The plastic (ϵ_p), elastic (ϵ_e), transformation (ϵ_{trans}), recovered $(\Delta\epsilon)$, and upper cycle strains (ϵ_{UCS}) are shown. Note that the cumulative plastic strain (ϵ_p) + the elastic strain (ϵ_e) + transformation strain (ϵ_{trans}) equals that of the strain at UCS (ϵ_{UCS}) (see Figure 3.2). In all cases, similar trends are observed. A marked increase in ϵ_{trans}, $\Delta\epsilon$, and ϵ_{UCS} followed by a stabilization period, followed by a steady increase in plastic strains and decrease in transformation strains, with constant elastic and upper cycle strain values. Although small, there is also a slight but marked increase in ϵ_p values during initial cycling. ϵ_{UCS} for most of the fatigue life remains constant after stabilization. Visually, it is observed that the trends for the transformation strain and recovered strain share similarity within each figure, which in turn is influenced by the increase in plastic strains, wherein the decrease in transformation strain is offset by the increase in plastic strain. This implies that the reduction in transformation strain arises from the increase in plastic strains, which balance each other out, keeping the total strain ϵ_{UCS} constant. Given the macroscopic responses, these observations are then compared to DIC data to study the origins and evolution of these different strains from a localized perspective.

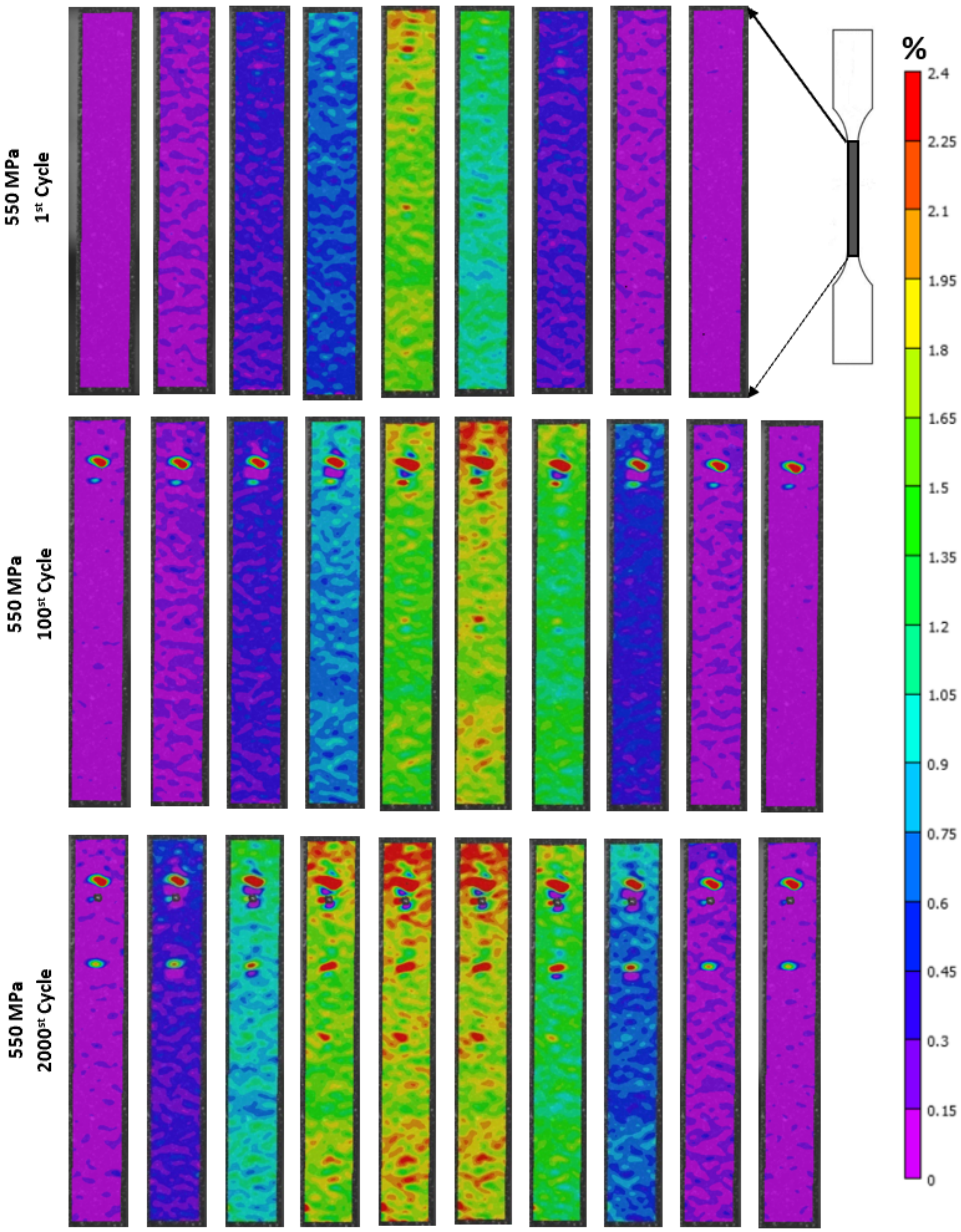

Figure 3.3: DIC Results on $Ni_{50.3}Ti_{29.7}Hf_{20}$ at 550 MPa UCS - 1^{st} cycle (top), 100^{th} cycle (middle), 2000^{th} cycle (bottom)

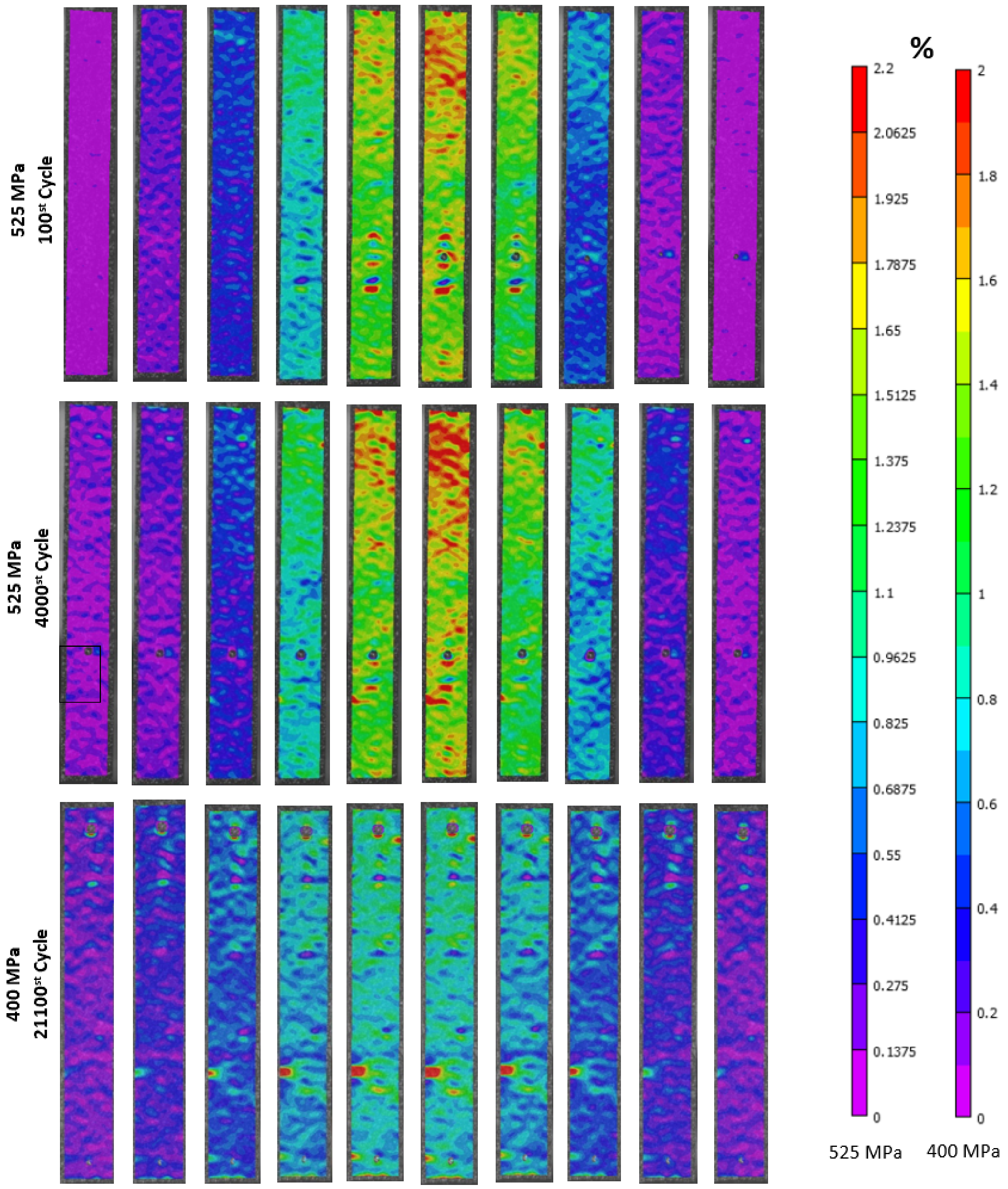

Figure 3.4: DIC Results on $Ni_{50.3}Ti_{29.7}Hf_{20}$ - 100th cycle 525 MPa UCS (top), 4000th cycle 525 MPa UCS (middle), 21100th cycle 400 MPa UCS (bottom)

DIC images for certain experiments on the $Ni_{50.3}Ti_{29.7}Hf_{20}$ samples were taken to observe total and plastic strain nucleation and evolution. The figures above showcase post-processed DIC images. Each color contour image corresponds to the sample gauge section surface that has the speckle patterns. Each row of contour images corresponds to 1 cycle, where either ends correspond to a sample at the lower cycle stress (5 newtons), and the middle the peak stress level. In Figure 3.3, the plots correspond to a $Ni_{50.3}Ti_{29.7}Hf_{20}$ sample cycled at a UCS of 550 MPa with a fatigue life of 2049 cycles. The first row corresponds to the first cycle in the test. The second row showcases the 100^{th} cycle and the third and last row the 2000^{th} cycle, which are the last set of DIC images taken before sample failure. During the first cycle for the 550 MPa UCS images, strain accumulation is seen throughout the gauge section, with localized regions of high transformation strain regions (red) near the top of the gauge section. Small speckle regions of blue at the lower cycle stress indicate accumulation of some plastic strain upon unloading. The second row, which indicates the 100^{th} cycle, confirms similar observations, this time with a higher degree of strain values as seen with the clear difference in growing high strain regions (red) during peak stress. This is confirmed by the increase in ϵ_{UCS} during initial cycling as seen in Figure 3.2a. It is also observed, that these new regions of high strain grow out from initially nucleated sites, with new nucleation sites being scarce. Additionally, at zero stress, non-zero strain values along the gauge section are more apparent, indicating an accumulation of more plastic or irrecoverable strain. Again, these new regions of plastic strains accumulate at or around the regions associated with high strains. An evident but important observation is the heterogeneity in the strain values throughout the gauge length, with the macroscopic strain value encapsulating the average of all local strain values.

Near the end of life of the material shown in row three (2000^{th} cycle), even higher values of total strain are observed. This is due to the slight difference in ϵ_{UCS} values between the 100^{th} and 2000^{th} cycle as seen in Figure 3.2a. Again, regions of new high strain grow from initial high strain regions corresponding to the initial nucleation sites. Similar trends are seen with plastic strains at minimum stress, where most of it is concentrated at or near high strain regions associated with transformation. Additionally, at this point in the life, as seen in Figure 3.2a, transformation strain decreases while plastic strain increases. This implies that a large portion of the intensity of the strain contours comes from additional plastic strains. This is confirmed by the contour plots at zero stress at which plastic deformation regions become even more apparent at higher cycle number. This goes in hand with macroscopic observation of continuous increase in plastic strain values throughout the samples' lifetime. Since the plots show additional plastic strains accumulate at regions of initially higher transformations, this is indicative of the fact that a large portion of plastic strains arise in the form of transformation induced plasticity (TRIP) via stable Martensite regions.

In Figure 3.4, similar results are shown for 525 MPa UCS 100^{th} (top row) and 4000^{th} cycle (middle row). This helps contrast similar stress levels with different fatigue lives. The 100^{th} cycle again shows regions of transformation strains at peak stress near the top of the gauge length, with minute regions of irrecoverable plastic strain. The 4000^{th} cycle however shows a move evolved contour region with heavier regions of red during peak stress indicative of increased upper cycle strain and apparent regions of plastic strain accumulation with dense blue regions at zero stress compared to the 550 MPa sample. As stated previously, this helps confirm the macroscopic observation that a sample with higher fatigue lives operating at near similar UCS's accumulate more plastic strain as the material cumulatively accumulates plastic strain over a larger time period. Adding on to that, the last and final row showcases the 21100^{th} cycle of the 400 MPa test. At peak stress, upper cycle strain values range lower due to the lower applied UCS. However, at zero stress, a much denser region of plastic strain is observed compared to the 550 MPa or 525 MPa near the end of life. Although the applied UCS is lower, due to the fatigue life extending well beyond the 550 and 525 MPa UCS fatigue lives, a higher concentration of plastic strain regions is observed. **Note**: Each UCS shown here has a slightly different scale shown to the right of the graphs.

Given the trend that is seen with transformation and plastic strains at a macroscopic scale, along with the observations made in DIC that plastic strains accumulate at regions of transformation, it would imply that the plastic strain consists of predominately transformation induced plasticity (TRIP) from stable martensite variants.

Earlier, it is observed that the plastic, transformation, and upper cycle strain all show a drastic increase within the first couple of cycles corresponding to the materials training phase, before stabilizing. This observation is confirmed by the above DIC analysis, which also shows a major increase in strain intensity during the first hundred cycles. According to Phillips et al. [38], this increase in transformation strain during the first cycles is the result from changes in defect density from dislocation movement, which may happen via movement of habit planes. This change in defect intensity induces increased local stresses which promotes more transformation strains, but also as a result, more plastic strains. This is discussed further in the following sections. It is important to note that plastic strains may consist of both plastic deformation from local plastic flow along with TRIP from stabilized martensitic regions, which is indistinguishable in DIC.

3.3 Plastic Strain Evolution during Mechanical Fatigue

The evolution of plastic strain (ϵ_p) of all three materials at a range of upper cycle stress levels is picked and showcased in Figure 3.5. All materials show a different trend for the accumulation of plastic strains both before and after reaching shakedown. $Ni_{50.3}Ti_{29.7}Hf_{20}$ materials show a brief period of stabilization before increasing at a steep rate for high stress levels, with lower stresses showing a similar increase in rate and eventual saturation. For $Ni_{50.6}Ti_{30.4}Hf_{19}$, the largest accumulation of plastic strains occur after reaching shakedown. Upon reaching shakedown, a steep linear increase in plastic strains takes place, especially for high stress levels, showing little sign of saturation. Interestingly, for $Ni_{50.5}Ti_{33.5}Hf_{16}$, the largest accumulation of plastic strains occur before reaching shakedown. The stabilization and saturation is more apparent, showing a clear transition to a plateau. It can be inferred, from the total and rate of plastic strain accumulation that $Ni_{50.5}Ti_{33.5}Hf_{16}$ showcases highest ductility, followed by $Ni_{50.6}Ti_{30.4}Hf_{19}$ and $Ni_{50.3}Ti_{29.7}Hf_{20}$. It is then observed, that compositions with higher percentages of Hafnium, observe reduced ductility. These trends seen with plastic strains and ductility play an important role with the material's functional evolution, as will be shown in the following sections.

It is important to note that the accumulation of total plastic strains depends not only on stress, but number of cycles. With $Ni_{50.3}Ti_{29.7}Hf_{20}$, this effect is seen clearly, whereby lower stress specimens accumulate lower amount of plastic strains during training (before shakedown) but over the lifetime of the sample accumulates more plastic strains than the high stress level specimens for low cycle fatigue. Seen similarly with $Ni_{50.6}Ti_{30.4}Hf_{19}$ samples, with the 650 MPa and 600 MPa curve, and the 500 MPa and 450 MPa curve, showing similar total plastic strain given the longer life of the latter. With $Ni_{50.5}Ti_{33.5}Hf_{16}$, a similar phenomenon for 625 MPa and 550 MPa is realized.

Consequently, using total cumulative plastic strains as parameter for fatigue model and prediction could yield misrepresented results. As such, Figure 3.6 shows plastic strain based fatigue life modelling, using plastic strain accumulation at the 300^{th} cycle. By this stage, the NiTiHf SMAs showcase stabilized or near stabilized responses, corresponding to reaching shakedown. Table 3.1 lists the *a* and *b* coefficients and r-squared values. It is apparent that the $Ni_{50.3}Ti_{29.7}Hf_{20}$ samples show the least correlated data points, followed by $Ni_{50.6}Ti_{30.4}Hf_{19}$ and $Ni_{50.5}Ti_{33.5}Hf_{16}$ showing the best fit. Interestingly, this trend is in line with the trend seen with ductility, whereby the more ductile materials show a better fit. Regardless, with this model, it can be inferred in general, that at or around shakedown, the cumulative plastic strain falls for higher fatigue lives.

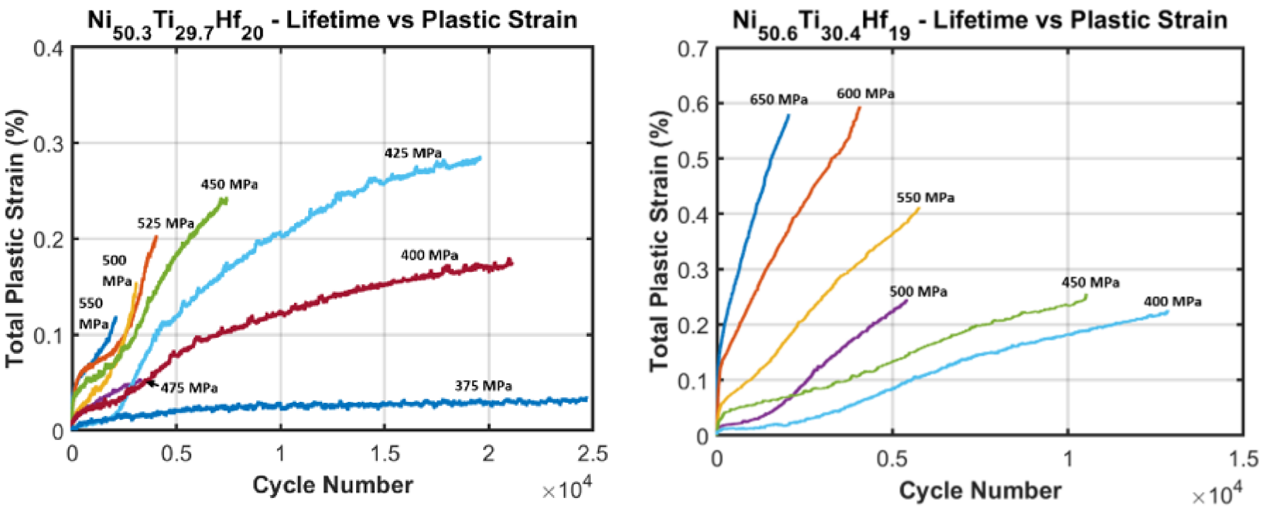

(a) $Ni_{50.3}Ti_{29.7}Hf_{20}$ (b) $Ni_{50.6}Ti_{30.4}Hf_{19}$

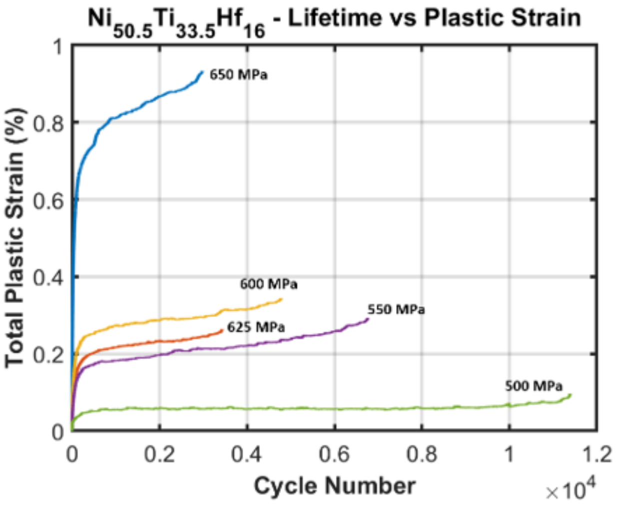

(c) $Ni_{50.5}Ti_{33.5}Hf_{16}$

Figure 3.5: Plastic Strain Evolution as a Function of Cycle Number at Various UCS's

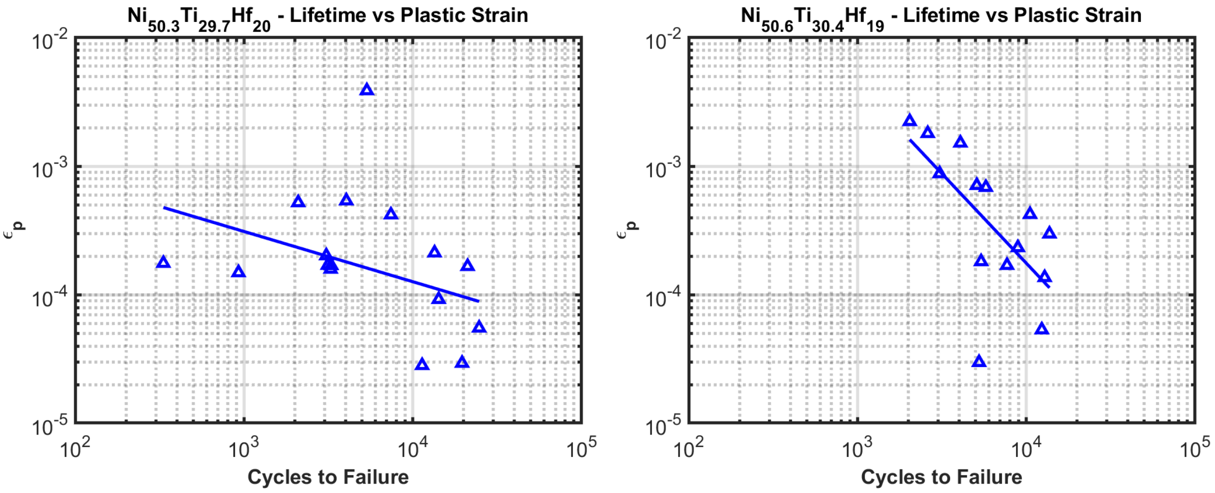

(a) $Ni_{50.3}Ti_{29.7}Hf_{20}$ (b) $Ni_{50.6}Ti_{30.4}Hf_{19}$

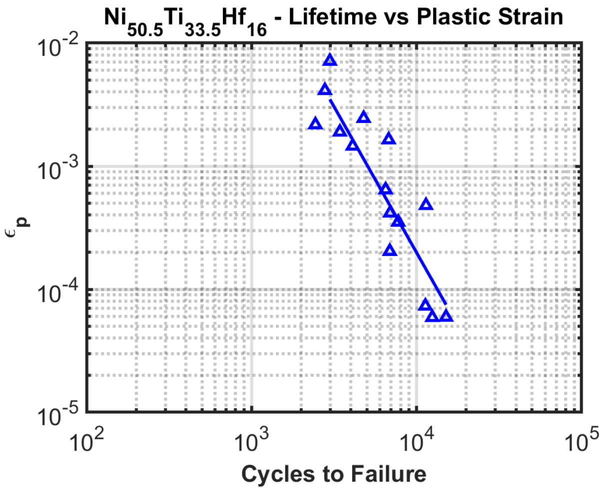

(c) $Ni_{50.5}Ti_{33.5}Hf_{16}$

Figure 3.6: Life vs Plastic Strain ($\epsilon_p = aN_f^b$)

	$Ni_{50.3}Ti_{29.7}Hf_{20}$			$Ni_{50.6}Ti_{30.4}Hf_{19}$			$Ni_{50.5}Ti_{33.5}Hf_{16}$		
Coefficients	a	b	R^2	a	b	R^2	a	b	R^2
Plastic Strain	0.003996	-0.357	0.101	65.3	-1.39	0.432	604266.249	-2.371	0.83

Table 3.1: Plastic Strain based Lifetime Model Parameters

For completeness, Figure 3.7 shows plastic strain based functional fatigue modelling, which compares work equivalent parameter ($\sigma_{max}\Delta\epsilon$) at the first cycle to cumulative plastic strain at stabilization (300^{th} cycle). Table 3.2 lists the *a* and *b* coefficients and r-squared values. Since work output is also correlated with fatigue lifetime, as showcased during lifetime modelling in the previous chapter, it shows the potential to bridge predictive modelling gaps between functional and structural fatigue.

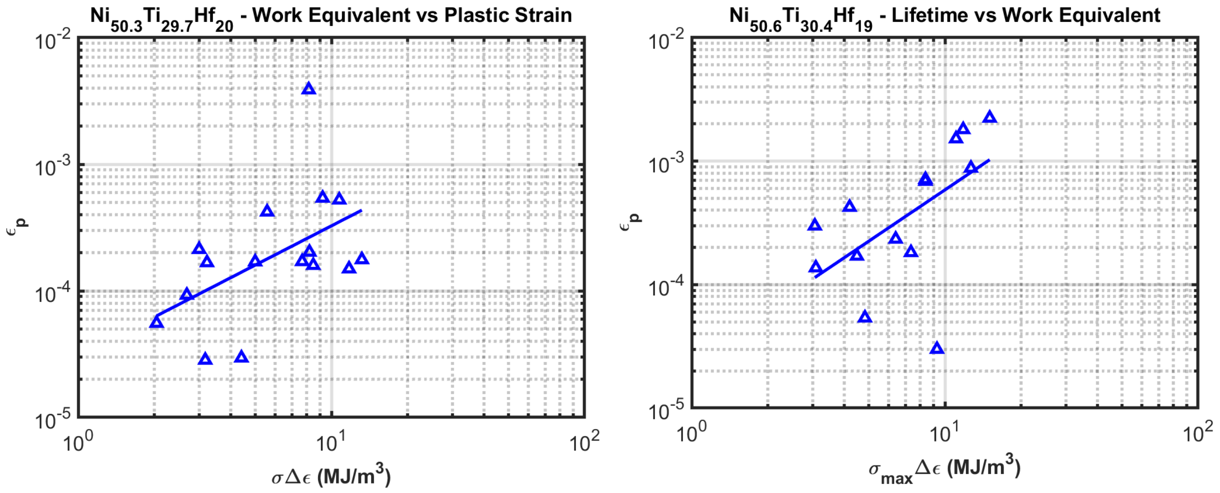

(a) $Ni_{50.3}Ti_{29.7}Hf_{20}$ (b) $Ni_{50.5}Ti_{33.5}Hf_{16}$

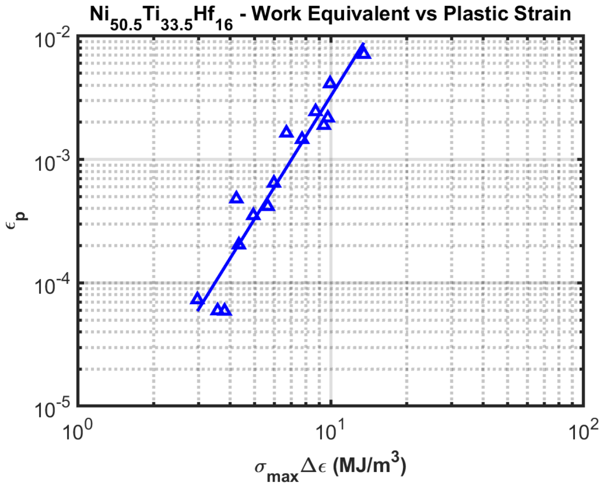

(c) $Ni_{50.6}Ti_{30.4}Hf_{19}$

Figure 3.7: $\sigma_{max}\Delta\epsilon$ vs Plastic Strain ($\epsilon_p = a(\sigma_{max}\Delta\epsilon)^b$)

	$Ni_{50.3}Ti_{29.7}Hf_{20}$			$Ni_{50.6}Ti_{30.4}Hf_{19}$			$Ni_{50.5}Ti_{33.5}Hf_{16}$		
Coefficients	a	b	R^2	a	b	R^2	a	b	R^2
Plastic Strain	3E-5	1.03	0.259	2.4E-5	1.381	0.31	2E-6	3.3074	0.92

Table 3.2: Plastic Strain based Functional Fatigue Model Parameters

3.4 Effects of Cyclic Deformation on Pseudoelasticity of NiTiHf Alloys

Apart from strain values, other aspects of the stress-strain response show drastic changes throughout a samples' lifetime, as shown in the figures as part of Figure 3.8. As cycling continues, the onset of more plastic strains associated with TRIP induce shape changes in the stress-strain response. In Figure 3.8, this is seen clearly for cycles above 10^4, where the stress-strain response shows a large deviation from the typical idealized pseudoelastic stress-strain curve. As such, this section goes over the evolution of certain pseudoelastic metrics such as recovered strain, transformation stresses, hardening slope, hysteresis, strain energy, and hysteresis width to study functional properties, its degradation, and the factors that influence it. All of these parameters are calculated using the same definitions as in Figure A.1. A robust MATLAB routine is implemented for the calculation of all metrics for full/partial pseudoelastic transformations, including drastically fatigued stress-strain curves and curves near the elastic response, which makes distinguishing stress-induced transformation difficult. An example of the Tangent Line Method is shown in Figure 3.9 for certain stress-strain curves of the 550 MPa (top row) and 425 MPa (bottom row). The 1^{st}, 100^{st} and final cycles (left to right), exhibiting various hysteresis shapes, are shown. The black lines indicate the tangent line and the black circles indicate intersection points which correspond to the transformation stresses/strains. The linear regions within these curves are well captured, even for responses showcasing higher degree of non-linearity. Refer to **Appendix A** for a detailed walk through on the implementation of the routine for the extraction of pseudoelastic metrics.

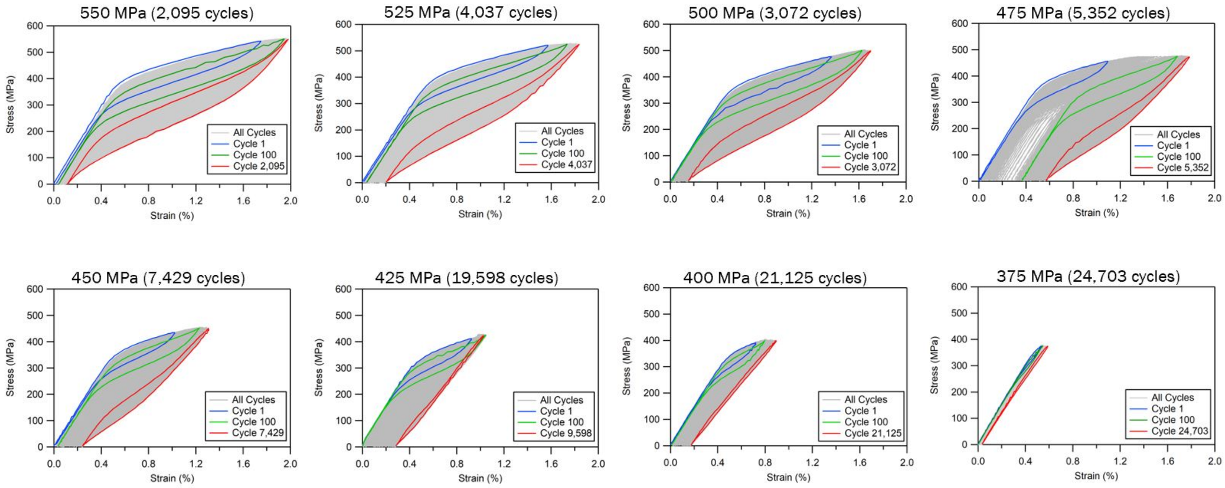

Figure 3.8: $\sigma - \epsilon$ curves (1st, 100th, and final) of Mechanical Fatigue tests for $Ni_{50.3}Ti_{29.7}Hf_{20}$

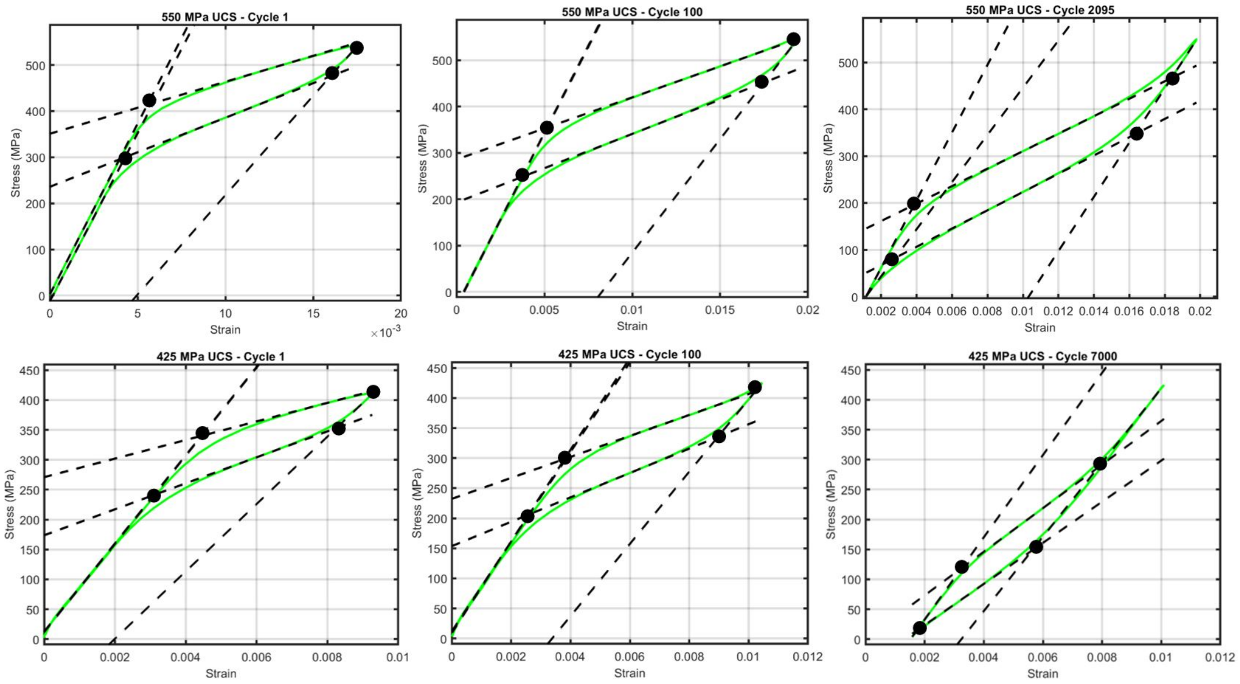

Figure 3.9: Tangent Line Method on $Ni_{50.3}Ti_{29.7}Hf_{20}$ at Different Cycles- 550 MPa UCS (top row) and 425 MPa UCS (bottom row)

Details below showcase results of the aforementioned pseudoelastic metric trends for all three materials at varying stress levels.

3.4.1 Strain, Transformation Stress, and Hardening Slope

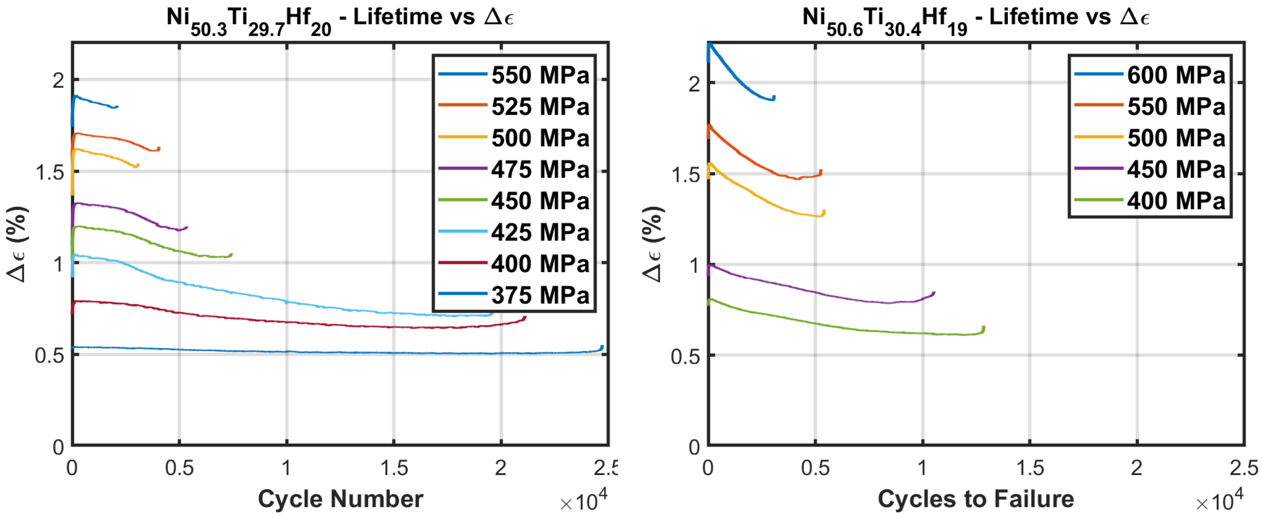

(a) $Ni_{50.3}Ti_{29.7}Hf_{20}$ (b) $Ni_{50.6}Ti_{30.6}Hf_{19}$

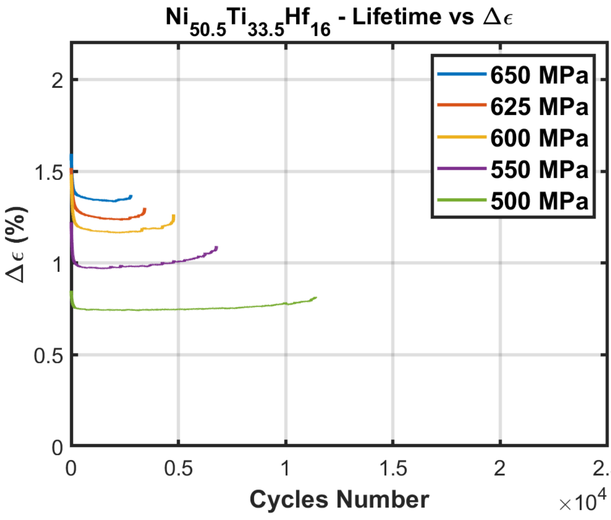

(c) $Ni_{50.5}Ti_{33.5}Hf_{16}$

Figure 3.10: Evolution of Recovered Strain ($\Delta\epsilon$)

Recovered Strain ($\Delta\epsilon$) - Figure 3.10 showcases the evolution of recovered strains as a function of cycles for a range of stress levels for the three materials. Initial strain magnitudes go up for increasing stress levels, but decrease as cycles go on. A strong contrast between the trends seen with plastic strains, and the corresponding strains are observed, with more ductile materials observing a larger rate of decrease during initial cycling. For $Ni_{50.3}Ti_{29.7}Hf_{20}$, an initial marked increase is observed, as also seen in DIC. This is however not the case for $Ni_{50.6}Ti_{30.4}Hf_{19}$ and $Ni_{50.5}Ti_{33.5}Hf_{16}$ which show a smaller increase and marked decrease respectively. To allow further understanding as to the differences between initial values for each material, the Martensite stress (σ_{Ms}) and hardening slopes (s_{load}) are analyzed.

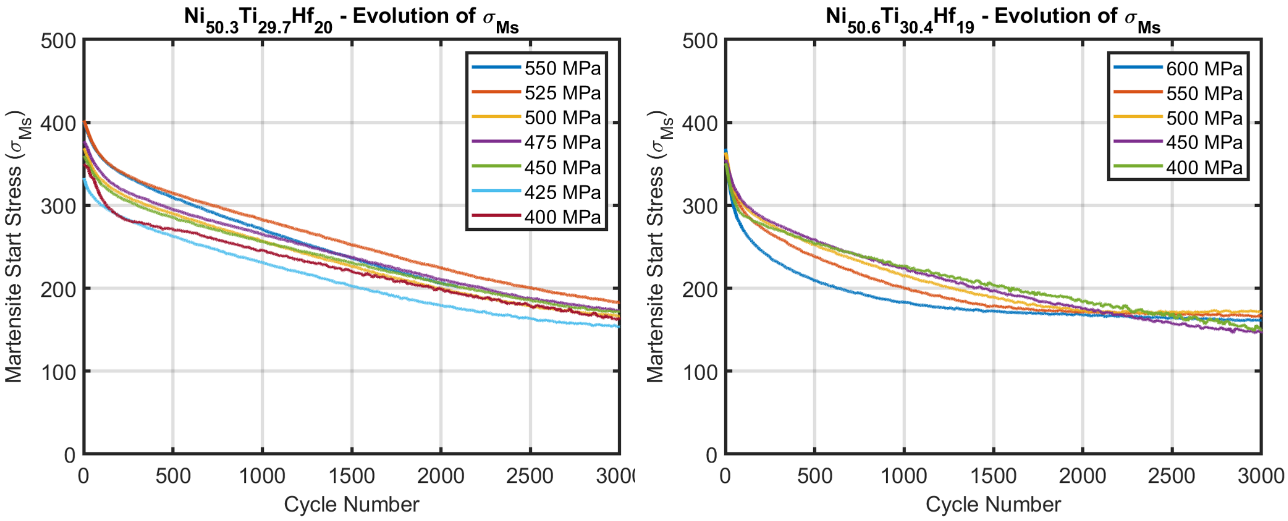

(a) $Ni_{50.3}Ti_{29.7}Hf_{20}$ (b) $Ni_{50.6}Ti_{30.6}Hf_{19}$

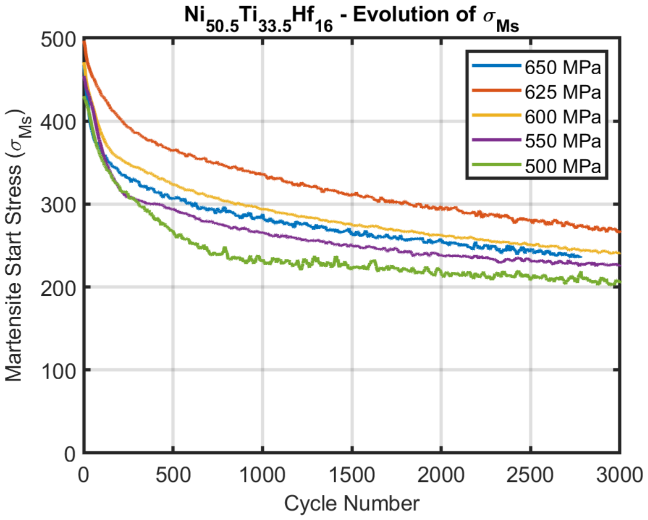

(c) $Ni_{50.5}Ti_{33.5}Hf_{16}$

Figure 3.11: Evolution of Martensite Start Stress (σ_{Ms})

Transformation Stresses - Martensite Start Stress (σ_{Ms}) - In Figure 3.11, the Martensite start stress (σ_{Ms}) show a marked decline during initial cycling. As cycling continues, the stresses start to plateau but still gradually decrease. This occurs until failure, or long enough for the stress levels to saturate. During initial cycling, phase transformation promotes the creation and movement of dislocations. Upon transformation reversal, these dislocations remain and promote the accumulation of stabilized Martensitic regions and with it residual internal stresses [77]. With additional cycles, these internal stresses assist the transformation to martensite, effectively lowering the yield stress for transformation. For this reason, transformation to Austenite during unloading also reduces, as it becomes more difficult to transform back. Figure 3.11b shows a distinct pattern whereby a higher stress level leads to a higher rate of decrease, after which the curves saturate towards a similar value. Similar patterns in $Ni_{50.3}Ti_{29.7}Hf_{20}$ (see Figure 3.11a) and $Ni_{50.5}Ti_{33.5}Hf_{16}$ (see Figure 3.11c) are less evident and show uncertainty, yet retain some degree of similarity for certain stress levels. As cycling continues, movement of dislocations decreases while most pile up, and so does the rate of decrease of the transformation stresses when internal stresses within the material tends to saturate. The lower yield stress allows for more transformation. This puts into perspective as to why an increase in recovered strains is seen. However, it still does not explain the trends seen with the more ductile materials.

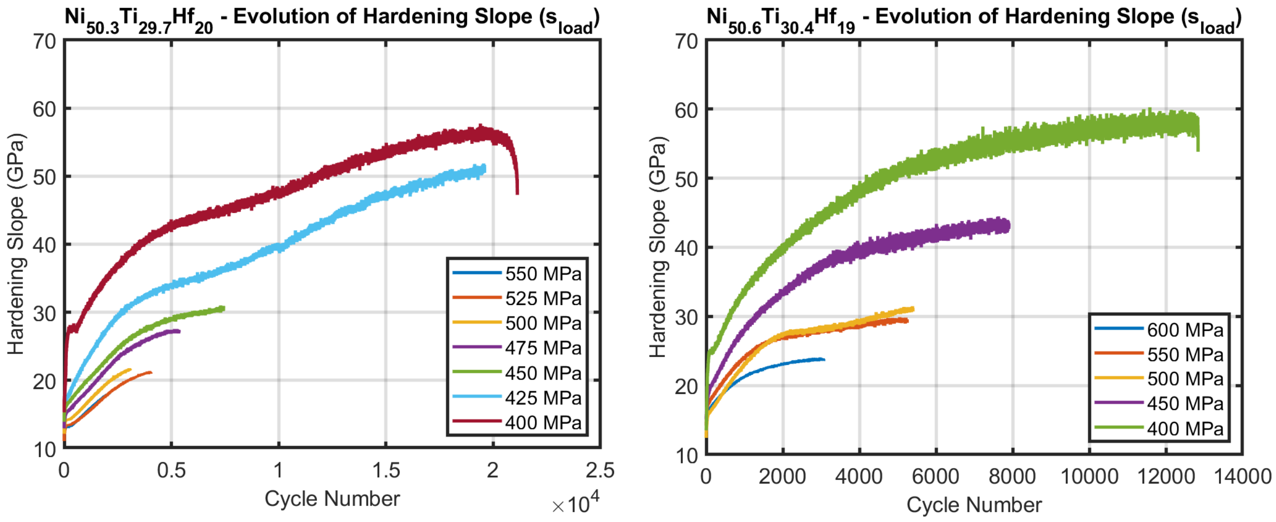

(a) $Ni_{50.3}Ti_{29.7}Hf_{20}$ (b) $Ni_{50.6}Ti_{30.6}Hf_{19}$

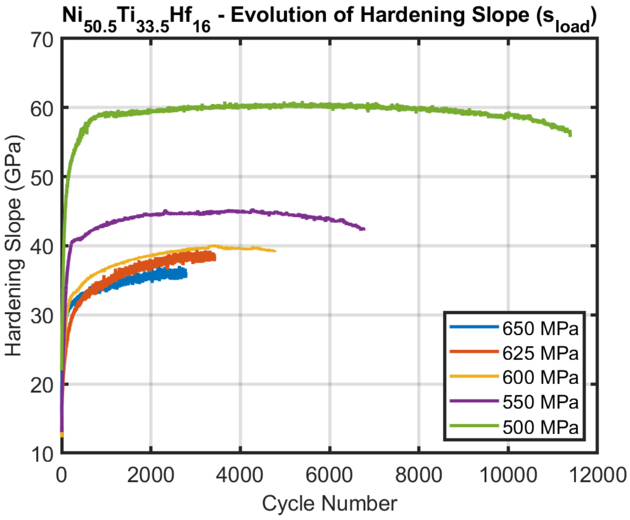

(c) $Ni_{50.5}Ti_{33.5}Hf_{16}$

Figure 3.12: Evolution of Hardening Slope (s_{load})

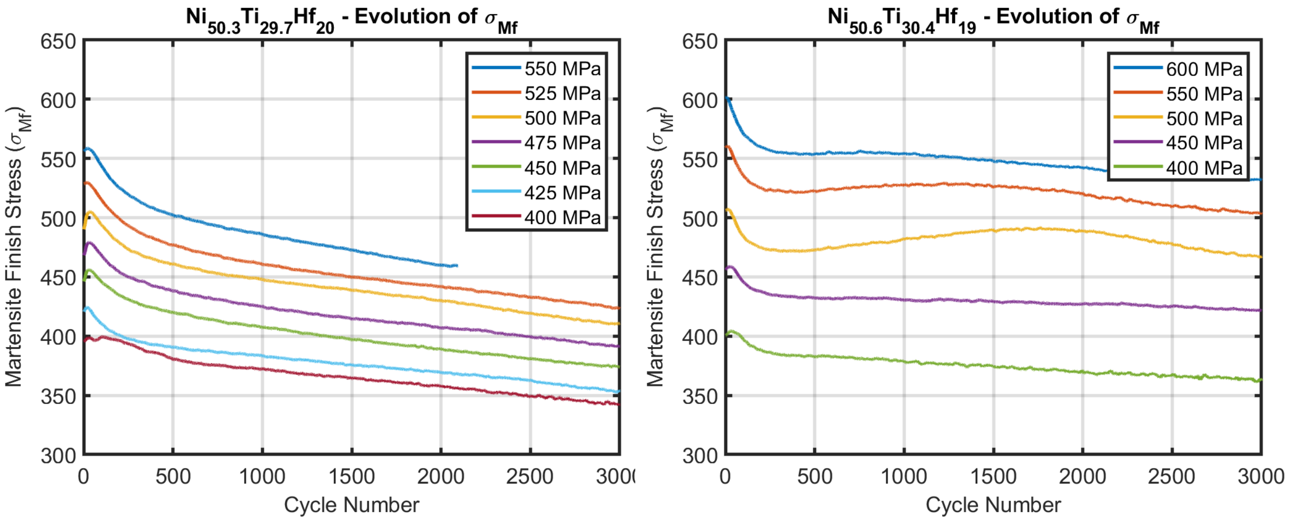

(a) $Ni_{50.3}Ti_{29.7}Hf_{20}$ (b) $Ni_{50.6}Ti_{30.6}Hf_{19}$

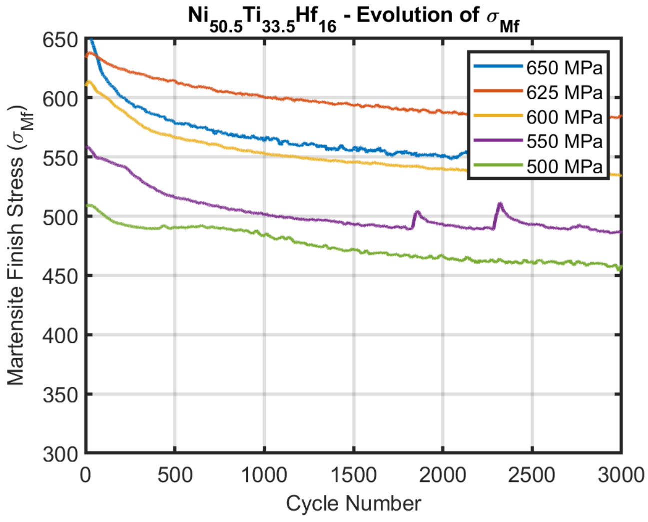

(c) $Ni_{50.5}Ti_{33.5}Hf_{16}$

Figure 3.13: Evolution of Martensite Finish Stress (σ_{Mf})

Hardening Slopes - Figure 3.12 showcases the hardening slope (s_{load}) of the loading curve as a function of cycle number. For $Ni_{50.3}Ti_{29.7}Hf_{20}$ (see Figure 3.12a) and $Ni_{50.4}Ti_{30.6}Hf_{19}$ (see Figure 3.12b), trends show a marked increase during initial cycling, with subsequent gradual increase towards asymptomatic behavior with increasing cycles. The same behavior is more drastic for $Ni_{50.5}Ti_{33.5}Hf_{16}$ (see Figure 3.12c) whereby there is a sharp increase in magnitude during initial cycling, followed by quick saturation. More interestingly, all materials observe a higher rate of increase for decreasing stress levels, especially during initial cycling. According to Zhang et al. [77], this increase in slope can be explained by the phenomenon that leads to the reduction in transformation stresses. As discussed earlier, due to local internal stresses from an increase in dislocation density, all values of the transformation stresses decrease. However, due to an internal stress gradient as phase transformation continues, the Martensite finish and Austenite start stresses decrease at a significantly lower rate than the Martensite start and Austenite finish stresses. As a result, a larger stress has to be applied to continue the forward transformation, effectively increasing the hardening slope. However, the higher rate of slope increase during initial cycling for low stress levels seems counter-intuitive. Figure 3.13 showcases the Martensite finish/reversal stresses. It is seen that, during initial cycling, the higher stress levels show a clear and evident drop in σ_{Mf}^{rev} values. With decreasing stress levels, a lower rate of decrease, and overall lower decrease in magnitude during initial cycling is observed. For low stress levels, the decrease in σ_{Ms} combined with a relatively unchanging σ_{Mf}^{rev} leads to a large jump in hardening slopes during initial cycling. In contrast, for high stress levels, the decrease in σ_{Ms} combined with a significant drop in σ_{Mf}^{rev} leads to an overall lower rate of hardening. Due to higher stress levels and corresponding transformation, a larger concentration and magnitude of internal stresses may exist that effectively lower the σ_{Mf}^{rev} value to a greater extent than tests at lower stress levels.

Finally, the trend seen with the recovered strains can be described. $Ni_{50.3}Ti_{29.7}Hf_{20}$ observes a decrease in σ_{Ms}, and small increase in hardening, which leads to a marked jump in $\Delta\epsilon$ during initial cycling. $Ni_{50.4}Ti_{30.6}Hf_{19}$ observes similar trends, however, has slightly larger hardening which negates the decrease in σ_{Ms}. This leads to a very small or zero change in $\Delta\epsilon$ during initial cycling. $Ni_{50.5}Ti_{33.5}Hf_{16}$ observed similar σ_{Ms} trends, which should increase recovered strains, however, the very large increase in hardening during initial cycling leads to a drastic drop in $\Delta\epsilon$. After the hardening saturates, so does $\Delta\epsilon$.

3.4.2 Energy Dissipation and Hysteresis Width

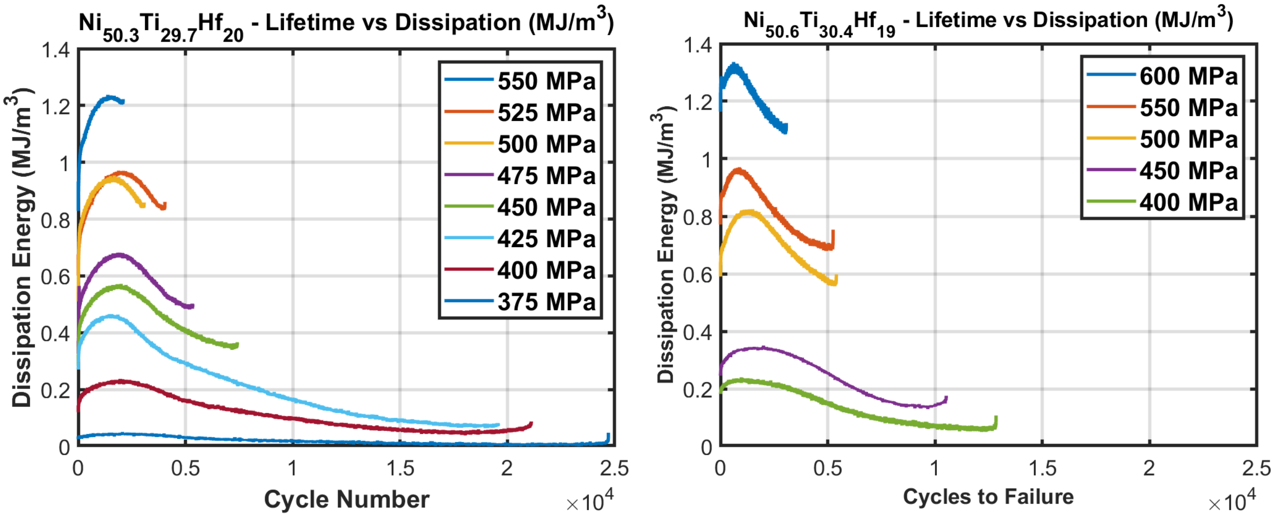

(a) $Ni_{50.3}Ti_{29.7}Hf_{20}$ (b) $Ni_{50.6}Ti_{30.6}Hf_{19}$

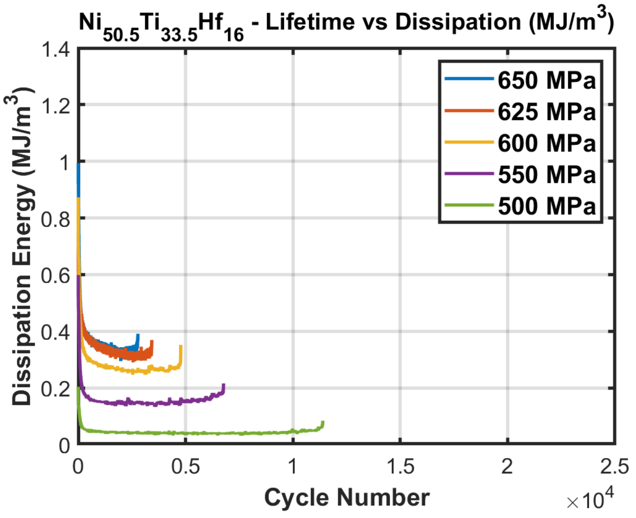

(c) $Ni_{50.5}Ti_{33.5}Hf_{16}$

Figure 3.14: Evolution of Energy Dissipation (E_{diss}) - Hysteresis

Hysteresis/Energy Dissipation - Figure 3.14 showcases the energy dissipation. The hysteresis calculates the total mechanical energy dissipation during each cycle, the results of which are characterized by an initial marked jump, followed by a steady increase to a peak, and continuous decrease till failure where it increases momentarily for the $Ni_{50.3}Ti_{29.7}Hf_{20}$ (see Figure 3.14a) and $Ni_{50.6}Ti_{30.4}Hf_{19}$ (see Figure 3.14b) materials. As seen with other metrics, $Ni_{50.5}Ti_{33.5}Hf_{16}$ showcases no initial increase, but instead a sharp decrease during initial cycling followed by rapid stabilization. The peak hysteresis energy corresponds to between 2000–3000 cycles for the results presented so far, regardless of stress level for materials that show an increase, with $Ni_{50.3}Ti_{29.7}Hf_{20}$ peaking at higher cycles than $Ni_{50.6}Ti_{30.4}Hf_{19}$. Energy dissipation increases with increasing stress levels, due to the corresponding increase in transformation strains. Changes in hysteresis can be tracked back to the trends in the metrics analyzed previously. The initial jump of hysteresis value comes from the rapid accumulation of plastic strains, along with increased transformation or recovered strains behavior during initial cycling. Plastic strain accumulation is an important mechanism for energy dissipation. In the subsequent cycles, the decrease in yield stresses (σ_{Ms}) for martensite transformation and minor hardening lead to an overall increase in martensite volume fraction, leading to larger energy dissipation as seen with an increase to a peak. During further cycling, the saturation of the transformation stresses, rapid reduction of transformation strains, and hardening aid in the reduction of the energy dissipation values. For $Ni_{50.5}Ti_{33.5}Hf_{16}$ however, the large accumulation of plastic strains during the first couple cycles leads to a large dissipation, which is why initial dissipation value fall much higher than stabilized values. Unlike the other materials, which show a rapid followed by a gradual increase to a peak, $Ni_{50.5}Ti_{33.5}Hf_{16}$ observes rapid hardening and strain loss from initial plastic strain accumulation, effectively reducing the hysteresis during initial cycling. The hysteresis values then stabilize quickly, with values much lower than what is observed during the first cycle. The hysteresis energy evolution encapsulates the changes seen with the many pseudoelastic metrics, which describe the changes in the stress-strain response effectively. The total change and rate of change of these metrics depend on the total and rate of change of plastic strain trends, which effectively presents itself within the hysteresis evolution. As such, just by a visual inspection of hysteresis trends; recovered strain, transformation stresses, and hardening slope and most importantly plastic strain trends can also be inferred, providing for a more cohesive method for material functional screening.

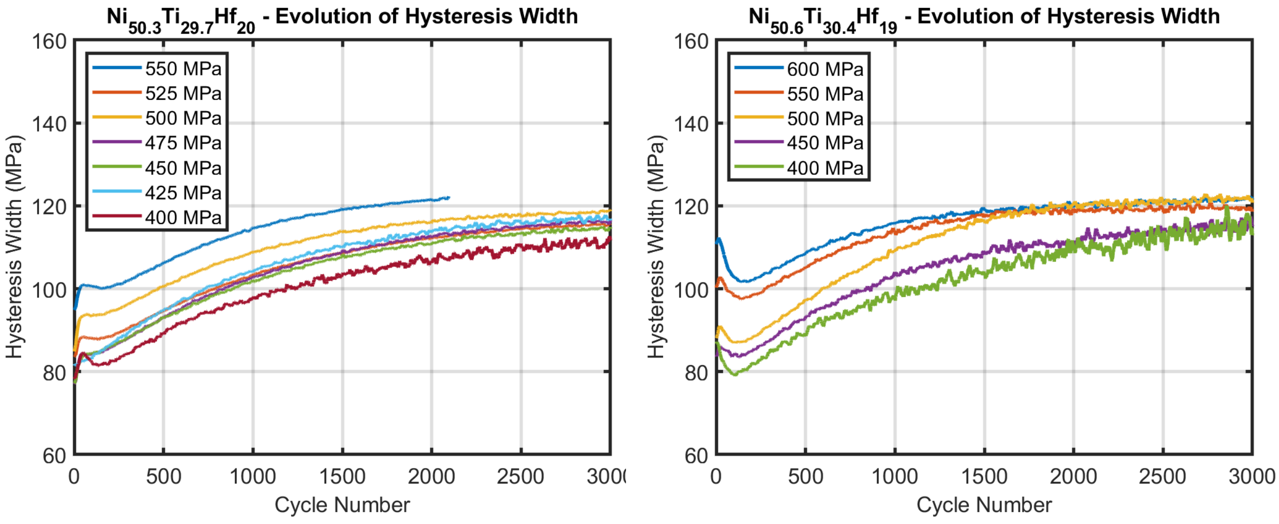

(a) $Ni_{50.3}Ti_{29.7}Hf_{20}$ (b) $Ni_{50.6}Ti_{30.6}Hf_{19}$

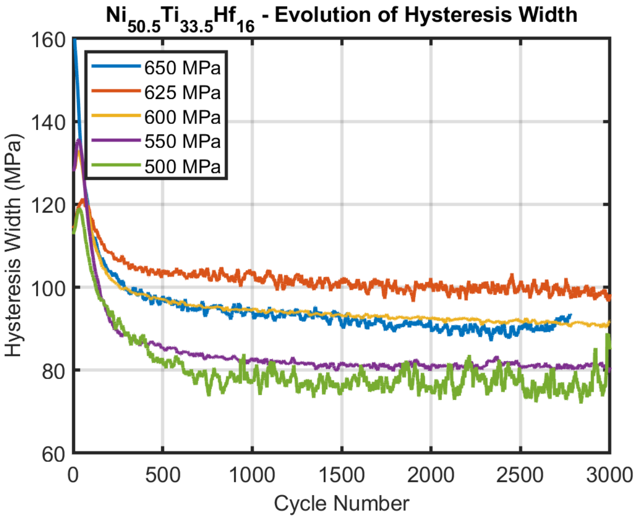

(c) $Ni_{50.5}Ti_{33.5}Hf_{16}$

Figure 3.15: Evolution of Hysteresis Width (H_{width})

Hysteresis Width - Figure 3.15 showcases the hysteresis width (H_{width}) trends. Across all materials, the general trend shows an increase in overall H_{width} for higher stress levels. $Ni_{50.3}Ti_{29.7}Hf_{20}$ (see Figure 3.15a) and $Ni_{50.6}Ti_{30.4}Hf_{19}$ (see Figure 3.15b) showcase peak to valley behavior during initial cycling, before gradual increase observing asymptomatic behavior. All curves, for both materials, stabilize to a similar value near 120 MPa. During the discussion regarding transformation stresses, it was showcased how the Martensite Start and Austenite Finish Stresses fall at a higher rate compared to Martensite finish/reversal and Austenite start/reversal stresses. The hysteresis width can give valuable information on how changes in transformation stresses for each parent phase compare to one another. The increase in H_{width} for $Ni_{50.3}Ti_{29.7}Hf_{20}$ and $Ni_{50.6}Ti_{30.4}Hf_{19}$ before stabilization showcases a higher rate of decrease for Austenite Stresses compared to the Martensite counterparts. For $Ni_{50.5}Ti_{33.5}Hf_{16}$, the decrease implies the opposite effect, which showcases a higher rate of decrease for Martensite Stresses compared to the Austenite counterparts. Here, the curves corresponding to different stress levels saturate at different values of Hysteresis Width, with lower stress values stabilizing at lower H_{width} values.

Cycling during later stages for fatigue tests with $N_f > 10^4$, stress-strain curves shows an almost linear like response (see Figure 3.8). This is confirmed by macroscopic observation showing that the recovered strain ($\Delta\epsilon$) consists of mainly elastic strains (ϵ_e) (see Figure 3.2c). This is due to the reduction of transformation levels to *near* zero from the accumulation of TRIP. However, it must be noted that the response is not truly elastic due to the existence of a small but visible hysteresis, implying small values of localized transformation. This very same phenomenon and explanation can be extended to the strain energy, which shows similar trends to energy dissipation.

Analyzing the changes observed for the aforementioned metrics helps to form the bigger picture on the evolution of the stress-strain response observed throughout a samples lifetime, and consequently the influence of material properties such as ductility, and loading conditions on functional fatigue. Despite the interdependence of many of these metrics on their evolution, it can be inferred from the analysis that the fundamental reason comes down to the formation and accumulation of plastic strains via TRIP from dislocation motion and increase in dislocation density. As discussed earlier, this change in defect density forms the catalyst for the formation of initial microcracks. As such, structural and functional fatigue share similar origins.

Figure 3.16 below summarizes the characteristics of functional fatigue during mechanical cycling of NiTiHf HTSMAs.

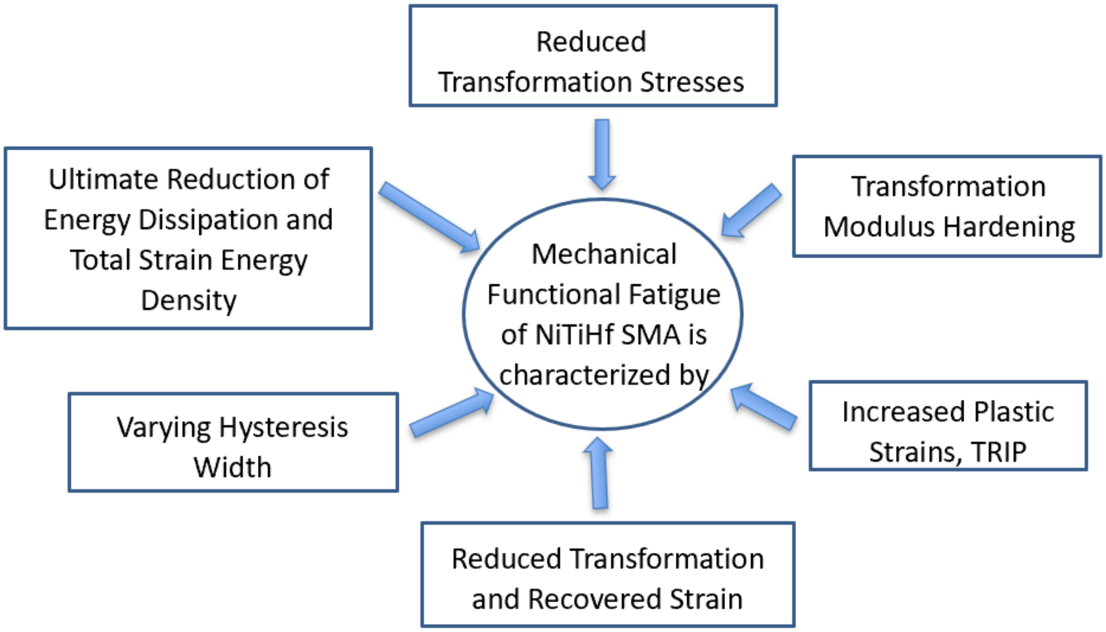

Figure 3.16: Factors Influencing Functional Fatigue during Mechanical Cycling

4. CONCLUSIONS

4.1 Summary

In recent years, the multifunctionality of shape memory alloys has garnered keen interest due to its applicability for use in solid-state actuator systems. As a result, research into studying and improving SMA properties such as cyclic and microstructural reversibility, work output, transformation strain, corrosion resistance and tailoring of transformation temperatures for specific applications has led to the discovery of precipitation strengthened High-temperature SMAs (HTSMAs). Among these, NiTiHf is especially liked due to its cost-effectiveness compared to other ternary SMAs that have metals such as Platinum and Gold as one of their constituent elements. Due to their potential for use in actuators, good fatigue properties are highly desirable. Consequently, recent studies into improving the actuation fatigue resistance of NiTiHf materials has gained momentum.

Actuation fatigue tests, which is when the material is cycled between an Upper and lower cycle temperature at a constant load, can be long and laborious to conduct due to their high heating and cooling rates. As a result, mechanical fatigue experiments, which is when the material is cycled between an upper and lower cycle load at constant temperature, were carried out to create a trend for the mechanical fatigue response of the material in the form of Wohler curves. This was done in an effort to realize a correlation between fast mechanical fatigue tests and actuation fatigue tests to use mechanical fatigue as a predictor for actuation fatigue lifetime and corresponding loading conditions.

Tensile mechanical fatigue testing was carried out on three precipitation hardened NiTiHf materials ($Ni_{50.3}Ti_{29.7}Hf_{20}$,$Ni_{50.6}Ti_{30.4}Hf_{19}$, and $Ni_{50.5}Ti_{33.5}Hf_{16}$). All tests were conducted at 1 hertz for fast testing while minimizing thermomechanical coupling effects on fatigue lifetime and functionality from latent heat accumulation. Temperature was set at $A_f + 25°C$ where A_f is the Austenite Finish Temperature at zero stress. The only parameter to be varied between each sample is the upper cycle stress (UCS) which allowed for various levels of partial transformation. Chosen stress levels and temperature were based on characterization tests for each composition, including thermal cycling for a phase diagram. Fractography micrographs, and effects on temperature from thermomechanical coupling due to cyclic loading, are also discussed.

All materials showed decreased fatigue life with increasing upper cycle stress levels. Mechanical fatigue data was correlated and modelled using different approaches including stress based, strain based and stress-strain based (energy) parameters. Using a defined mechanical work equivalent value similar to the actuation work output model, both of which are based on the Smith-Watson-Topper parameter ($\sigma_{max}\Delta\epsilon$), a similarity in the slopes between mechanical and partial heating actuation fatigue is observed, with the mechanical data being offset negatively along the y-axis. This was observed across all materials. Based on these observations, mechanical data can possibly be used as a screening method for the prediction of actuation data and required loading conditions. In estimating actuation fatigue lifetime and loading conditions, one can conduct a series of mechanical tests to determine the slope, and a minimum of one actuation test to determine the offset and required shift, saving on run time and experiments. The physical nature of the offset is qualitatively described. It arises from a combination of high stress levels to reach yield stress for transformation during mechanical cycling compared to actuation operating stress levels, and set temperature that leads to low strains compared to actuation cycling strain values. Combined with frequency effects, which shows reduced strains for higher loading rates, further increasing the divide between actuation and mechanical data.

Along with structural fatigue, the functional fatigue properties of the materials are investigated. A MATLAB routine for the automatic analysis of mechanical stress-strain cyclic curves is implemented. The routine extracts pseudoelastic metrics that describe each cycle, providing an evolution of said metrics throughout a samples' lifetime. This gives an insight into the functional fatigue properties of the material. Using this method, the evolution of multiple parameters such as recovered strains, transformation stresses, hardening slopes, energy dissipation, strain energy, and hysteresis width were characterized to analyze the progression of functional degradation and the factors that influence it as a function of cycles and stress levels between all three materials. For certain tests for the $Ni_{50.3}Ti_{29.7}Hf_{20}$ material, DIC images were taken to showcase the evolution of mesoscalic strains, which allowed for a visual study into the origins and evolution of localized plastic and transformation strains throughout a samples' life. This is then compared with the corresponding macroscopic recovered, transformation, upper cycle, and plastic strains, which showed direct correlations between macro and mesoscopic measurements.

All materials showed characteristically different trends for plastic strain/TRIP accumulation, which spoke to the ductility of each material. Materials with lower Hafnium content exhibited higher ductility. As a result, mechanical cycling of these alloys can be conducted in actuation cycling's stead as a preliminary screening tool to characterize the material's functional trends from the accumulation of plastic strains. Plastic strain based fatigue approaches were considered for both structural and functional fatigue, showcasing potential to bridge modelling gaps between the two types of fatigue. Phenomenological descriptions of the relationship between plastic strain accumulation and pseudoelastic metrics such as transformation stresses, recovered strains and hardening slopes, are assessed that provide insight into the evolution of the macroscopic stress-strain response. It is characterized by a decrease in recovered strain and transformation stresses, with an increase in hardening slope and plastic strains. A potential cause of such changes boils down to the movement and generations of dislocations that promote the development of localized internal stresses. These internal stresses aide transformation, lowering transformation stresses. It also has a gradient associated with it as transformation proceeds, which leads to a hardening phenomenon and an increase in hardening slopes. Further, they promote the accumulation of Transformation Induced Plasticity (TRIP) leading to increased plastic strains at the expense of transformation and recovered strains, as also seen with the DIC measurements. The changes seen in the stress-strain response throughout life, especially during initial cycling, are highly dependent on ductility. The hysteresis energy evolution encapsulates the changes seen with the many pseudoelastic metrics, which describe the changes in the stress-strain response effectively. The total change and rate of change of these metrics depend on the total and rate of change of plastic strain trends, which effectively presents itself within the hysteresis evolution. As such, just by a visual inspection of hysteresis trends; recovered strain, transformation stresses, hardening slope and most importantly plastic strain trends can also be inferred, providing for a more cohesive method for material functional screening.

4.2 Future Study

1. So far, a qualitative description as to the physical nature of the offset has been given. Deeper insight is required to understand the origins of the offset that is shown in the efforts to correlate the actuation and mechanical fatigue results from a quantitative perspective. A parametric study on the effects of frequency or upper cycle temperature would allow for discerning what factors are at play.

2. The work done here applies to uniaxial tension for dogbone specimens. More work has to be done to confirm findings for multiaxial loading conditions, compression, or specimens with different geometries, such as torque tubes.

3. So far, the current study gives an experimental and phenomenological description of structural and functional fatigue trends. Given the trends seen with the analyzed pseudoelastic properties, generalized macroscopic and mesoscopic modelling efforts can be carried out to effectively predict the evolution of metrics such as transformation stresses, transformation strain, and loading/unloading slope hardening based on plastic strain accumulation combined with DIC measurements. With the recent relevance and advances in data-driven machine learning (ML) approaches, the trends identified as a function of loading conditions such as stress, material property such as ductility (plastic strain accumulation), and cycles provide a method to predict macroscopic functional response. Furthermore, it was shown in the plastic strain based fatigue modelling section that plastic strains can be effectively used as a parameter to connect with work output, and hence fatigue life. As such, a cohesive model to predict both functional response and lifetimes can be implemented.

REFERENCES

[1] Bogue, R. (2009). Shape-memory materials: a review of technology and applications. Assembly Automation, 29(3), 214-219.

[2] Machado, L. G., & Savi, M. A. (2003). Medical applications of shape memory alloys. Brazilian journal of medical and biological research, 36, 683-691.

[3] Patel, S. K., Behera, B., Swain, B., Roshan, R., Sahoo, D., & Behera, A. (2020). A review on NiTi alloys for biomedical applications and their biocompatibility. Materials Today: Proceedings, 33, 5548-5551.

[4] Stoeckel, D. (1990). Shape memory actuators for automotive applications. Materials & Design, 11(6), 302-307.

[5] Ma, J., Karaman, I., & Noebe, R. D. (2010). High temperature shape memory alloys. International Materials Reviews, 55(5), 257-315.

[6] Meng, X. L., Zheng, Y. F., Wang, Z., & Zhao, L. C. (2000). Shape memory properties of the $Ti_{36}Ni_{49}Hf_{15}$ high temperature shape memory alloy. Materials Letters, 45(2), 128-132.

[7] Bigelow, G., Noebe, R., Padula, S., Garg, A., & Olson, D. (2006, January). Development and characterization of improved NiTiPd high-temperature shape-memory alloys by solid-solution strengthening and thermomechanical processing. In International Conference on Shape Memory and Superelastic Technologies (No. ASM Paper 12689).

[8] Atli, K. C., Karaman, I., Noebe, R. D., Garg, A., Chumlyakov, Y. I., & Kireeva, I. V. (2010). Improvement in the shape memory response of Ti50. 5Ni24. 5Pd25 high-temperature shape memory alloy with scandium microalloying. Metallurgical and Materials Transactions A, 41(10), 2485-2497.

[9] Bucsek, A. N., Hudish, G. A., Bigelow, G. S., Noebe, R. D., & Stebner, A. P. (2016). Composition, compatibility, and the functional performances of ternary NiTiX high-temperature shape memory alloys. Shape Memory and Superelasticity, 2(1), 62-79.

[10] Khan, M. I., Kim, H. Y., Namigata, Y., Nam, T. H., & Miyazaki, S. (2013). Combined effects of work hardening and precipitation strengthening on the cyclic stability of TiNiPdCu-based high-temperature shape memory alloys. Acta materialia, 61(13), 4797-4810.

[11] Thoma, P. E., & Boehm, J. J. (1999). Effect of composition on the amount of second phase and transformation temperatures of $NixTi90-xHf10$ shape memory alloys. Materials Science and Engineering: A, 273, 385-389.

[12] Ley, N. A., Smith, J., Wheeler, R. W., & Young, M. L. (2019). Effects of thermo-mechanical processing on precipitate evolution in Ni-rich high temperature shape memory alloys. Materialia, 8, 100496.

[13] Bigelow, G. S., Garg, A., Padula Ii, S. A., Gaydosh, D. J., & Noebe, R. D. (2011). Load-biased shape-memory and superelastic properties of a precipitation strengthened high-temperature Ni50. 3Ti29. 7Hf20 alloy. Scripta Materialia, 64(8), 725-728.

[14] Saghaian, S. M., Karaca, H. E., Tobe, H., Turabi, A. S., Saedi, S., Saghaian, S. E., ... & Noebe, R. D. (2017). High strength NiTiHf shape memory alloys with tailorable properties. Acta Materialia, 134, 211-220.

[15] Sanders, B., Crowe, R., & Garcia, E. (2004). Defense advanced research projects agency–Smart materials and structures demonstration program overview. Journal of Intelligent Material Systems and Structures, 15(4), 227-233.

[16] Kudva, J. N. (2004). Overview of the DARPA smart wing project. Journal of intelligent material systems and structures, 15(4), 261-267.

[17] Hartl, D., Volk, B., Lagoudas, D. C., Calkins, F., & Mabe, J. (2006, January). Thermomechanical characterization and modeling of $Ni_{60}Ti_{40}$ SMA for actuated chevrons. In ASME international mechanical engineering congress and exposition (Vol. 47659, pp. 281-290).

[18] Hartl, D. J., & Lagoudas, D. C. (2007, April). Characterization and 3-D modeling of $Ni_{60}Ti_{40}$ SMA for actuation of a variable geometry jet engine chevron. In Sensors and Smart Structures Technologies for Civil, Mechanical, and Aerospace Systems 2007 (Vol. 6529, pp. 1212-1223). SPIE.

[19] Barbarino, S., Ameduri, S., Lecce, L., & Concilio, A. (2009). Wing shape control through an SMA-based device. Journal of Intelligent Material Systems and Structures, 20(3), 283-296.

[20] Carpenter, B., & Lyons, J. (2001). EO-1 technology validation report: Lightweight flexible solar array experiment. NASA/GSFC. Last updated: August, 8.

[21] Barbarino, S., Flores, E. S., Ajaj, R. M., Dayyani, I., & Friswell, M. I. (2014). A review on shape memory alloys with applications to morphing aircraft. Smart materials and structures, 23(6), 063001

[22] Janke, L., Czaderski, C., Motavalli, M., & Ruth, J. (2005). Applications of shape memory alloys in civil engineering structures—Overview, limits and new ideas. Materials and Structures, 38, 578-592.

[23] Doebler, W., Wilson, S., Loubeau, A., & Sparrow, V. (2020, December). Five-year simulation study of NASA's X-59 low-boom carpets across the contiguous United States of America. In eForum Acusticum 2020 (pp. 1001-1008).

[24] Eggeler, G., Hornbogen, E., Yawny, A., Heckmann, A., & Wagner, M. (2004). Structural and functional fatigue of NiTi shape memory alloys. Materials Science and Engineering: A, 378(1-2), 24-33.

[25] Vantadori, S., Carpinteri, A., Di Cocco, V., Iacoviello, F., & Natali, S. (2018). Fatigue analysis of a near-equiatomic pseudo-elastic NiTi SMA. Theoretical and Applied Fracture Mechanics, 94, 110-119.

[26] Lagoudas, D. C., Miller, D. A., Rong, L., & Kumar, P. K. (2009). Thermomechanical fatigue of shape memory alloys. Smart Materials and Structures, 18(8), 085021.

[27] Melton, K. N., & Mercier, O. (1979). Fatigue of NiTi thermoelastic martensites. Acta Metallurgica, 27(1), 137-144.

[28] Rahim, M., Frenzel, J., Frotscher, M., Pfetzing-Micklich, J., Steegmüller, R., Wohlschlögel, M., ... & Eggeler, G. (2013). Impurity levels and fatigue lives of pseudoelastic NiTi shape memory alloys. Acta Materialia, 61(10), 3667-3686.

[29] Demblon, A., Karakoc, O., Sam, J., Zhao, D., Atli, K. C., Mabe, J. H., & Karaman, I. (2022). Compositional and microstructural sensitivity of the actuation fatigue response in NiTiHf high temperature shape memory alloys. Materials Science and Engineering: A, 838, 142786.

[30] Gall, K., Tyber, J., Wilkesanders, G., Robertson, S. W., Ritchie, R. O., & Maier, H. J. (2008). Effect of microstructure on the fatigue of hot-rolled and cold-drawn NiTi shape memory alloys. Materials Science and Engineering: A, 486(1-2), 389-403.

[31] Hornbogen, E., & Eggeler, G. (2004). Surface aspects in fatigue of shape memory alloys (SMA). Materialwissenschaft und Werkstofftechnik: Entwicklung, Fertigung, Prüfung, Eigenschaften und Anwendungen technischer Werkstoffe, 35(5), 255-259.

[32] Tobushi, H., Hachisuka, T., Yamada, S., & Lin, P. H. (1997). Rotating-bending fatigue of a TiNi shape-memory alloy wire. Mechanics of Materials, 26(1), 35-42.

[33] Lin, C., Wang, Z., Yang, X., & Zhou, H. (2020). Experimental study on temperature effects on NiTi shape memory alloys under fatigue loading. Materials, 13(3), 573.

[34] Zhang, Y., You, Y., Moumni, Z., Anlas, G., Zhu, J., & Zhang, W. (2017). Experimental and theoretical investigation of the frequency effect on low cycle fatigue of shape memory alloys. International Journal of Plasticity, 90, 1-30.

[35] Gu, X., Moumni, Z., Zaki, W.,& Zhang, W. (2016). Shakedown based model for high-cycle fatigue of shape memory alloys. Smart Materials and Structures, 25(11), 115012.

[36] Kang, G., Kan, Q., Qian, L., & Liu, Y. (2009). Ratchetting deformation of super-elastic and shape-memory NiTi alloys. Mechanics of Materials, 41(2), 139-153.

[37] Karakoc, O., Demblon, A., Wheeler, R. W., Lagoudas, D. C., & Karaman, I. (2019). Effects of testing parameters on the fatigue performance NiTiHf high temperature shape memory alloys. In AIAA Scitech 2019 Forum (p. 0416).

[38] Phillips, F. R., Wheeler, R. W., Geltmacher, A. B., & Lagoudas, D. C. (2019). Evolution of internal damage during actuation fatigue in shape memory alloys. International Journal of Fatigue, 124, 315-327.

[39] Hamilton, R. F., Sehitoglu, H., Chumlyakov, Y., & Maier, H. J. (2004). Stress dependence of the hysteresis in single crystal NiTi alloys. Acta Materialia, 52(11), 3383-3402.

[40] Kang, G., & Song, D. (2015). Review on structural fatigue of NiTi shape memory alloys: Pure mechanical and thermo-mechanical ones. Theoretical and Applied Mechanics Letters, 5(6), 245-254.

[41] Carmine, M., Fabrizio, N., Emanuele, S., & Franco, F. (2017). Analysis of fatigue damage in shape memory alloys by nanoindentation. Materials Science and Engineering: A, 684, 335-343.

[42] Lagoudas, D. C., & Miller, D. A. (1999, July). Experiments of thermomechanical fatigue of SMAs. In Smart Structures and Materials 1999: Smart Materials Technologies (Vol. 3675, pp. 275-282). SPIE.

[43] Lagoudas, D. C., Li, C., Miller, D. A., & Rong, L. (2000, November). Thermomechanical transformation fatigue of SMA actuators. In ASME International Mechanical Engineering Congress and Exposition (Vol. 19135, pp. 1-6). American Society of Mechanical Engineers.

[44] Miller, D. A., & Lagoudas, D. C. (2000). Thermomechanical characterization of NiTiCu and NiTi SMA actuators: influence of plastic strains. Smart Materials and Structures, 9(5), 640.

[45] Bertacchini, O. W., Lagoudas, D. C., Calkins, F. T., & Mabe, J. H. (2010, January). Transformation induced cyclic behavior and fatigue properties of nickel rich NiTi shape memory alloy actuators. In International Conference on Martensitic Transformations (ICOMAT) (pp. 199-206). Hoboken, NJ, USA: John Wiley & Sons, Inc..

[46] Bertacchini, O. W., Schick, J., & Lagoudas, D. C. (2009, March). Parametric study and characterization of the isobaric thermomechanical transformation fatigue of nickel-rich NiTi SMA actuators. In Behavior and Mechanics of Multifunctional Materials and Composites 2009 (Vol. 7289, pp. 156-167). SPIE.

[47] Bertacchini, O. W., Lagoudas, D. C., & Patoor, E. (2003, August). Fatigue life characterization of shape memory alloys undergoing thermomechanical cyclic loading. In Smart Structures and Materials 2003: Active Materials: Behavior and Mechanics (Vol. 5053, pp. 612-624). SPIE.

[48] Bertacchini, O. W., Lagoudas, D. C., & Patoor, E. (2009). Thermomechanical transformation fatigue of tinicu sma actuators under a corrosive environment–part i: Experimental results. International Journal of Fatigue, 31(10), 1571-1578.

[49] Wheeler, R. W., Hartl, D. J., Chemisky, Y., & Lagoudas, D. C. (2014, September). Characterization and modeling of thermo-mechanical fatigue in equiatomic NiTi actuators. In Smart Materials, Adaptive Structures and Intelligent Systems (Vol. 46155, p. V002T02A009). American Society of Mechanical Engineers.

[50] Wheeler, R., Ottmers, C., Hewling, B., & Lagoudas, D. (2016, April). Actuator lifetime predictions for $Ni_{60}Ti_{40}$ shape memory alloy plate actuators. In Behavior and mechanics of multifunctional materials and composites 2016 (Vol. 9800, pp. 91-101). SPIE.

[51] Wheeler, R. W., Hartl, D. J., Chemisky, Y., & Lagoudas, D. C. (2015, April). Modeling of thermo-mechanical fatigue and damage in shape memory alloy axial actuators. In Behavior and mechanics of multifunctional materials and composites 2015 (Vol. 9432, pp. 140-149). SPIE.

[52] Denowh, C. M., & Miller, D. A. (2012). Thermomechanical training and characterization of Ni–Ti–Hf and Ni–Ti–Hf–Cu high temperature shape memory alloys. Smart materials and structures, 21(6), 065020.

[53] Benafan, O., Bigelow, G. S., Garg, A., Noebe, R. D., Gaydosh, D. J., & Rogers, R. B. (2021). Processing and scalability of NiTiHf high-temperature shape memory alloys. Shape Memory and Superelasticity, 7(1), 109-165.

[54] Karakoc, O., Atli, K. C., Benafan, O., Noebe, R. D., & Karaman, I. (2022). Actuation fatigue performance of NiTiZr and comparison to NiTiHf high temperature shape memory alloys. Materials Science and Engineering: A, 829, 142154.

[55] Karakoc, O., Hayrettin, C., Canadinc, D., & Karaman, I. (2018). Role of applied stress level on the actuation fatigue behavior of NiTiHf high temperature shape memory alloys. Acta Materialia, 153, 156-168. Figure 1.10 reprinted with permission from Elsevier

[56] Karakoc, O., Hayrettin, C., Bass, M., Wang, S. J., Canadinc, D., Mabe, J. H., ... & Karaman, I. (2017). Effects of upper cycle temperature on the actuation fatigue response of NiTiHf high temperature shape memory alloys. Acta Materialia, 138, 185-197.

[57] Demblon, A., Mabe, J. H., & Karaman, I. (2022, May). Extending the Fatigue Life of NiTiHf High Temperature Shape Memory Alloys through Partial Thermal Cycling. In SMST2022 (pp. 36-38). ASM International.

[58] Kockar, B., Karaman, I., Kim, J. I., & Chumlyakov, Y. (2006). A method to enhance cyclic reversibility of NiTiHf high temperature shape memory alloys. Scripta materialia, 54(12), 2203-2208.

[59] Evirgen, A., Basner, F., Karaman, I., Noebe, R. D., Pons, J., & Santamarta, R. (2012). Effect of aging on the martensitic transformation characteristics of a Ni-rich NiTiHf high temperature shape memory alloy. Functional Materials Letters, 5(04), 1250038.

[60] Karaca, H. E., Saghaian, S. M., Ded, G., Tobe, H., Basaran, B., Maier, H. J., ... & Chumlyakov, Y. I. (2013). Effects of nanoprecipitation on the shape memory and material properties of an Ni-rich NiTiHf high temperature shape memory alloy. Acta Materialia, 61(19), 7422-7431.

[61] Haghgouyan, B., Young, B., Picak, S., Baxevanis, T., Karaman, I., & Lagoudas, D. C. (2021). A unified description of mechanical and actuation fatigue crack growth in shape memory alloys. Acta Materialia, 217, 117155. Figure 1.11 reprinted with permission from Elsevier

[62] Evirgen, A., Pons, J., Karaman, I., Santamarta, R., & Noebe, R. D. (2018). H-Phase precipitation and martensitic transformation in Ni-rich Ni–Ti–Hf and Ni–Ti-Zr high-temperature shape memory alloys. Shape Memory and Superelasticity, 4, 85-92.

[63] Coffin Jr, L. F. (1954). A study of the effects of cyclic thermal stresses on a ductile metal. Transactions of the American Society of Mechanical engineers, 76(6), 931-949.

[64] Manson, S. S. (1953). Behavior of materials under conditions of thermal stress (Vol. 2933). National Advisory Committee for Aeronautics.

[65] Tobushi, H., Nakahara, T., Shimeno, Y., & Hashimoto, T. (2000). Low-cycle fatigue of TiNi shape memory alloy and formulation of fatigue life. J. Eng. Mater. Technol., 122(2), 186-191.

[66] Maletta, C., Sgambitterra, E., Furgiuele, F., Casati, R. I. C. C. A. R. D. O., & Tuissi, A. (2012). Fatigue of pseudoelastic NiTi within the stress-induced transformation regime: a modified Coffin–Manson approach. Smart materials and structures, 21(11), 112001.

[67] Kollerov, M., Lukina, E., Gusev, D., Mason, P., & Wagstaff, P. (2013). Impact of material structure on the fatigue behaviour of NiTi leading to a modified Coffin–Manson equation. Materials Science and Engineering: A, 585, 356-362.

[68] Moumni, Z., Van Herpen, A., & Riberty, P. (2005). Fatigue analysis of shape memory alloys: energy approach. Smart Materials and Structures, 14(5), S287.

[69] Zhang, Y., Zhu, J., Moumni, Z., Van Herpen, A., & Zhang, W. (2016). Energy-based fatigue model for shape memory alloys including thermomechanical coupling. Smart Materials and Structures, 25(3), 035042.

[70] Zhang, Y., You, Y., Moumni, Z., Anlas, G., Zhu, J., & Zhang, W. (2019). Stored-energy-based fatigue criterion for shape memory alloys. Smart Materials and Structures, 28(6), 065027.

[71] Song, D., Kang, G., Kan, Q., Yu, C., & Zhang, C. (2015). Damage-based life prediction model for uniaxial low-cycle stress fatigue of super-elastic NiTi shape memory alloy micro-tubes. Smart Materials and Structures, 24(8), 085007.

[72] Calhoun, C., Wheeler, R., Baxevanis, T., & Lagoudas, D. C. (2015). Actuation fatigue life prediction of shape memory alloys under the constant-stress loading condition. Scripta Materialia, 95, 58-61.

[73] Gao, Y., Casalena, L., Bowers, M. L., Noebe, R. D., Mills, M. J., & Wang, Y. (2017). An origin of functional fatigue of shape memory alloys. Acta Materialia, 126, 389-400.

[74] Abuzaid, W., & Sehitoglu, H. (2017). Functional fatigue of $Ni_{50.3}Ti_{25}Hf_{24}$. 7–Heterogeneities and evolution of local transformation strains. Materials Science and Engineering: A, 696, 482-492.

[75] Dornelas, V. M., Oliveira, S. A., & Savi, M. A. (2020). A macroscopic description of shape memory alloy functional fatigue. International Journal of Mechanical Sciences, 170, 105345.

[76] Sidharth, R., Mohammed, A. S. K., & Sehitoglu, H. (2022). Functional Fatigue of NiTi Shape Memory Alloy: Effect of Loading Frequency and Source of Residual Strains. Shape Memory and Superelasticity, 1-19.

[77] Zhang, Y., Moumni, Z., Zhu, J., & Zhang, W. (2018). Effect of the amplitude of the training stress on the fatigue lifetime of NiTi shape memory alloys. Scripta Materialia, 149, 66-69.

[78] Kuner, M. C., Karakalas, A. A., & Lagoudas, D. C. (2021). ASMADA—A tool for automatic analysis of shape memory alloy thermal cycling data under constant stress. Smart Materials and Structures, 30(12), 125003. Figure A.1c reprinted with permission from IOP Publishing

APPENDIX A

AUTOMATIC ANALYSIS OF PSEUDOELASTIC STRESS-STRAIN DATA

A.1 Introduction and Motivation

Part of the analysis of pseudoelastic cyclic stress-strain response is implementing a methodology for the extraction of the different parameters that define a material's functional performance. The non-linear nature of pseudoelastic curves is evident in all SMA regardless of application, including conventional SMAs and high-temperature SMAs. Different physical properties can be attributed to the two phases of the material. Characterizing pseudoelastic stress-strain response serves many purposes including training and studying material behavior prior to and after stabilization (reaching shakedown state), calibration of constitutive models, and commonly to study fatigue properties throughout lifetime which showcase functional performance and degradation of the alloy through parameters such as transformation strains, work output, energy dissipation and plastic strains. Number of cycles can range from tens of cycles for characterization tests and/or material training. Here, functional fatigue may not be of concern, but one may need to analyze the changes in material properties corresponding with training and stabilization. Pseudoelastic fatigue on the other hand ranges is an order to two orders of magnitude higher than the conventional training or characterization experiments, whereby functional fatigue is a very important characteristic of material behavior. Analysis of these hysteresis curves can be done entirely manually via visual inspection and tangent line fitting to determine critical metrics that describe the response. Intuitively, it is understood that this method of analysis is not feasible when running fatigue tests. Manual analysis can render extreme long processing times, and increased risk of inconsistency and error on the part of the person(s) completing the analysis. Furthermore, the purpose of such a tool is not only to characterize the functional response for one or many individual cycles, but to study its evolution. The evolution of multiple metrics described in this section gives valuable insight into the functional fatigue characteristics of the material. Given that structural and functional fatigue share similar origins, the information from such a tool can also provide insight into structural fatigue of the material.

Authors of "*Automatic Analysis of Shape Memory Alloy Thermal Cycling Data under Constant Stress: Methodology and Open-Source Software*" Kuner et al. [78] from the department of Aerospace Engineering at Texas A&M University developed a routine and software dedicated to the automated analysis of actuation cycling Temperature-Strain data. A limitation of their routine was the inability for the analyses of pseudoelastic stress-strain data, which was listed as an avenue for future work. The following section aims to tackle this problem in a similar fashion. Many aspects of the pseudoelastic routine have been inspired by the aforementioned work, with parts of the methodology carried over, which also provides for a consistent method of analysis between the two types of cycling. Established standards have laid out definitions for the determination of the many critical properties that describe a pseudoelastic curve essential for characterization, and showcase an idealized version of hysteresis curves that might not reflect actual experimental data. Hysteresis shapes change based on testing parameters (stress, temperature, loading rate) and evolve with each curve in a fatigue test. This introduces different roadblocks. Experimental data may have gaps in data or may be noisy. From Figure 3.8, pseudoelastic curves can undergo extreme shape change from more clear and defined hysteresis curves after training to a complete lack of distinguishable features that make a hysteresis curve for high cycle fatigue. This can be attributed to the inevitable functional degradation from changes in microstructure as the specimen is mechanically cycled. As a result, a more robust and general methodology to extract the various metrics is required that take into account the shape changes.

A.2 Definitions of Extracted Metrics

To the best of the authors' knowledge, no current ASTM standard exists that effectively describes the definitions laid out to describe pseudoelastic curves. In Kuner et al. [78], thermal cycling definitions were well-defined and extracted from ASTM E3097-17 in conjunction with ASTM F2005, as seen in Figure A.1c. However, given the similarity between the curves from thermal cycling and pseudoelasticity, the definitions laid out in the aforementioned ASTM standards can be carried over and applied to pseudoelastic behavior as well. The similarity in this case is showcased by the underlying nature of the curves in the Figure A.1 below, wherein thermal cycling has two near-flat pure phase regions and a steep transformation zone, and two steep pure phase zones with a flat transformation zone for pseudoelasticity. Figure A.1a and Figure A.1b shows how each parameter is physically defined on an idealized partial Stress-Strain Pseudoelastic Curve.

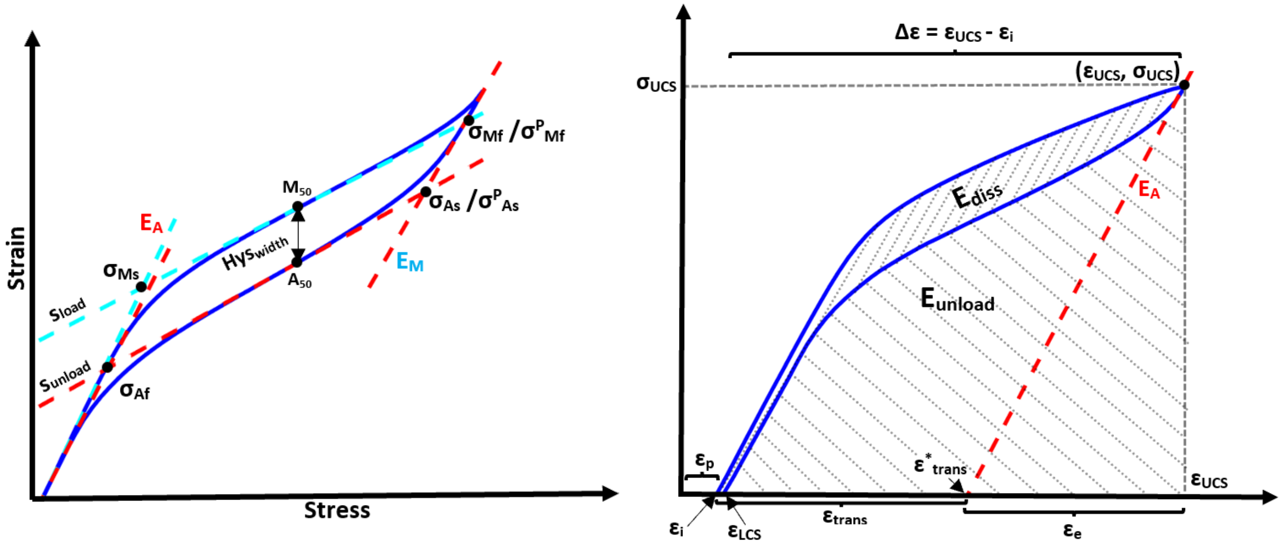

(a) Pseudoelastic Partial Transformation - Tangent Line Method

(b) Pseudoelastic Partial Transformation - Strains and Energy

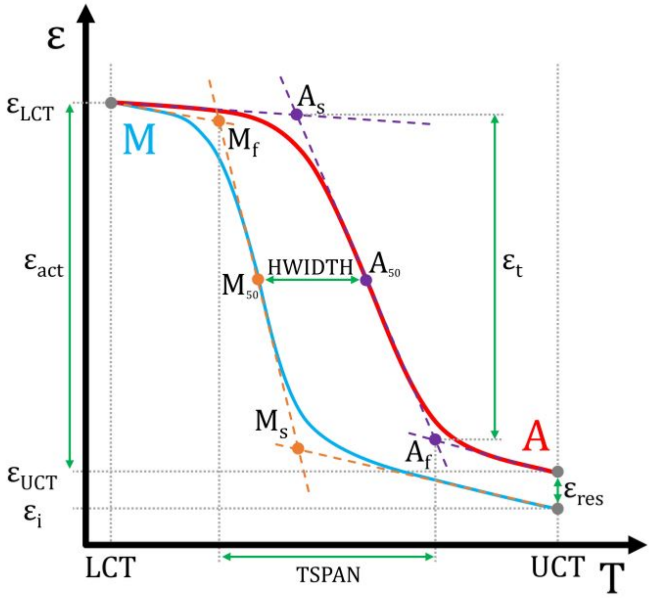

(c) Thermal Cycling Full Transformation (Reprinted with permission from [78])

Figure A.1: Definitions of Metrics

The forward transformation is defined by a transformation from Austenite at the lower cycle stress (LCS), to an intermediate transformation zone, to martensite via a Stress Induced Martensite (SIM) transformation at the Upper Cycle Stress (UCS). Reverse transformation ensues upon unloading, reverting to pure Austenite after another transformation zone. Since loading conditions such as the upper cycle stress, frequency, and the set temperature for isothermal pseudoelastic fatigue dictates the level of induced transformation from Austenite to Martensite, pseudoelastic fatigue tests can consist of full transformation at high UCS's and partial transformation at low UCS's. As a result, a routine designed to analyze mechanical fatigue stress strain data must be able to analyze both full and partial transformations. That being said, it is important to note that for both partial and full transformations, the definitions of the metrics remains constant and consequently both types of transformation can be analyzed using the same methodology from Figure A.1. As such, some metrics such as Martensite finish stress σ_{Mf} and Austenite start stresses σ_{As} are also denoted as σ^p_{Mf} and σ^p_{As} respectively, where the superscript p denotes partial transformation. The routine makes no distinction between full and partial values and reports them as single quantities.

The bulk of the routine deals with the implementation of the tangent line method, which is the method used for the calculation of parameters such as the four transformation stresses/strains, hardening slope and Young's Modulus and is the primary method used for the analyses of actuation data in [78] (see Figure A.1). This routine calculates a total of 26 metrics, which are defined and described in Table A.1 below.

---

[1] Intermediate Value not Exported by Routine

Property	**Symbol**	**Description**
Upper Cycle Stress	σ_{UCS}	Maximum Stress Value of the cycle
Lower Cycle Stress	σ_{LCS}	Minimum Stress Value of the cycle
Martensite Start Stress	σ_{M_s}	Stress threshold indicating initiation of forward transformation. Determined by tangent line method
Martensite Finish/Reversal Stress	σ_{M_f} or $\sigma^p_{M_f}$	Stress threshold indicating completion (full transformation) or reversal point (partial transformation) of forward transformation. Determined by tangent line method
Austenite Start/Reversal Stress	σ_{A_s} or $\sigma^p_{A_s}$	Stress threshold indicating initiation of reverse transformation. Determined by tangent line method
Austenite Finish Stress	σ_{A_f}	Stress threshold indicating completion of reverse transformation. Determined by tangent line method
Martensite Start Strain	ϵ_{M_s}	Strain value corresponding to Martensite Start Stress. Determined by tangent line method
Martensite Finish/Reversal Strain	ϵ_{M_f} or $\epsilon^p_{M_f}$	Strain value corresponding to Martensite Finish/Reversal Stress. Determined by tangent line method
Austenite Start/Reversal Strain	ϵ_{A_s} or $\epsilon^p_{A_s}$	Strain value corresponding to Austenite Start/Reversal Stress. Determined by tangent line method
Austenite Finish Strain	ϵ_{A_f}	Strain value corresponding to Austenite Finish Stress. Determined by tangent line method
Initial Strain	ϵ_i	Strain corresponding to the first data point in the cycle
Lower Cycle Strain	ϵ_{LCS}	Strain corresponding to the Lower Cycle stress during reverse transformation
Upper Cycle Strain	ϵ_{UCS}	Strain corresponding to the Upper Cycle stress
Residual Strain	ϵ_{res}	Irrecoverable strain per cycle. Calculated using $\epsilon_{res} = \epsilon_{UCS} - \epsilon_i$
Recovered Strain	ϵ_{rec} or $\Delta\epsilon$	Total Strain induced during forward transformation. Calculated using $\epsilon_{tot} = \epsilon_{UCS} - \epsilon_{LCS}$
Transformation Strain	ϵ_{trans}	Induced strain from phase transformation. Calculated by the difference of ϵ_i and the intersection of Austenite modulus line at ϵ_{UCS} with x-axis

Table A.1: Description of Pseudoelastic Metrics Calculated by Routine

Austenite Modulus	E_A	Calculated using tangent line method at Austenite pure phase region
Martensite Modulus	E_M	Calculated using tangent line method at Martensite pure phase region
Loading Slope	s_{load}	Calculated using tangent line method at steepest point during forward transformation
Unloading Slope	s_{unload}	Calculated using tangent line method at steepest point during reverse transformation
[1]50% Martensite Transformation	M_{50}	Stress value corresponding to 50% completion of forward transformation. Calculated by $M_{50} = \frac{\sigma_{M_f} - \sigma_{M_s}}{2}$
[1]50% Austenite Transformation	A_{50}	Stress value corresponding to 50% completion of reverse transformation. Calculated by $M_{50} = \frac{\sigma_{A_f} - \sigma_{A_s}}{2}$
Loading Hysteresis	E_{load}	Area under loading curve. Calculated by $\int_{fow} \sigma \, d\epsilon$
Unloading Hysteresis	E_{unload}	Area under unloading curve. Calculated by $\int_{rev} \sigma \, d\epsilon$
Cycle Hysteresis	E_{diss}	Area of enclosed hysteresis. Calculated by $E_{diss} = E_{load} - E_{unload}$
Hysteresis Width	Hys_{width}	Width of cycle hysteresis Calculated by $Hys_{width} = M_{50} - A_{50}$

A.3 Graphical User Interface

Using MATLAB's (version 2022b) app designer, a Graphical User Interface (GUI) was developed in an effort to make the routine available and accessible to users as an open source software. Figure A.2 shows the layout of the Developed GUI. The GUI is composed of three distinct regions.

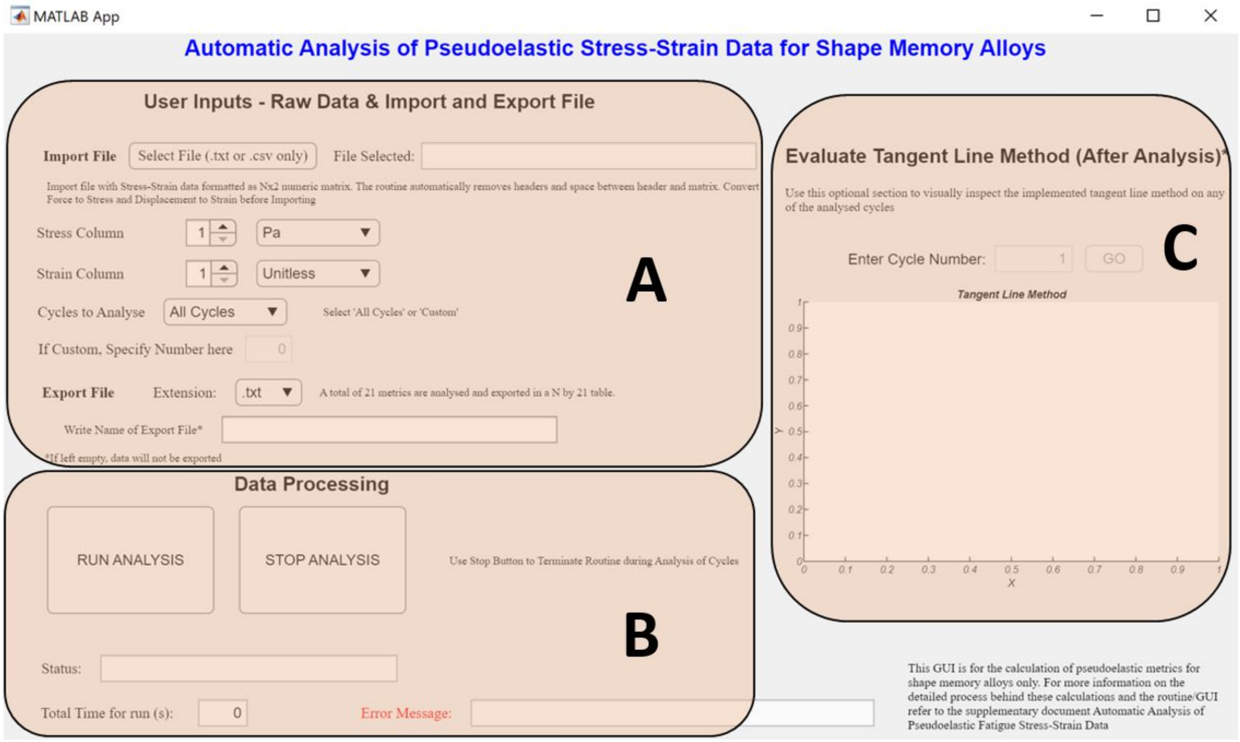

Import file with Stress-Strain data formatted as Nx2 numeric matrix. The routine automatically removes headers and space between header and matrix. Convert Force to Stress and Displacement to Strain before Importing

Stress Column: 1 Pa

Strain Column: 1 Unitless

Cycles to Analyse: All Cycles

Select 'All Cycles' or 'Custom'

If Custom, Specify Number here: 0

Extension: .txt

A total of 21 metrics are analysed and exported in a N by 21 table.

*If left empty, data will not be exported

Use Stop Button to Terminate Routine during Analysis of Cycles

Total Time for run (s): 0

Use this optional section to visually inspect the implemented tangent line method on any of the analysed cycles

Enter Cycle Number: 1

This GUI is for the calculation of pseudoelastic metrics for shape memory alloys only. For more information on the detailed process behind these calculations and the routine/GUI refer to the supplementary document Automatic Analysis of Pseudoelastic Fatigue Stress-Strain Data

Figure A.2: Labelled Graphical User Interface

- Region A shows the user input commands. This is where the user can import a .txt or .csv file with stress-strain data. The user then specifies columns corresponding to stress and strain with units, specifies the number of cycles to analyze and an export file where all calculated metrics will be saved to

- Region B shows the status of the ongoing analysis after the user hits run. The status bar shows where in the analysis the routine is (can be between 'Analyzing Raw Data', 'Analyzing Cycles and Compiling' and finally to 'Exporting and Complete'). It also allows the user to force stop the code while the routine is executing. When the code completes, the time box shows the total time of run. An error box showcases any input errors by the user

- Region C shows another user input dialog box that is accessible after the analysis of data is complete. For the user's ease of mind, the user will be able to visually inspect the proper implementation of the tangent line method for any cycle of their choosing

Furthermore, it must be mentioned that the usefulness of this routine extends to experiments outside just fatigue. Stress-Strain data from experiments, such as characterization and calibration tests or even just one cycle, can be analyzed.

A.4 Methodology

The methodology behind the routine is summarized below in a flowchart in Figure A.3. A more detailed explanation follows in the sections after.

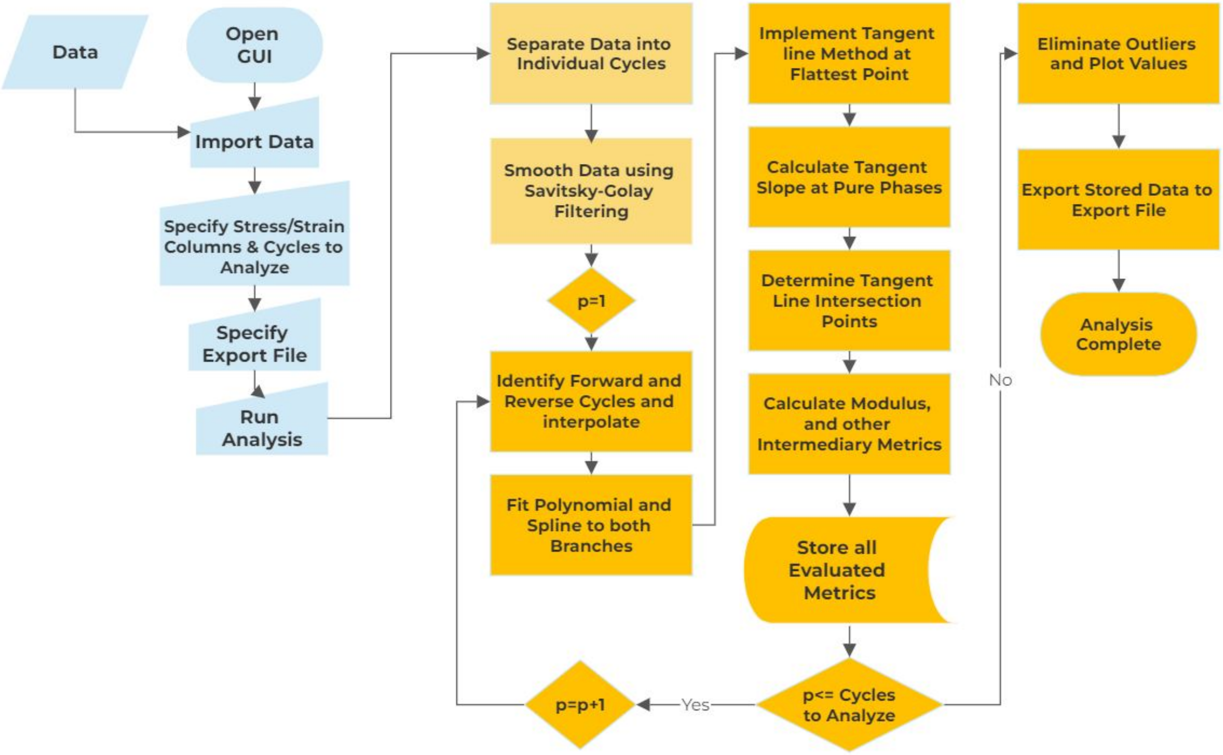

Figure A.3: Flowchart of Implemented Methodology

A.4.1 Raw Data Processing

Upon running the analysis, the routine initiates its process on the data imported. The routine first detects any negative outliers or force values that are below an arbitrary value of -1 MPa and makes them null along with the corresponding strain value. After a material fails, data acquisition systems may continue storing rouge outlier data, as was noticed with some experiments conducted on the MTS frames used predominately throughout this document.

The data is then separated into its constituent cycles, which are further divided into the forward and reverse branches using MATLAB's inbuilt findpeaks function. The data is then smoothed using Savitsky-Golay filtering to eliminate any noise. The smoothing window utilized by the method is proportional to the square root of the number of data points per cycle. This is dependent on the data acquisition rate in conjunction with the loading rate set by the experimenter. This ensures consistent smoothing as a function of number of data points per cycle. In this context, a data point is defined as (ϵ, σ).

A.4.2 The Tangent Line Method

Following from the previous step, each cycle is analyzed individually. To work with a consistent dataset alluding to different data acquisition rates, the data is interpolated to a dataset size of 50 and 2000 data points. These sets serve different purposes.

A.4.2.1 Tangent lines for Hardening Zone - Loading and Unloading Slope

Using a fourth degree order polynomial in the form of

$$\sigma(\epsilon) = a\epsilon^4 + b\epsilon^3 + c\epsilon^2 + d\epsilon + e \tag{A.1}$$

a fit to both the loading and unloading branches to the dataset with 50 points is made. This number of data points is sufficient to describe the curve for a fit and also saves on processing time. Large datasets for fits can considerably increase processing speeds and the overall speed of the analysis. The fit was accomplished using MATLAB's curve-fitting toolbox. The purpose of the polynomial fit is to determine the position of the flattest point in each branch, which corresponds to the location where the first derivative of the fit is at its minimum. This point corresponds to the location where the loading and unloading slopes will be drawn. As discussed earlier, pseudoelastic fatigue consists of full and partial transformations. An example is given in Figure 3.8 in section 3.4 for the tests on $Ni_{50.3}Ti_{29.7}Hf_{20}$ with upper cycle stress levels ranging from 575-375 MPa at a temperature of 175 C and loading rate of 1 Hz.

It is clear from Figure 3.8 that with a decrease in stress level, the more partial the transformation gets. Furthermore, within each fatigue test, the shape of the hysteresis goes through constant changes during the cycling process. The hysteresis slowly evolves and there comes a point where the hysteresis bears no resemblance to a ’regular’ pseudoelastic response, where distinguishing pure phases from transformation zones becomes more tedious. The longer the fatigue life, the greater this effect is seen. Although a regular pseudoelastic full transformation can be modelled by say a logistic function, given the variability in hysteresis shapes, a more versatile fit parameter is required. As a result, a polynomial fit shows promise and is able to fit a much wider range of cycles with exceptional accuracy. The polynomial fit showed greater accuracy as the cycles went on, and as a result was able to predict the flattest region in the curve with great precision even when visually, the hysteresis curves took on very irregular shapes.

Using MATLAB’s *spaps* function, a smooth spline is fit to both the loading and unloading branches. The function is then numerically evaluated to estimate the first derivative or gradient of the stress-strain data. The value of the gradient corresponding to the flattest point calculated by the polynomial fit is extracted and assigned to the corresponding loading or unloading slopes. The approach is visualized in Figure A.4 below.

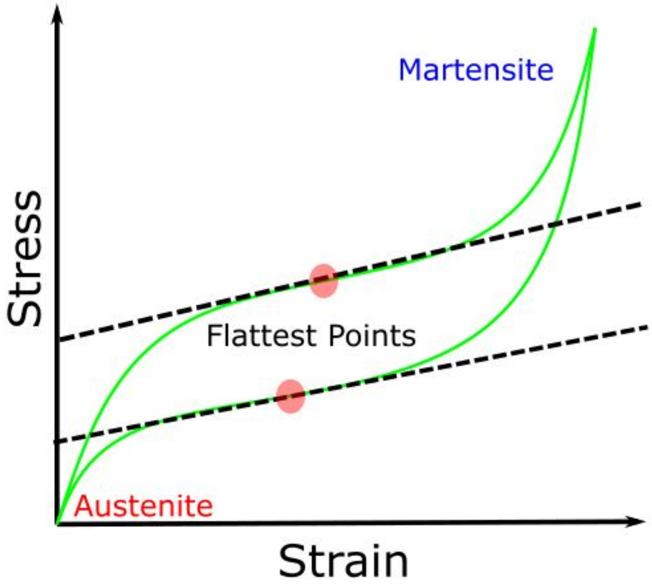

Figure A.4: Tangent Line at Flattest Point on Both Branches

A.4.2.2 Tangent line for Pure Phases

A different technique is utilized to calculate the slopes of the pure phases (steepest regions corresponding to the Austenite and Martensite regions). To calculate the slope (modulus) of the pure regions, a range of data points in the pure phase region is used to calculate a linear fit and determine its slope. To determine the range of data points for say the Austenite slope, the point of intersection of the loading slope and the equation $y = \epsilon_i$ is determined to give a range of the Austenite pure phase. This routine only utilizes 50% of the determined range on the y-axis to form a linear fit. The same method applies for the Martensite slope, where the point of intersection of the unloading slope and the equation $y = \epsilon_{UCS}$ is determined. An example of this process is shown in Figure A.5.

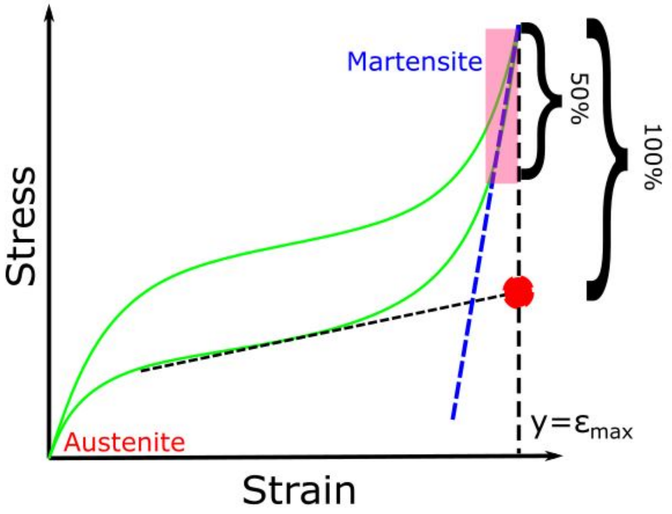

Figure A.5: Calculation of Slopes for Pure Phases

At this point, metrics such as transformation stresses and strains are calculated by the intersection points of the tangent lines. Figure A.6 below showcases the final result of the tangent line method. All the other non-energy metrics are easily calculated using intermediary results from the tangent line method and are referred back to Figure A.1 and table A.1. For plastic strain evolution, the initial strain (ϵ_i) for each cycle is plotted against cycle number.

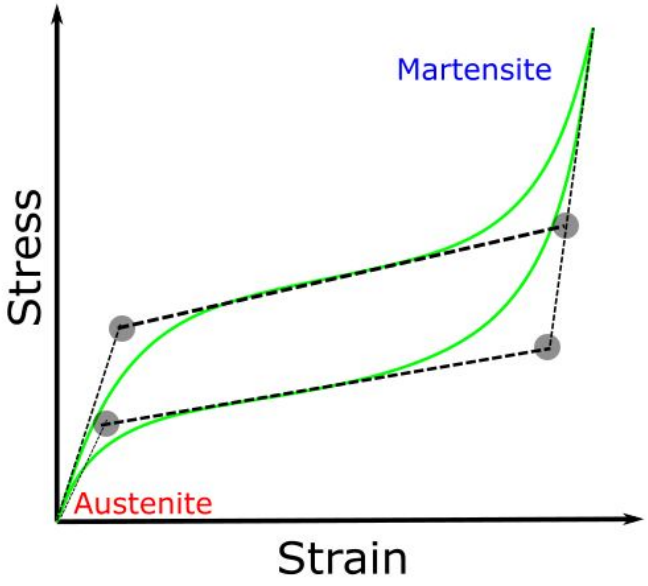

Figure A.6: Intersection Points of Tangent Lines

A.4.3 Hysteresis - Energy Dissipation

The hysteresis area determines the energy dissipation (H_{cycle}/E_{diss}) of the sample during each cycle. The calculation of hysteresis employs the use of the *trapz* function used to numerically integrate the 2000-point interpolated data set using the trapezoidal integration method. Figure A.7 shows the definition for total strain energy $H_{loading}$, recovered strain energy, $H_{unloading}$, and energy dissipation H_{cycle}.

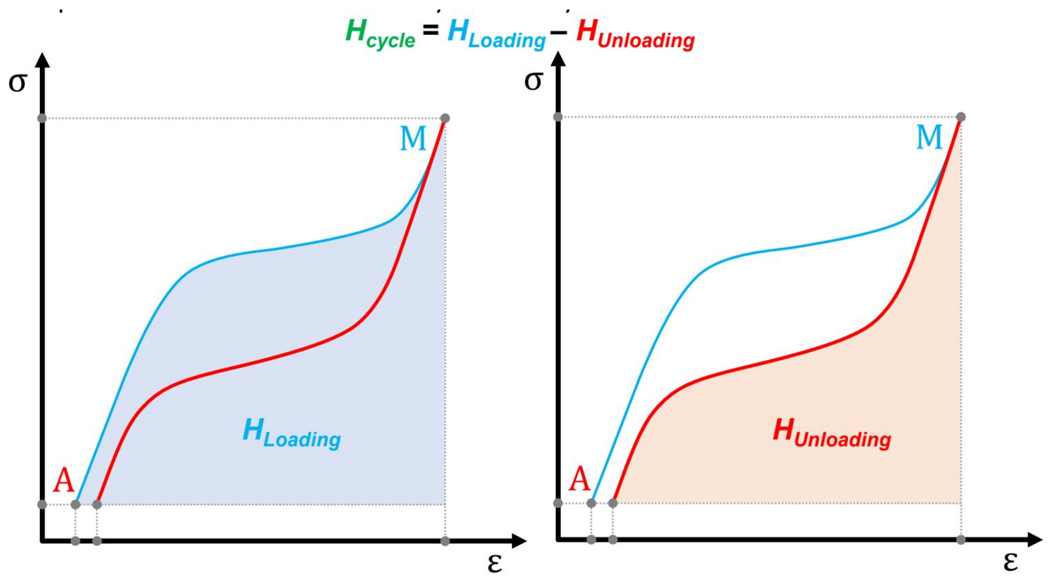

Figure A.7: Calculation of Hysteresis Area

A.5 Discussion of Routine

A.5.1 Advantages

The two primary objectives of such a tool were to provide for a consistent analysis scheme that had the capability to analyze ranges of pseudoelastic response curves of SMAs. Pseudoelastic definitions are inspired from ASTM standards to maintain consistency with thermomechanical fatigue tests. The second objective is to provide for a speedy analysis. The routine, on average, was consistently able to analyze between 25–33 cycles per second with the implementation of the

Tangent line method. It was noticed that consistent use of the routine would slow down processing times due to processing and memory constraints. The formulation of the routine and testing was done on a 2016 personal laptop HP Spectre x360 with Intel Core i7-6500U CPU @ 2.50GHz processor with 16 gigabytes of installed RAM. The size of the data file can also affect processing speeds. It is clear that manual analysis of these curves by visual means would render long hours, along with user inconsistencies that may arise from such a method. As mentioned before, this routine has the ability to analyze pseudoelastic response curves regardless of testing parameters or material. The routine, along with both full and partial transformations, has the ability to analyze extremely deformed and irregular curves that arise from functional fatigue during a samples' lifetime. This allows for a generalized and more robust approach to studying evolution and character zing pseudoelastic behavior.

A.5.2 Limitations

Although this routine has the ability to analyze partial transformation curves, the curves must begin from the Austenite phase, i.e. the constant temperature for these tests must be ideally above Austenite Finish temperature and the lower cycle stress below the critical Austenite finish stress (σ_{Af}) of the material studied. This is to ensure that a "regular" pseudoelastic response is analyzed that show distinct Austenite pure phase regions to implement the tangent line method. In other words, this routine can only analyze closed-loop hysteresis responses (disregarding plastic strain). The routine can only analyze one set of experimental data at a time.

A.5.3 Conclusion

The MATLAB routine developed allows for the automated analysis of pseudoelastic or mechanical stress-strain data. The script comes equipped with a graphical user interface (GUI) that allows for user accessibility and ease of use. A routine as such serves the purpose of drastically reducing analysis times as well as provide a consistent method of analysis inspired by ASTM standards for the characterization of the thermomechanical response of SMAs. This routine

- allows the user to input stress strain data directly into the graphical user interface with ease

- with the data alone, the implemented methodology separates the data into individual cycles, and calculates a total of 26 different metrics as a function of cycle number
- The data is then exportable for further analysis by the user. After the analysis, the user has the ability to validate the implementation of the tangent line method on the cycle(s) of choice by visual inspection